

INHOMOGENEOUS SLAB ANALYSIS & NOVEL THIN-FILM WAVEGUIDE

Ettore Colombini

M. ENG.

Department of Electrical Engineering

ANALYSIS OF AN INHOMOGENEOUS SLAB WAVEGUIDE
AND AN EXPERIMENTAL STUDY OF
A NOVEL MONOMOLECULAR-LAYERED-FILM ANISOTROPIC OPTICAL WAVEGUIDE
FOR INTEGRATED OPTICS

by

Ettore Colombini, B. Eng.

McGill University,

Montreal, Canada.

March, 1977.

ANALYSIS OF AN INHOMOGENEOUS SLAB WAVEGUIDE
AND AN EXPERIMENTAL STUDY OF
A NOVEL MONOMOLECULAR-LAYERED-FILM ANISOTROPIC OPTICAL WAVEGUIDE
FOR INTEGRATED OPTICS

by

Ettore Colombini, B. Eng.

A thesis submitted to the Faculty of Graduate Studies and Research
in partial fulfillment of the requirements for the degree of
Master of Engineering.

Department of Electrical Engineering,

McGill University,

Montreal, Quebec.

March, 1977.

TO MY PARENTS

ABSTRACT

Slab waveguides are of considerable current interest in view of their potential applications in integrated optics in forming a part of the terminal processing optical circuitry.

In the first part of this thesis, a detailed analysis of a symmetric cladded slab waveguide having a parabolic refractive index profile in the core, is carried out. Two techniques, one based on the step-index approximation and the other on the WKB approximation, are used to obtain the dispersion curves and field plots for both the even and odd, TE and TM modes. The two methods are compared, and are found to be complementary.

The second part of this work deals with an experimental study wherein the Blodgett-Langmuir molecular film technique has been used to produce a novel monomolecular-layered-film anisotropic optical waveguide. The film manufacturing process along with the mode coupling, excitation and measurement techniques used to determine the film's permittivity tensor and thickness by correlating the experimental data with theory, are presented in detail.

RÉSUMÉ

Les guides optiques plans suscitent présentement beaucoup d'intérêt en raison de leur utilisation possible dans les circuits intégrés optiques.

La première partie de cette thèse traite de l'analyse détaillée d'une lame diélectrique ayant un profil d'indice de réfraction parabolique, entourée d'un diélectrique tel que le profil du guide est symétrique. Deux méthodes approchées sont employées pour obtenir les courbes de dispersion et la distribution des champs électromagnétiques pour plusieurs modes, TE et TM, symétriques et antisymétriques. La première méthode simule la distribution d'indice parabolique par des gradins homogènes ayant une différence d'indice égale. Ensuite, la méthode BKW est utilisée. Par comparaison, on trouve que les deux méthodes sont complémentaires.

La deuxième partie décrit une étude expérimentale dans laquelle la méthode de Blodgett et Langmuir, qui s'intéresse à la déposition des pellicules unimoléculaires, a été utilisée pour créer un nouveau guide optique composé d'un substrat de quartz recouvert par une couche mince anisotrope. Le procédé de fabrication et la méthode employée pour exciter et mesurer les modes, sont présentées. La comparaison des résultats expérimentaux et de la théorie, permet la détermination du tenseur de la permittivité et l'épaisseur de la couche mince.

ACKNOWLEDGEMENTS

I wish to thank, first of all, my research director Dr. Gar Lam Yip for giving me the opportunity of starting some work in integrated optics here at McGill. His remarkable enthusiasm and the many discussions we had, especially relating to the theoretical first part of this work, show his genuine concern for his graduate students. Indeed, with his help, I had the privilege of presenting the first part of this work at the IEEE/AP-S and USNC/URSI meeting in October 1976.

I also wish to sincerely thank my brother, Dr. Marco Colombini, who suggested the use of the Blodgett-Langmuir molecular film technique to deposit thin organic films on glass substrates. To my knowledge, these monomolecular layered films have never been previously used for the purpose of manufacturing thin-film waveguides. Being specialized in biological membranes, Marco's advice in the details relating to the chemical techniques and the film deposition process, was invaluable and aided in the successful completion of the experimental, second part of this work.

I am grateful to the machine shop crew of the Electrical Eng. Dept. for their skillful manufacture of some of the equipment. The financial support of the National Research Council is also gratefully acknowledged.

The experimental part of this work has been carried out in the new Louis Herdt laboratory.

TABLE OF CONTENTS

<u>CHAPTER</u>	<u>TITLEs</u>	<u>PAGE</u>
ABSTRACT		i
RESUME		ii
ACKNOWLEDGEMENTS		iii
TABLE OF CONTENTS		iv
1	INTRODUCTION	1-1
	1.1 An Inhomogeneous Symmetric Cladded Slab Optical Waveguide	1-2
	1.2 A Monomolecular-Layered-Film Anisotropic Optical Waveguide	1-4
PART I	ANALYSIS OF AN INHOMOGENEOUS SYMMETRIC CLADED SLAB OPTICAL WAVEGUIDE	
2	ANALYSIS BASED ON THE STEP APPROXIMATION	2-1
	2.1 Special Case of a Homogeneous Core Waveguide	2-4
	2.1.1 TE Even Core Modes	2-6
	2.1.2 TE Even Cladding Modes	2-8
	2.1.3 TE Odd Modes and the TM Modes	2-9
	2.2 Extension to the Multi-Layer-Core Waveguide	2-10
	2.2.1 TE Even Modes	2-10
	2.2.2 TE Odd Modes and TM Modes	2-14
	2.3 Numerical Results	2-15
	2.3.1 Computation of the Dispersion Curves	2-15
	2.3.2 Field Computation	2-18
3	ANALYSIS BASED ON THE WKB APPROXIMATION	3-1
	3.1 Analysis for TE Modes	3-1
	3.1.1 Elimination of the Turning Point Singularity	3-5

<u>CHAPTER</u>	<u>TITLE</u>	<u>PAGE</u>
	3.1.2 Dispersion Relation and Fields for the TE Case.	3-8
	3.2 Analysis for TM Modes	3-9
4	DISCUSSION AND CONCLUSIONS	4-1
	4.1 Comparison between the Step and WKB Approximations	4-1
	4.2 Conclusions	4-12
PART II	DEPOSITION OF A MONOMOLECULAR-LAYERED-FILM AND THE DETERMINATION OF ITS BIREFRINGENCE AND THICKNESS THROUGH ITS APPLICATION AS AN ANISOTROPIC OPTICAL WAVEGUIDE	
5	FABRICATION PROCESS	5-1
	5.1 Film Chemistry	5-1
	5.2 Equipment and Procedure for Monolayer Deposition	5-2
	5.2.1 Equipment Considerations	5-2
	5.2.2 Method of Monolayer Deposition	5-5
	5.3 Film Quality	5-11
6	FILM CHARACTERIZATION THROUGH WAVEGUIDE MODE EXCITATION AND MEASUREMENT	6-1
	6.1 Refractive Index and Thickness Measuring Techniques	6-1
	6.2 Light Coupling, Mode Observation and Measurement	6-5
	6.2.1 The Prism-Film Coupler	6-5
	6.2.2 Experimental Technique for Mode Observation and Measurement	6-13
	6.3 Matching of the Experimental and Theoretical Propagation Characteristics to Determine the Film's Birefringence and Thickness	6-24

<u>CHAPTER</u>	<u>TITLE</u>	<u>PAGE</u>
7	CONCLUSIONS AND DISCUSSION ON FURTHER WORK	7-1
<u>APPENDIX</u>		
A	DESCRIPTION OF COMPUTER PROGRAMS UNDER THE 1 ST STEP APPROXIMATION	A-1
	A.1 Computation of the Dispersion Curves	A-1
	A.2 Computation of the E and H Fields	A-4
B	MATERIAL CONCERNING THE WKB METHOD	B-1
	B.1 Nature of the WKB Approximation	B-1
	B.2 The TM Case	B-2
	B.3 Computer Program Flow Charts	B-3
C	DETAILS CONCERNING APPARATUS AND PROCEDURE FOR FILM DEPOSITION	C-1
	C.1 Preparation of Chemicals	C-1
	C.2 Substrate Cleaning Procedure	C-3
	C.3 Procedure for Monolayer Deposition	C-4
D	EQUIPMENT, THEORY, AND DATA FITTING PROGRAM FOR THE DETERMINATION OF THE OPTICAL CONSTANTS OF THE MULTILAYER FILM	D-1
	D.1 Equipment Alignment	D-1
	D.2 Derivation of the Dispersion Relations for a Thin-Film Waveguide whose Film has a Diagonal Permittivity Tensor	D-4
	D.3 Data Fitting Program	D-7
	REFERENCES	R-1

CHAPTER 1INTRODUCTION

The dramatic improvements that have and are presently being made in fiber technology have spurred on much research into all aspects of optical communication systems (1). Their promise of increased bandwidth and freedom from interference justify the need for improved terminal processing hardware which presently takes the form of discrete components (2). The concept of integrated optics (3), whereby various thin-film optical devices along with the electronic circuitry would be assembled on a single substrate, should broaden the present capabilities of microelectronics to the processing of optical signals and also effect the coupling of these to glass fibers for transmission. At the same time it should provide a more reliable, sturdy and economical system.

The considerable amount of effort that has been devoted to this just developing field in the past seven years is readily demonstrated by the great number of papers and meetings on active and passive optical devices (4) - (12). The former consist of : electro-optic and acousto-optic modulators, non-linear thin-film devices such as parametric oscillators and devices employing second harmonic generation (SHG), light deflectors, switches and lasers. The category of passive optical devices includes such items as : couplers, filters, junctions, directional couplers, wavelength multiplexers and microoptics where 2-dimensional optical elements like inhomogeneous slab lenses,

are used to shape and focus the light beam. Although the integration of these various devices is still a few steps away, their present state of development has been indeed a tremendous accomplishment in a very short span of time.

This thesis is composed of two parts: a purely theoretical part where the behaviour of the fields and the propagation characteristics of an inhomogeneous slab waveguide are determined, and an experimental part where a novel anisotropic thin-film waveguide is described and its propagation characteristics compared with theory. Other than that both parts deal with slab waveguides, the two are quite independent and have been treated as such throughout.

1.1 An Inhomogeneous Symmetric Cladded Slab Optical Waveguide

Inhomogeneous thin dielectric slab waveguides are of great interest at the present time due to their potential applications in integrated optics in performing beam-shaping-functions as part of the terminal processing microoptic circuitry. Graded index or self-focusing fiber waveguides which are the 3-dimensional analogue of these, are very advantageous since their transmittable information flows are higher as a result of the decrease of delay distortion (13). At a recent topical meeting on optical fiber transmission, a scheme of using two perpendicularly-crossed slab Selfoc[®] lenses to couple a light beam from a DH semiconductor laser into a Selfoc[®] fiber was proposed (14). These slab Selfoc[®] lenses were fabricated by an ion-exchange technique, and a nearly parabolic distribution (a close approximation to the optimal distribution) of refractive index was obtained.

In order to produce an effective design in these waveguiding circuits, a thorough description of the guided modes and their behaviour with changing geometry and index profile is crucial. However, exact analytical and asymptotic analyses of such waveguiding structures are possible only for a very limited number of specified refractive index profiles (15)-(18) and, in general, numerical techniques are essential.

Marcuse (19) carried out an analysis of the TE modes in graded-index slab waveguides by using a piecewise-linear approximation to the actual index profile as well as the WKB approximation. Kuester and Chang (20) used a numerical procedure, based on the invariant imbedding principle and the transverse impedance concept, to study the various properties of inhomogeneous slab waveguides. The mode property and scattering loss in a slab waveguide with a gradual index distribution has been determined by using a staircase approximation to the profile (21). For exponentially and nonmonotonically varying media, the WKB approximation was found to be convenient in describing the modes (22), (23).

In this work, a detailed analysis of a symmetric cladded slab waveguide having a parabolic refractive index profile in the core is carried out. Although a parabolic distribution is assumed, any symmetric gradual index profile could be analyzed by the methods employed. Two approximate techniques are used to obtain the dispersion curves and the field plots for both the even and odd, TE and TM modes. The first technique involves quantizing the continuously varying index profile into discrete homogeneous steps and then analyzing the resulting multi-layer-core waveguide exactly to obtain approximate results for the

original waveguide. The second technique employs the WKB approximation to a smoothed-out index profile so that the condition of slow index change relative to the wavelength is satisfied.

The two approximate methods are compared and their relative merits are discussed. The elimination of the singularity in the WKB field solution is also discussed.

1.2 A Monomolecular-Layered-Film Anisotropic Optical Waveguide

Work in the field of integrated optics in recent years has mainly been devoted to producing higher quality films, improving ways of coupling light into them, and developing thin-film devices like optical modulators, frequency converters and parametric oscillators. The standard methods of film deposition include vacuum evaporation (24), sputtering (25), and ion implantation (26). The former two in particular, were used (27) to deposit semiconductor films which are essential for electrooptical and non-linear thin-film devices, however these films suffer somewhat from scattering and absorption losses. Although high quality single-crystal films are needed for devices, low-loss amorphous films have been developed (28) and can be used for light guidance between devices. Some of these include acrylic resin films (29), KOR negative photoresist films (30) and gratings for air-film coupling, solution-deposited films (31) for passive and active light guides, and very low loss (<0.04 dB/cm.) organosilicon films (32).

In view of this need for high quality single-crystal films with accurate control of thickness, an investigation has been conducted

into the use of the Blodgett-Langmuir molecular film technique (33)-(35) to coat a surface with single molecular layers 25 Å thick. By superposing these layers of oriented molecules, positive uniaxial birefringent crystals having their optical axis perpendicular (36) to the film surface, are obtained. Barium-copper-stearate is the film material which has been used since it proved successful (34) in "building-up" several thousand layers. Srivastava (37) has compiled an excellent account of the many studies which were carried out to determine the physical properties of these films, two important ones being ellipsometric and interferometric studies for refractive index and thickness evaluation. In addition, he outlined some possible film applications that are being considered. These include : antireflection coatings, interference filters, thickness gauges, X-ray diffraction gratings, ion-selective membranes for electrochemical studies, and electronic devices such as capacitors and tunneling devices between metals. Thin-film waveguides can now be added to this list as a result of the present work.

Indeed, a rudimentary fabrication process has been set up along the same lines used by the original workers. Many problems were encountered in this endeavour and the major ones will be discussed. A detailed procedure which must be carefully followed will be outlined. Although the quality of the present films still requires some improvement, TE and TM modes have been coupled into and out of the film by use of the prism-film coupler (24), and sharply defined angles associated with the modes have been observed and compared with the theory for an

asymmetric slab waveguide with an anisotropic film having a diagonal permittivity tensor. In this way, the thickness, which was already accurately determined (36), and the permittivity tensor, were computed.

The experimental and theoretical results show good agreement in spite of the difficulty in making accurate measurements. This method will be compared with other measuring techniques such as interferometry, X-ray diffraction, and ellipsometry. Unfortunately, the present film is quite lossy due to a large density of scattering centers and possible surface roughness. In addition this film, being basically a soap film, is very soft and is therefore easily damaged. Both these factors make it difficult to guide light over a long distance in the film. Streak lengths up to 3 cm. long have been observed.

This preliminary study however, shows the film's feasibility as an optical waveguide material, and due to its substantial anisotropy, this crystalline film should offer device capabilities. Certain improvements can now be made on the present fabrication system which would both facilitate the film deposition procedure, but more important, improve the film quality. These along with some ideas related to the testing of the electrooptic properties of the film will be presented.

PART I

ANALYSIS OF AN INHOMOGENEOUS SYMMETRIC

CLADDED SLAB OPTICAL WAVEGUIDE

CHAPTER 2

ANALYSIS BASED ON THE STEP APPROXIMATION

The propagation characteristics of a symmetric slab dielectric waveguide, having an inhomogeneous core and a homogeneous, finite cladding, are now examined. The core is assumed to have a parabolic refractive index profile symmetric about $\bar{x} = 0$, the axial plane of the waveguide, as shown in Fig. 2.1 and expressed as :

$$n(\bar{x}) = n_a - (n_a - n_c)\bar{x}^2 \quad (2.1)$$

where : n_a = refractive index on the axial plane

n_c = refractive index in the cladding

n_e = refractive index of the external medium (in Fig. 2.1)

$\bar{x} = \frac{x}{d}$, the normalized transverse distance

d = half the core thickness

This normalization is convenient since the dispersion curves and fields which will be computed, will be independent of the core thickness. The normalized distance to the outer cladding has been denoted r and represents the ratio of the cladding thickness to that of the core.

In the present analysis using the step approximation, the core is subdivided into N homogeneous steps or layers which follow as closely as possible the true refractive index profile with the i th step having an index n_i . The index difference between steps is constant and given by :

$$\delta = (n_a - n_c)/N \quad (2.2)$$

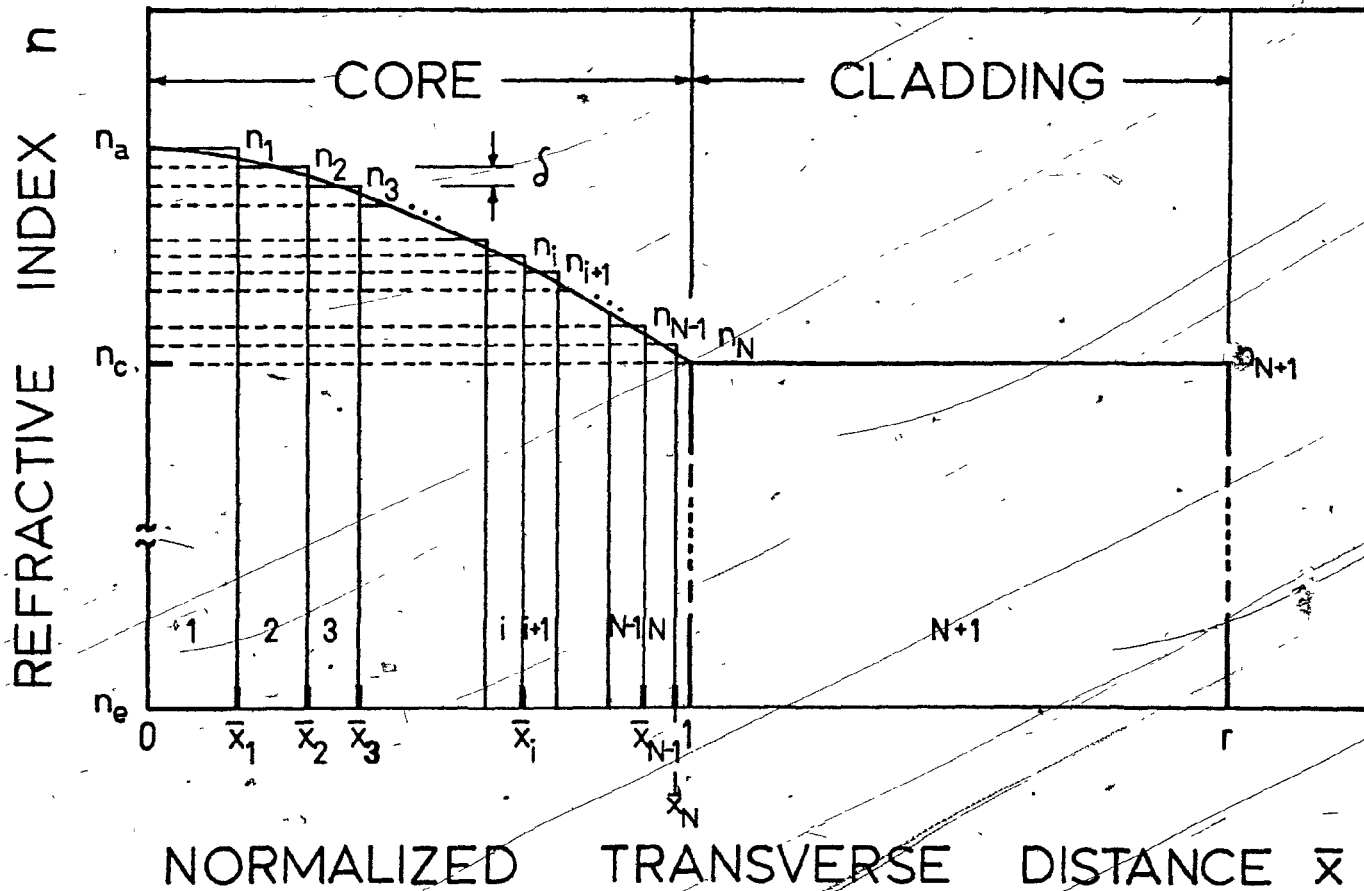


Figure 2.1 Step approximation to the parabolic refractive index profile, symmetric about $\bar{x} = 0$, of a cladded slab waveguide.

From (2.1) the transverse distance is:

$$\bar{x} = \left[\frac{n_a - n(\bar{x})}{n_a - n_c} \right]^{\frac{1}{2}} \quad (2.3)$$

Therefore the normalized transverse distance to the boundary separating region i and $(i+1)$ is:

$$\bar{x}_i = \left[\frac{n_a - (n_i - \frac{\delta}{2})}{n_a - n_c} \right]^{\frac{1}{2}}, \quad i = 1, 2, \dots, N \quad (2.4)$$

where $n_i = n_a - \delta(i - 1)$

In addition, $n_{N+1} = n_c$, $n_{N+2} = n_c$ and $\bar{x}_{N+1} = r$.

It might be correctly anticipated that if a greater number of steps is chosen, the solution obtained would be more accurate since the approximate profile would follow the true one more closely. However, the amount of computation required grows enormously with increasing N . Another type of approximation that could be made is a piecewise-linear one, where instead of using steps, the profile is approximated by straight line segments. The boundary value problem (BVP) which then results, can be solved exactly in terms of Bessel functions instead of the sinusoids and exponentials obtained with homogeneous steps. Although a better approximation would be obtained with the same number of segments as steps, the added computational complexity of using Bessel functions tends to balance out the two approaches.

To facilitate the development of this step approximation technique, the special case of a homogeneous core, finite cladding, slab waveguide is first considered. By solving this BVP, all the possible field solutions in the various regions are obtained, and through a simple

extension, the multi-layer-core waveguide can be easily handled.

2.1 Special Case of a Homogeneous Core Waveguide

Exact field solutions are readily found for the homogeneous core, finite cladding waveguide whose index profile is shown in Fig. 2.2 (a). The homogeneous layers have been labelled 1, 2, and 3, starting from the axial plane. There are two major types of modes which can exist in such a waveguide, guided and radiation modes. In Fig. 2.2(b), a ray picture is given of the guided modes, which consist of core and cladding modes, along with the radiation modes which will not be examined here.

Fig. 2.2(c) shows the various propagation vectors associated with reflection and refraction of light at the interface separating the two homogeneous media labelled 1 and 2. The various parameters, like the refractive index and the propagation vectors, have appropriate subscripts to indicate to which medium they pertain. Each light ray is described by a propagation vector k which is normal to the plane waves as they interact with the interface. The major energy flow occurs in the z -direction and is described by the longitudinal component β in the travelling wave term $\exp j(\omega t - \beta z)$, where time harmonic dependence is assumed. The transverse component K can be real or imaginary. When real, it describes the standing waves occurring in the core, or core and cladding regions as is the case when the light rays are contained by total internal reflection. On the other hand, an imaginary K represents an evanescent or decaying field as is the case in the unbounded external medium.

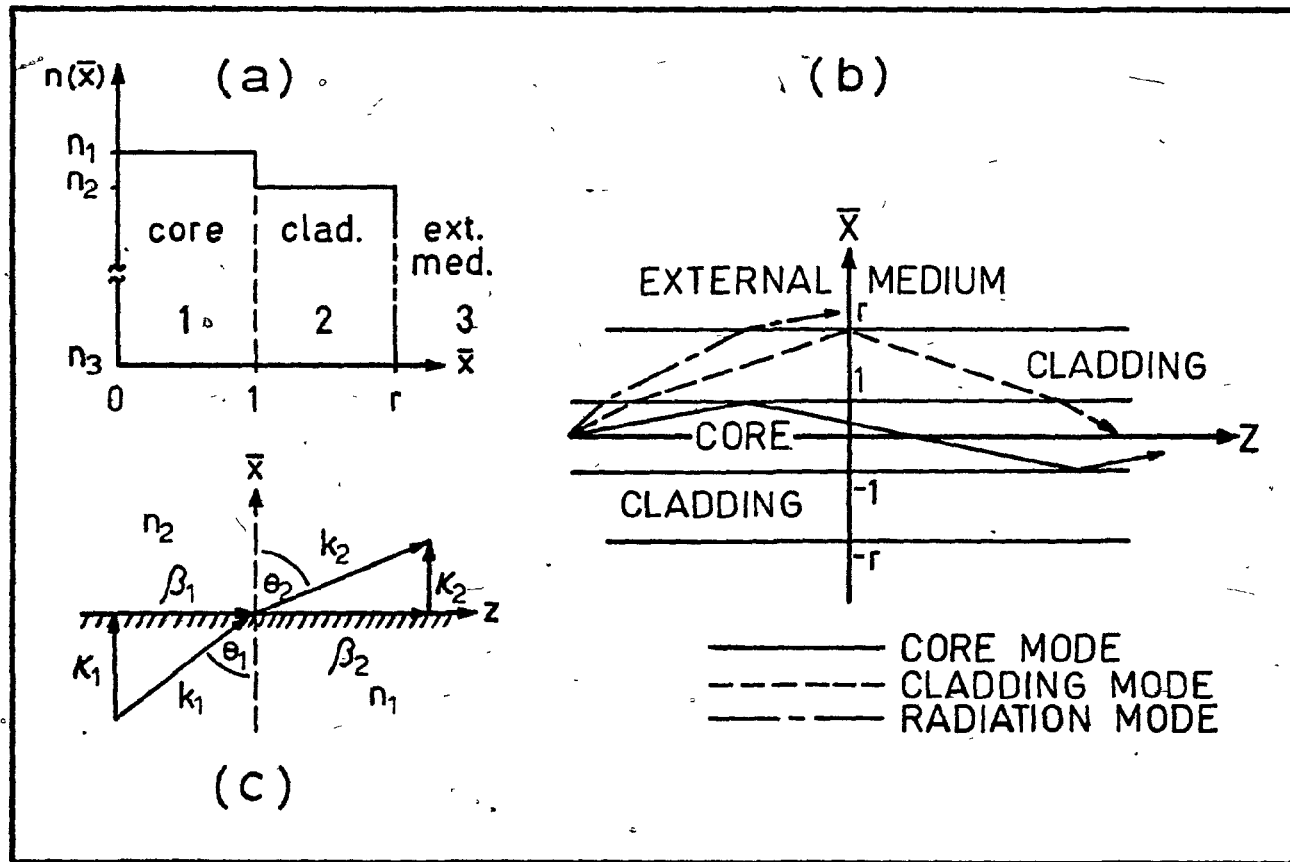


Figure 2.2 (a) Index profile of a homogeneous core waveguide.
 (b) Core, cladding and radiation modes.
 (c) Propagation vectors at an interface.

Assuming no variation in both the geometry and field in the y-direction, then $\frac{\partial}{\partial y} = 0$. This restriction allows decomposition of the field into TE and TM modes. From Maxwell's equations for homogeneous and source free media, it is found that for TE waves the only non-zero field components are H_z , H_x , and E_y given by :

$$\frac{\partial^2 E_y}{\partial x^2} + (k_i^2 - \beta^2) E_y = 0 \quad (2.5a)$$

$$H_z = \frac{j}{\omega\mu_0} \frac{\partial E_y}{\partial x}, \quad H_x = \frac{-j}{\omega\mu_0} \frac{\partial E_y}{\partial z} \quad (2.5b)$$

2.1.1 TE Even Core Modes

Equation (2.5a) is the reduced wave equation, and the solutions for E_y can represent oscillatory or decaying fields depending on whether the transverse propagation vector, $K_i = (k_i^2 - \beta^2)^{\frac{1}{2}}$ is real or imaginary. Since core modes are desired, oscillatory waves will exist only in the core region. Therefore K_1 will be real while K_2 and K_3 will be imaginary. Letting the normalized propagation constant be $\bar{\beta} = \beta/k_0$, the transverse propagation vector in the i th region is then :

$$K_i = k_0(n_i^2 - \bar{\beta}^2)^{\frac{1}{2}}, \quad i = 1, 2, 3$$

It is therefore necessary that $\bar{\beta}$ be in the range $n_2 < \bar{\beta} < n_1$ if only core modes are to exist.

For real K , the solution of (2.5a) is of the form $A \cos(Kx) + B \sin(Kx)$. Since even modes are sought, the second term is neglected at present.

In the core region : $|\bar{x}| \leq 1$

$$E_y = A \cos(K_1 x) = A \cos(K_1 d \bar{x}) \quad (2.6a)$$

$$H_z = -j \frac{K_1}{\omega \mu_0} A \sin(K_1 d \bar{x}) \quad (2.6b)$$

$$K_1 d = k_0 d (n_1^2 - \beta^2)^{\frac{1}{2}} \quad (2.6c)$$

In the cladding : $1 \leq |\bar{x}| \leq r$

$$E_y = C e^{\gamma_2 d |\bar{x}|} + D e^{-\gamma_2 d |\bar{x}|} \quad (2.7a)$$

$$H_z = j \frac{|\bar{x}|}{x} \frac{\gamma_2}{\omega \mu_0} C e^{\gamma_2 d |\bar{x}|} - j \frac{|\bar{x}|}{x} \frac{\gamma_2}{\omega \mu_0} D e^{-\gamma_2 d |\bar{x}|} \quad (2.7b)$$

$$\gamma_2 d = k_0 d (\beta^2 - n_2^2)^{\frac{1}{2}} \quad (2.7c)$$

where $\gamma_i = k_0 (\beta^2 - n_i^2)^{\frac{1}{2}} = jK_i$ is real. Hence, it can be seen that the fields associated with real transverse wavenumbers exhibit oscillatory behaviour, whereas the fields associated with imaginary transverse wavenumbers are evanescent.

In the external medium : $|\bar{x}| \geq r$

$$E_y = \left[C e^{\gamma_2 dr} + D e^{-\gamma_2 dr} \right] e^{-\gamma_3 d (|\bar{x}| - r)} \quad (2.8a)$$

$$H_z = -j \frac{|\bar{x}|}{x} \frac{\gamma_3}{\omega \mu_0} \left[C e^{\gamma_2 dr} + D e^{-\gamma_2 dr} \right] e^{-\gamma_3 d (|\bar{x}| - r)} \quad (2.8b)$$

$$\gamma_3 d = k_0 d (\beta^2 - n_3^2)^{\frac{1}{2}} \quad (2.8c)$$

The boundary conditions require that the E_y and H_z fields be continuous across the interface at $|\bar{x}| = \frac{d}{a}$ and r . This is the same as requiring that the magnitude and slope of E_y be continuous. For a non-

trivial solution, the determinant of the resulting set of homogeneous equations must vanish yielding the following dispersion relation which specifies the allowed values of k_0d for a given $\bar{\beta}$:

$$-K_1d \tan(K_1d) = \gamma_2d \left[\frac{(\gamma_2d - \gamma_3d) - (\gamma_2d + \gamma_3d)e^{2\gamma_2d(r-1)}}{(\gamma_2d - \gamma_3d) + (\gamma_2d + \gamma_3d)e^{2\gamma_2d(r-1)}} \right] \quad (2.9)$$

This is an expression implicit in the single unknown k_0d if equations (2.6c), (2.7c), and (2.8c) are used with a particular value of $\bar{\beta}$. If a root-search technique like the "interval-halving method" (38) is used on (2.9), the dispersion curves ($\bar{\beta}$ vs. k_0d) can be computed. The fields are then easily determined from equations (2.6) - (2.8).

2.1.2 TE Even Cladding Modes

In this case, oscillatory fields occur in the cladding as well as the core region, therefore K_2 must be real and $n_3 < \bar{\beta} < n_2$ is now required. In the core, equations (2.6) are still valid, but in the cladding the growing and decaying exponentials must be replaced by sines and cosines.

In the cladding : $1 \leq |x| \leq r$

$$E_Y = C' \cos(K_2d\bar{x}) + D' \sin(K_2d|\bar{x}|) \quad (2.10a)$$

$$H_Z = -j \frac{K_2}{\omega\mu_0} C' \sin(K_2d\bar{x}) + j \frac{|\bar{x}|}{x} \frac{K_2}{\omega\mu_0} D' \cos(K_2d\bar{x}) \quad (2.10b)$$

$$K_2d = k_0d (n_2^2 - \bar{\beta}^2)^{\frac{1}{2}} \quad (2.10c)$$

In the external medium, equations (2.8) still hold except that the amplitude coefficient is changed to $\{C' \cos(K_2dr) + D' \sin(K_2dr)\}$.

If the tangential fields are now matched at the boundaries, the dispersion relation in the determinant form is :

$$\begin{vmatrix} \cos(K_1 d) & -\cos(K_2 d) & -\sin(K_2 d) \\ -K_1 d \sin(K_1 d) & K_2 d \sin(K_2 d) & -K_2 d \cos(K_2 d) \\ 0 & \gamma_3 d \cos(K_2 d) - K_2 d \sin(K_2 d) & K_2 d \cos(K_2 d) + \gamma_3 d \sin(K_2 d) \end{vmatrix} = 0 \quad \dots (2.11)$$

2.1.3 TE Odd Modes and the TM Modes

The dispersion curves and fields for the odd modes are obtained in the same way as for the even case. The only difference is that the odd part of the solution of the reduced wave equation (2.5a), which had been previously neglected, is now considered. In the core, E_y takes the form $B \sin(K_1 x)$, while in the cladding, for cladding modes :

$$E_y = \frac{|x|}{x} F \cos(K_2 x) + G \sin(K_2 x)$$

TM modes can be handled in a very similar way. In this case, $H_z = 0$ and the only non-trivial field components are E_z , E_x , and H_y , and are given by :

$$\frac{\partial^2 H_y}{\partial x^2} + k_0^2 (n_1^2 - \beta^2) H_y = 0 \quad (2.12a)$$

$$E_z = \frac{-j}{n_1^2 \omega \epsilon_0} \frac{\partial H_y}{\partial x}, \quad E_x = \frac{j}{n_1^2 \omega \epsilon_0} \frac{\partial H_y}{\partial z} \quad (2.12b)$$

From these, the field solutions and the dispersion relation can be obtained as was done previously. However, if the principle of duality

is adopted whereby :

$$\begin{array}{ll} E \rightarrow H & \mu \rightarrow \epsilon \\ H \rightarrow -E & \epsilon \rightarrow \mu \end{array}$$

the fields for the TM case can be obtained directly from those of the TE case.

2.2 Extension to the Multi-Layer-Core Waveguide

The homogeneous step approximation consists of extending the method just discussed, to a waveguide having many homogeneous layers in the core region. The value of the refractive index and size of each layer are chosen by the quantization procedure described previously so that the parabolic index profile is approximated very closely.

2.2.1 TE Even Modes

As might be expected, in addition to the cladding modes, many types of core modes exist depending on how many of the inner core layers support oscillatory fields. In order to distinguish between these modes, the following notation is introduced. Core I modes, where I can take a value from 1 up to N, are said to exist if in layers $1 \leq i \leq I$, K_i is real and there are oscillatory fields, whereas for layers $i > I$, K_i is imaginary and only evanescent fields exist. Since the transverse propagation vectors are :

$$\text{for oscillatory fields : } K_i d = k_0 d (n_i^2 - \beta^2)^{\frac{1}{2}} \quad (2.13a)$$

$$\text{and for decaying fields : } \gamma_i d = k_0 d (\beta^2 - n_i^2)^{\frac{1}{2}} \quad (2.13b)$$

they are related to the single unknown $k_0 d$ for specific values of $\bar{\beta}$.

For core I modes, the oscillatory field solutions to the wave equation (2.5a) in the i th layer ($1 \leq i \leq I$, $\bar{x}_{i-1} \leq |\bar{x}| \leq \bar{x}_i$, and $\bar{x}_0 = 0$) are as follows :

$$E_{y_i} = A_i \cos(K_i d \bar{x}) + B_i \sin(K_i d |\bar{x}|) \quad (2.14a)$$

$$H_{z_i} = -j \frac{K_i}{\omega \mu_0} A_i \sin(K_i d \bar{x}) + j \frac{|\bar{x}|}{x} \frac{K_i}{\omega \mu_0} B_i \cos(K_i d \bar{x}) \quad (2.14b)$$

where $B_1 = 0$ for even modes. By matching E_{y_i} , H_{z_i} and $E_{y_{i+1}}$, $H_{z_{i+1}}$ at x_i ($1 \leq i < I$), the boundaries between layers having oscillatory fields, two equations relating the unknown A_i 's and B_i 's are obtained at each interface.

$$A_i \cos(K_i d \bar{x}_i) + B_i \sin(K_i d |\bar{x}_i|) = A_{i+1} \cos(K_{i+1} d \bar{x}_i) + B_{i+1} \sin(K_{i+1} d |\bar{x}_i|) \quad (2.15a)$$

$$-K_i d A_i \sin(K_i d |\bar{x}_i|) + K_i d B_i \cos(K_i d \bar{x}_i) = -K_{i+1} d A_{i+1} \sin(K_{i+1} d |\bar{x}_i|) + K_{i+1} d B_{i+1} \cos(K_{i+1} d \bar{x}_i) \quad (2.15b)$$

The evanescent field solutions in the layers $I < i \leq N+1$, where the $(N+1)$ th layer represents the cladding, are given by :

$$E_{y_i} = A_i e^{\gamma_i d |\bar{x}|} + B_i e^{-\gamma_i d |\bar{x}|} \quad (2.16a)$$

$$H_{z_i} = j \frac{|\bar{x}|}{x} \frac{\gamma_i}{\omega \mu_0} A_i e^{\gamma_i d |\bar{x}|} - j \frac{|\bar{x}|}{x} \frac{\gamma_i}{\omega \mu_0} B_i e^{-\gamma_i d |\bar{x}|} \quad (2.16b)$$

The fields E_y and H_z are then matched at x_i ($I < i \leq N$), since x_{N+1} is the boundary separating the cladding and the external medium which

will be considered separately.

This gives :

$$A_i e^{\gamma_i d |\bar{x}_i|} + B_i e^{-\gamma_i d |\bar{x}_i|} = A_{i+1} e^{\gamma_{i+1} d |\bar{x}_i|} + B_{i+1} e^{-\gamma_{i+1} d |\bar{x}_i|} \quad \dots (2.17a)$$

$$\begin{aligned} \gamma_i d A_i e^{\gamma_i d |\bar{x}_i|} - \gamma_i d B_i e^{-\gamma_i d |\bar{x}_i|} &= \gamma_{i+1} d A_{i+1} e^{\gamma_{i+1} d |\bar{x}_i|} \\ - \gamma_{i+1} d B_{i+1} e^{-\gamma_{i+1} d |\bar{x}_i|} & \end{aligned} \quad (2.17b)$$

Matching the field at $\bar{x} = \bar{x}_I$ ($i = I$), the boundary separating layers having oscillatory and decaying fields :

$$A_I \cos(K_I d |\bar{x}_I|) + B_I \sin(K_I d |\bar{x}_I|) = A_{I+1} e^{\gamma_{I+1} d |\bar{x}_I|} + B_{I+1} e^{-\gamma_{I+1} d |\bar{x}_I|} \quad \dots (2.18a)$$

$$\begin{aligned} -K_I d A_I \sin(K_I d |\bar{x}_I|) + K_I d B_I \cos(K_I d |\bar{x}_I|) &= \gamma_{I+1} d A_{I+1} e^{\gamma_{I+1} d |\bar{x}_I|} \\ - \gamma_{I+1} d B_{I+1} e^{-\gamma_{I+1} d |\bar{x}_I|} & \end{aligned} \quad (2.18b)$$

The only boundary left is that which separates the cladding and external medium. In this latter medium ($i = N+2$, $|\bar{x}| \geq \bar{x}_{N+1}$), the decaying fields are :

$$E_{Y_{N+2}} = \{E_{Y_{N+1}}(\bar{x}_{N+1})\} e^{-\gamma_{N+2} d (|\bar{x}| - \bar{x}_{N+1})} \quad (2.19a)$$

$$H_{Z_{N+2}} = -j \frac{|\bar{x}|}{x} \frac{\gamma_{N+2}}{\omega \mu_0} \{E_{Y_{N+1}}(\bar{x}_{N+1})\} e^{-\gamma_{N+2} d (|\bar{x}| - \bar{x}_{N+1})} \quad (2.19b)$$

Matching H_z at $\bar{x} = \bar{x}_{N+1}$ since E_y has already been matched in (2.19a) :

$$(\gamma_{N+2}d + \gamma_{N+1}d)A_{N+1} e^{\gamma_{N+1}d|\bar{x}_{N+1}|} + (\gamma_{N+2}d - \gamma_{N+1}d)B_{N+1} e^{-\gamma_{N+1}d|\bar{x}_{N+1}|} = 0 \quad \dots (2.20)$$

However, if cladding modes are considered, the fields in layer N+1 are given by equations (2.14) with $I = N+1$ since core N+1 modes are really cladding modes. In this case, equation (2.20) is replaced by :

$$A_{N+1} \{K_{N+1}d \sin(K_{N+1}d|\bar{x}_{N+1}|) - \gamma_{N+2}d \cos(K_{N+1}d\bar{x}_{N+1})\} + B_{N+1} \{-K_{N+1}d \cos(K_{N+1}d\bar{x}_{N+1}) - \gamma_{N+2}d \sin(K_{N+1}d|\bar{x}_{N+1}|)\} = 0 \quad \dots (2.21)$$

In general, to obtain the dispersion curves for the multi-layer-core waveguide, where $n_c < \bar{\beta} < n_a$ for the core modes while $n_e < \bar{\beta} < n_c$ for the cladding modes, the individual core modes must be considered one at a time. For core I modes, $\bar{\beta}$ is in the range $n_{I+1} < \bar{\beta} < n_I$. With a particular value of $\bar{\beta}$ in this range equations (2.15), (2.17), (2.18), and (2.20), which have been obtained by satisfying the boundary conditions in the various regions, can be combined into a set of $2N+1$ independent, homogeneous equations in $2N+1$ unknowns, the A_i 's and B_i 's. In order to obtain a non-trivial solution, a necessary requirement is that the determinant of the resulting $(2N+1) \times (2N+1)$ coefficient matrix vanish, hence yielding the dispersion relation for the guided modes. This occurs at discrete values of k_0d , the eigenvalues which are being sought for each particular value of $\bar{\beta}$. The arrangement of the set of $2N+1$ equations for core I modes is as follows :

LAYER	BOUNDARY	EQUATIONS	UNKNOWNNS	
1	\bar{x}_1 {	(2.15a)	A_1	0
		(2.15b)	A_2	0
⋮	⋮	⋮	B_2	0
I-1	\bar{x}_{I-1} {	(2.15a)	A_3	
		(2.15b)	B_3	
I	\bar{x}_I {	(2.18a)	⋮	
		(2.18b)	A_I	= ⋮
I+1	\bar{x}_{I+1} {	(2.17a)	B_I	
		(2.17b)	⋮	
⋮	⋮	⋮	A_N	
N	\bar{x}_N {	(2.17a)	B_N	0
		(2.17b)	A_{N+1}	0
N+1	\bar{x}_{N+1} {	(2.20)	B_{N+1}	0

(2.22)

There are two special cases. For core N modes, equations (2.17) do not appear and for cladding modes, also equations (2.18) are absent and (2.20) is replaced by (2.21).

2.2.2 TE Odd Modes and TM Modes

The field equations (2.14a) and (2.16a) which were previously chosen as solutions to the wave equation (2.5a), must be modified slightly for the odd modes. These become :

$$E_{y_i} = \frac{|x|}{x} A_i \cos(K_i d \bar{x}) + B_i \sin(K_i d \bar{x}), \quad 1 \leq i \leq I \quad (2.23)$$

where $A_1 = 0$

$$E_{y_i} = \frac{|x|}{x} A_i e^{\gamma_i d |x|} + \frac{|x|}{x} B_i e^{-\gamma_i d |x|}, \quad I < i \leq N+1 \quad (2.24)$$

The only difference between the dispersion relations for the even and odd modes occurs when the fields at the first boundary are matched. Here equations (2.15) are different for even and odd modes since in the former case $B_1 = 0$ while in the latter $A_1 = 0$. This change must be carried through in (2.22) by changing A_1 to B_1 and altering the first column of the matrix.

As outlined previously, the TM fields can be obtained directly from the TE by using duality. The only difference in the TM coefficient matrix from the TE case is that the factors $K_i d$ and $\gamma_i d$ are changed to $K_i d/n_i^2$ and $\gamma_i d/n_i^2$ respectively, while the arguments of the sinusoids and exponentials remain unchanged.

2.3 Numerical Results

2.3.1 Computation of the Dispersion Curves

The dispersion curves for the TE modes of the multi-layer core waveguide with $N = 4$, $n_a = 1.53$, $n_c = 1.50$, $n_e = 1.00$, and $r = 2.0$, are shown in Fig. 2.3. These were obtained with the aid of a computer program described in Appendix A.1, which, for particular values of $\bar{\beta}$, finds the allowed values of $k_0 d$ for which the determinant of the coefficient matrix in (2.22) vanishes. The particular numerical root-

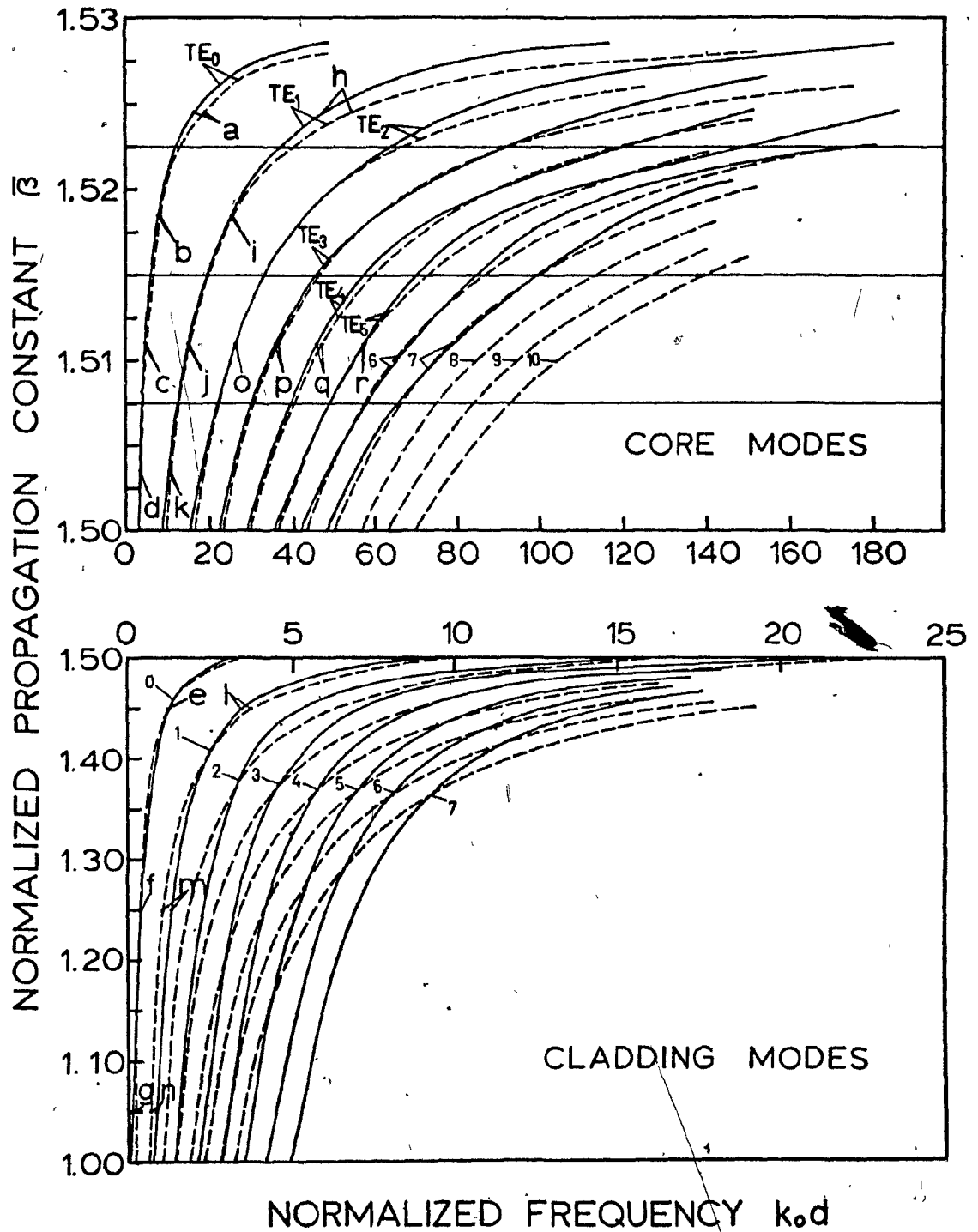


Figure 2.3 Dispersion curves for the TE modes using the step (—) approx. with $N = 4$, $r = 2.0$, and the WKB (----) approx. with $r = 4.2$.

search technique employed is the "interval-halving method" (38), even though it is not too efficient due to its slow convergence, since it is very reliable and the accuracy of the root is readily obtained. In Fig. 2.3, the solid curves represent the results of the step method while the dashed curves represent the results obtained by using the WKB method which will be presented in the next chapter. In this case, a slightly coarse 4 step approximation ($N = 4$) to the core has been used in order to conserve computer time. However, N can be specified arbitrarily as the program is quite flexible and accepts N as a data parameter. One limitation of this technique is in the determination of high order modes with $\bar{\beta}$ close to n_a corresponding to large values of k_0d . For this situation the exponential elements in the matrix become very large and tend to cause overflow problems even after the matrix has been scaled. The TM dispersion curves have also been computed but are so close to the TE curves that the latter serve to represent the TM case reasonably well. A few computed points on the TE and TM curves have been listed in Table 2.1 for comparison.

Table 2.1 : Comparison of a few points on the TE and TM dispersion curves

$\bar{\beta}$	1.5246	1.5185	1.5110	1.5035	1.4500	1.2500	1.0500
k_0d (TE)	16.7	25.1	26.1	10.5	8.9	5.1	1.6
k_0d (TM)	16.9	25.2	26.1	10.6	9.1	5.3	1.7

2.3.2 Field Computation

Once the dispersion curves are obtained, any field associated with a particular point on these curves can be computed by substituting the point coordinates $(\bar{\beta}, k_0d)$ into (2.22) and solving for the unknowns by row reduction. First however, it is necessary to specify one unknown so as to obtain a set of $2N$ inhomogeneous equations. If A_1 is set equal to unity, the fields will be normalized relative to the first layer.

One practical problem arises in the computation of the fields which deserves mention. In the determination of the A_i 's and B_i 's, the difference of very similar numbers is an unavoidable step in the computation. This results in the need for numbers of high accuracy with many significant figures if large errors are to be avoided. Therefore; given the coordinates $(\bar{\beta}, k_0d)$, it is first necessary to recompute the root k_0d to an extremely high accuracy before substitution into the matrix. Even with double precision arithmetic however, for large values of k_0d , the take-over of the growing exponential term in the cladding due to round-off errors is difficult to suppress. As a result, the field plots in Fig. 4.2, to be presented later, have been limited to values of k_0d below 60. A very similar problem was experienced by Marcuse (19) in his analysis of the TE modes in a graded-index slab waveguide using a piecewise-linear approximation to the index profile. A generalized flow chart describing the computer program is presented in Appendix A.2.

CHAPTER 3

ANALYSIS BASED ON THE WKB APPROXIMATION

An important condition for this approximation to hold is a slowly varying refractive index profile as a function of the distance \bar{x} . Fig. 3.1 depicts the smoothed-out profile used in the approximation. It is exact in the core, but deviates from the actual profile in the cladding because the parabolic profile of the core has just been extended. It is therefore expected that the core modes should be in close agreement to those obtained with the step approximation except possibly for values of $\bar{\beta}$ close to n_a corresponding to highly guided modes far from the cutoff. This is so because the analysis assumes widely separated turning points. The turning point \bar{x}_t is defined as the distance \bar{x} where the field changes from oscillatory to evanescent. This occurs when the transverse wavenumber K becomes zero.

3.1 Analysis for TE Modes

The WKB approximation (39) was used in classical physics to solve the Schrodinger equation for the allowable wave functions existing in a potential well. For a continuously varying refractive index profile, the same type of wave equation is obtained and is given by (2.5a) with k_i replaced by $k(x)$.

$$\frac{\partial^2 E_y}{\partial x^2} + K^2(x) E_y = 0 \quad (3.1)$$

where $K^2(x) = \{k^2(x) - \beta^2\}$

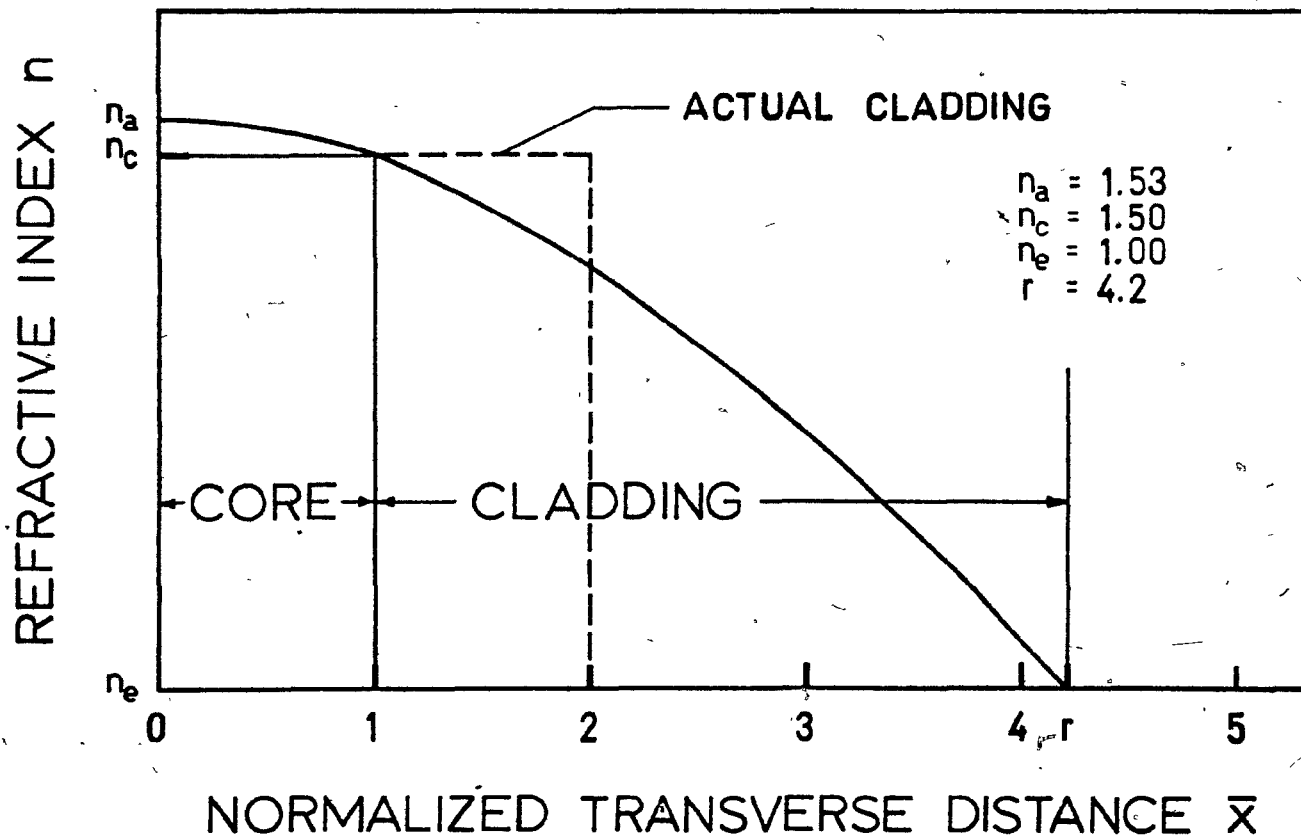


Figure 3.1 Smoothed-out profile for the WKB approximation.

By carrying out a similar type of analysis as in (39) for the case of well-separated turning points, WKB solutions which approximate the oscillatory and decaying fields are obtained.

In the immediate neighborhood of x_t , an exact solution can be found by approximating $K^2(x)$ by $\tilde{K}^2(x)$, a straight line tangent to $K^2(x)$ at x_t .

$$\tilde{K}^2(|x|) = a^2 (x_t - |x|)^2 \quad (3.2)$$

where $-a^2$ is the slope of $K^2(x)$ at x_t .

By letting $w_1 = \int_{|x|}^{x_t} K(x) dx$ be the new independent variable since as x approaches x_t , w_1 approaches:

$$\tilde{w}_1 = \int_{|x|}^{x_t} \tilde{K}(|x|) d|x| = \frac{2}{3} a (x_t - |x|)^{\frac{3}{2}}$$

and then, substituting into (3.1), the guided oscillatory field solution valid near x_t for $|x| \leq x_t$ is:

$$E_y^G = \sqrt{\frac{\tilde{w}_1}{\tilde{K}}} \left[A J_{\frac{1}{3}}(\tilde{w}_1) + B J_{-\frac{1}{3}}(\tilde{w}_1) \right] \quad (3.3)$$

where A and B are constants. In fact, if \tilde{w}_1 and \tilde{K} in equation (3.3) are replaced by w_1 and K , then this equation also describes the oscillatory field solutions far away from the turning point which take the form $K^{-\frac{1}{2}} \exp(\pm jw_1)$ derived in Appendix B.1. This can be verified by using the asymptotic expressions for the Bessel functions as $x \rightarrow \pm\infty$. The constants A and B are constrained by the boundary conditions as $|x| \rightarrow x_t$ and ∞ . Analysis shows that the latter condition, which constrains the

field to approach zero as $|x| \rightarrow \infty$, is satisfied only if $A = B$. An asymptotic solution to (3.1) valid near x_t is then obtained by substituting the asymptotic expressions for the Bessel functions as $|x| \rightarrow x_t$ or $\tilde{w}_1 \rightarrow 0$ into (3.3) yielding :

$$E_{y_t}^G = A \sqrt{\frac{2}{3}} \left[\frac{3 \left(\frac{a}{3}\right)^{\frac{1}{3}} d(\bar{x}_t - |\bar{x}|)}{\Gamma(\frac{1}{3})} + \frac{\left(\frac{a}{3}\right)^{-\frac{1}{3}}}{\Gamma(\frac{2}{3})} \right] \quad (3.4)$$

where Γ is the Gamma function.

Far from the turning point, substitution of the asymptotic expressions for the Bessel functions as $|x| \rightarrow \infty$ or $w_1 \rightarrow \infty$ into (3.3) with \tilde{w}_1 and \tilde{K} replaced by w_1 and K , leads to an approximate solution for the guided oscillatory fields.

Within the turning points $|x| \ll x_t$:

$$E_y^G = C K^{-\frac{1}{2}} \cos(w_1 - \frac{\pi}{4}) \quad (3.5a)$$

where $C = \left(\frac{6}{\pi}\right)^{\frac{1}{2}} A$ and $w_1 = \int_{|x|}^{x_t} K(x) dx$

Outside the turning points for $|x| \gg x_t$, a similar analysis can be performed for the decaying fields yielding a solution like (3.3) except that $J_{\pm\frac{1}{3}}$ is replaced by $I_{\pm\frac{1}{3}}$, w_1 by w_2 , and $K(x)$ by $\gamma(x)$ which can be reduced to :

$$E_y^D = \frac{C}{2} \gamma^{-\frac{1}{2}} e^{-w_2} \quad (3.5b)$$

where $w_2 = \int_{x_t}^{|x|} \gamma(x) dx$ and $\gamma(x) = jK(x)$

Notice that at the turning point a singularity exists in the solutions, K being zero. In an exact solution, no such singularity would exist as

it only appears due to the nature of the approximation.

3.1.1 Elimination of the Turning Point Singularity

As derived in Appendix B.1, the condition of slow index change relative to wavelength for a valid WKB solution is expressed as :

$$\left| \frac{dK}{dx} \right| \ll K^2 \quad \text{or} \quad \left| \frac{dK}{K} \right| \ll 2\pi \frac{dx}{\lambda_x} \quad (3.6)$$

where λ_x is the transverse wavelength. In order to find an estimate for the required deviation D from x_t beyond which equations (3.5) are valid, the expression for $\tilde{K}^2(x)$ given by (3.2) is used to satisfy condition (3.6). As a result :

$$D = | \bar{x} - \bar{x}_t | \gg \text{DEV} = (4d^3 a^2)^{-\frac{1}{3}} \quad (3.7)$$

But since $-a^2$ is just $\left. \frac{dK^2(x)}{dx} \right|_{x=x_t}$ and $n(\bar{x})$ is given by (2.1), then :

$$D \gg \text{DEV} = \{16(k_0 d)^2 \bar{\beta} \bar{x}_t (n_a - n_c)\}^{-\frac{1}{3}} \quad (3.8)$$

From the dispersion curves in Fig. 2.3, it can be seen that as $\bar{\beta}$ decreases, $k_0 d$ also decreases, while \bar{x}_t increases since $\bar{x}_t^2 \propto (n_a - \bar{\beta})$. This results in an overall increase in D . Numerical substitution shows that for $\bar{\beta} = 1.5246$, $\text{DEV} = 0.212$ and $\bar{x}_t = 0.424$, while for $\bar{\beta} = 1.05$, $\text{DEV} = 2.11$ and $\bar{x}_t = 4.0$. Therefore it is found that the singularity affects a considerable portion of the field around \bar{x}_t .

To clarify the situation at the turning point and establish a procedure to plot the fields, Fig. 3.2 is presented to illustrate the E field of the TE_0 mode which has been constructed from the WKB solutions

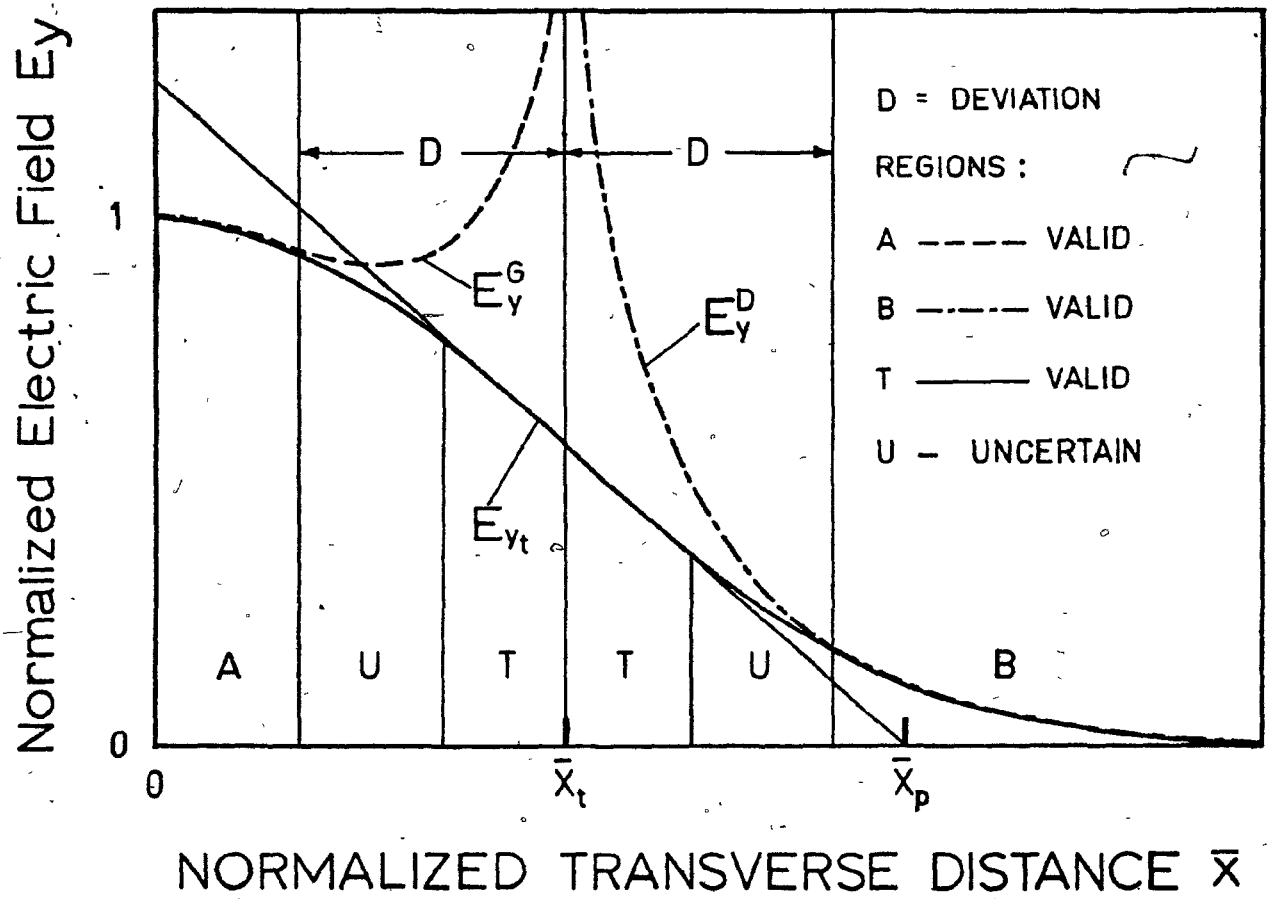


Figure 3.2 E field of the TE_0 mode depicting the regions of validity for the WKB solutions E_y^G and E_y^D , and the turning point asymptote E_{y_t} and the regions of uncertainty.

E_y^G and E_y^D , and is valid for points at a distance much greater than DEV from \bar{x}_t . For \bar{x} near \bar{x}_t , $E_{y_t} = E_{y_t}^G = E_{y_t}^D$ has been used yielding a straight line whose slope is given in terms of A in (3.4). The field is normalized at $\bar{x} = 0$ by setting $C = K^{\frac{1}{2}}(0)$ in equation (3.5). However, A cannot be chosen arbitrarily since E_y^G , E_y^D and E_{y_t} must be asymptotic to the true field in their respective regions of validity. There exists a region of uncertainty separating the regions of validity where neither field is accurately known. Although A is related to C through the factor $(\frac{\pi}{6})^{\frac{1}{2}}$, this relation only becomes valid for higher order modes where the turning point singularity has little effect on the value of the field at $\bar{x} = 0$. For low order modes, A must be chosen so that the field plotted connects E_y^G , E_y^D and E_{y_t} as smoothly as possible in the regions of uncertainty. The unknown A can be eliminated by first setting E_{y_t} , as given in (3.4), equal to zero. Solving for \bar{x} , a unique point \bar{x}_p is found at which E_{y_t} crosses the \bar{x} axis.

$$\left| \bar{x}_p \right| = \bar{x}_t + \frac{\Gamma(\frac{1}{3})}{\Gamma(\frac{2}{3})} (3a^2 d^3)^{-\frac{1}{3}} \quad (3.9)$$

where $a^2 d^3 = 4(k_0 d)^2 \bar{\beta} \bar{x}_t (n_a - n_c)$ from (3.7) and (3.8)

The point \bar{x}_p is called the pivot since E_{y_t} pivots about it as A is varied. Therefore, the slope, and hence A , is chosen graphically to produce the best fit. Further, choosing the slope also corresponds to determining H_z at \bar{x}_t . The normalized value of H_{z_t} is :

$$H_{z_t} N_t = \frac{dE_y/d\bar{x}}{K(0)d} = \frac{\text{SLOPE}}{k_0 d (n_a^2 - \bar{\beta}^2)^{\frac{1}{2}}} \quad (3.10)$$

3.1.2 Dispersion Relation and Fields for the TE Case

Since the refractive index profile is symmetric about $\bar{x} = 0$, the oscillatory fields given by equation (3.5a) must be continuous through the origin. This constraint leads to the dispersion relation :

$$\int_{-x_t}^{x_t} K(x) dx = (m + \frac{1}{2})\pi \quad (3.11)$$

where $m = 0, 2, 4, \dots$ for the even modes

$m = 1, 3, 5, \dots$ for the odd modes

This can be rearranged as :

$$k_0 d = \frac{(m + \frac{1}{2})\frac{\pi}{2}}{\int_0^{x_t} (n^2(\bar{x}) - \bar{\beta}^2)^{\frac{1}{2}} d\bar{x}} \quad (3.12)$$

In this expression, $k_0 d$ is related explicitly to $\bar{\beta}$ so that for a particular value of $\bar{\beta}$, the allowed values of $k_0 d$ for the TE_m modes are given immediately after carrying out a single numerical integration. The TE dispersion curves are therefore readily obtained with the WKB method and are shown by the dashed curves in Fig. 2.3. The normalized electric field components are given by equations (3.5) with $C = K^{\frac{1}{2}}(0) = k_0^{\frac{1}{2}}(n_a^2 - \bar{\beta}^2)^{\frac{1}{4}}$.

Differentiation leads to the normalized magnetic field components :

$$H_{zN}^G(\bar{x}) = \left[\frac{n^2(\bar{x}) - \bar{\beta}^2}{n_a^2 - \bar{\beta}^2} \right]^{\frac{1}{4}} \left[\frac{\bar{x} n(\bar{x}) (n_a - n_c)}{k_0 d \{n^2(\bar{x}) - \bar{\beta}^2\}^{\frac{3}{2}}} \cos(w_1 - \frac{\pi}{4}) + \sin(w_1 - \frac{\pi}{4}) \right] \dots \quad (3.13a)$$

$$H_{zN}^D(\bar{x}) = -\frac{1}{2} \left[\frac{\bar{\beta}^2 - n^2(\bar{x})}{n_a^2 - \bar{\beta}^2} \right]^{\frac{1}{4}} \left[\frac{\bar{x} n(\bar{x}) (n_a - n_c)}{k_0 d \{\bar{\beta}^2 - n^2(\bar{x})\}^{\frac{3}{2}}} + 1 \right] e^{-w_2} \quad (3.13b)$$

These fields are plotted in Fig. 4.2 as the dashed curves using the procedure just discussed to eliminate the singularity at the turning point.

3.2 Analysis for TM Modes

For an inhomogeneous index profile $n(x) = (\epsilon(x)/\epsilon_0)^{1/2}$, the reduced wave equation for the TM case can be derived from Maxwell's equations as given below :

$$\frac{\partial^2 H_y}{\partial x^2} - \frac{1}{\epsilon(x)} \frac{d\epsilon(x)}{dx} \frac{\partial H_y}{\partial x} + \{k^2(x) - \beta^2\} H_y = 0 \quad (3.14)$$

The $\frac{\partial}{\partial x}$ term in (3.14) can be eliminated as shown in Appendix B.2, and the equation reduces to the form :

$$\frac{\partial^2 G}{\partial x^2} + R^2(x) G = 0 \quad (3.15)$$

where

$$G = \bar{\epsilon}^{-1/2}(x) H_y$$

$$R^2(x) = k^2(x) - \beta^2$$

$$S^2(x) = k_0^2 n_{\text{eff}}^2(x)$$

and

$$n_{\text{eff}}^2(\bar{x}) = n^2(\bar{x}) - \frac{2(n_a - n_c) \{3(n_a - n_c)\bar{x}^2 + n_a\}}{n^2(\bar{x}) (k_0 d)^2}$$

The term $n_{\text{eff}}(x)$ can be regarded as an effective refractive index profile required to yield the same type of reduced wave equation as for the TE case. It can then be readily seen that the dispersion relation is similar to equation (3.12) with $n^2(\bar{x})$ replaced by $n_{\text{eff}}^2(\bar{x})$:

$$k_{0d} = \frac{(m + \frac{1}{2}) \frac{\pi}{2}}{\int_0^{\bar{x}_t} \{n_{\text{eff}}^2(\bar{x}) - \beta^2\}^{\frac{1}{2}} d\bar{x}} \quad (3.16)$$

where $m = 0, 2, 4, \dots$ for the even modes

$m = 1, 3, 5, \dots$ for the odd modes

Since $n_{\text{eff}}^2(\bar{x})$ contains k_{0d} , unlike the TE case, in equation (3.16) k_{0d} is given implicitly and therefore its evaluation necessitates the use of a numerical root-search technique. Fortunately, the roots for the TM modes have been found to lie very close to those for the TE modes, and hence, the roots for the latter can be used as the first guesses in searching for the roots of the former. Even so, the computing time is quite considerable since each step in the search for a root requires a numerical integration. This fact makes the WKB method less attractive in the computation of the dispersion curves for the TM modes since the advantage of low computing time at the expense of some loss in accuracy, which is the case for the TE modes, is not present for the TM modes. The TM dispersion curves are so close to the TE shown in Fig. 2.3 that they have not been presented separately. The computer programs used to generate the dispersion curves and field plots are described in Appendix B.3.

CHAPTER 4DISCUSSION AND CONCLUSIONS4.1 Comparison between the Step and WKB Approximations

For ease of comparison, the dispersion curves for the TE modes and the refractive index profiles for both the step and WKB approximations, which were shown in Figs. 2.3 and 3.1 respectively, have been combined in Fig. 4.1. For the core modes, the three horizontal lines shown in the figure represent the boundaries separating the four homogeneous steps used to approximate the core. Results of the WKB approximation presented in dashed curves, agree quite well with the results of the step approximation except for $\bar{\beta} \rightarrow 1.53$ where $k_0 d$ becomes large and near cutoff as $\bar{\beta} \rightarrow 1.50$. Values of $\bar{\beta}$ close to 1.53 correspond to highly guided modes and close turning points, which tends to degrade the WKB solutions. However, the WKB profile corresponds exactly to the actual profile in the core region, and hence, high order modes, which are mainly confined in the core region, are best treated with the WKB method. This method is especially useful since it is very fast computationally. Indeed, the computation of the dispersion curves for these high order modes with the step method becomes increasingly more difficult due to the blow up of the matrix elements with increasing $k_0 d$. As cutoff is approached with $\bar{\beta} \rightarrow 1.50$, the curves again begin to deviate. This is due to the sharp difference between the cladding profiles used in the two methods. In the step method, the actual homogeneous cladding was used, whereas the WKB method allows no abrupt index variations, and consequently, the cladding

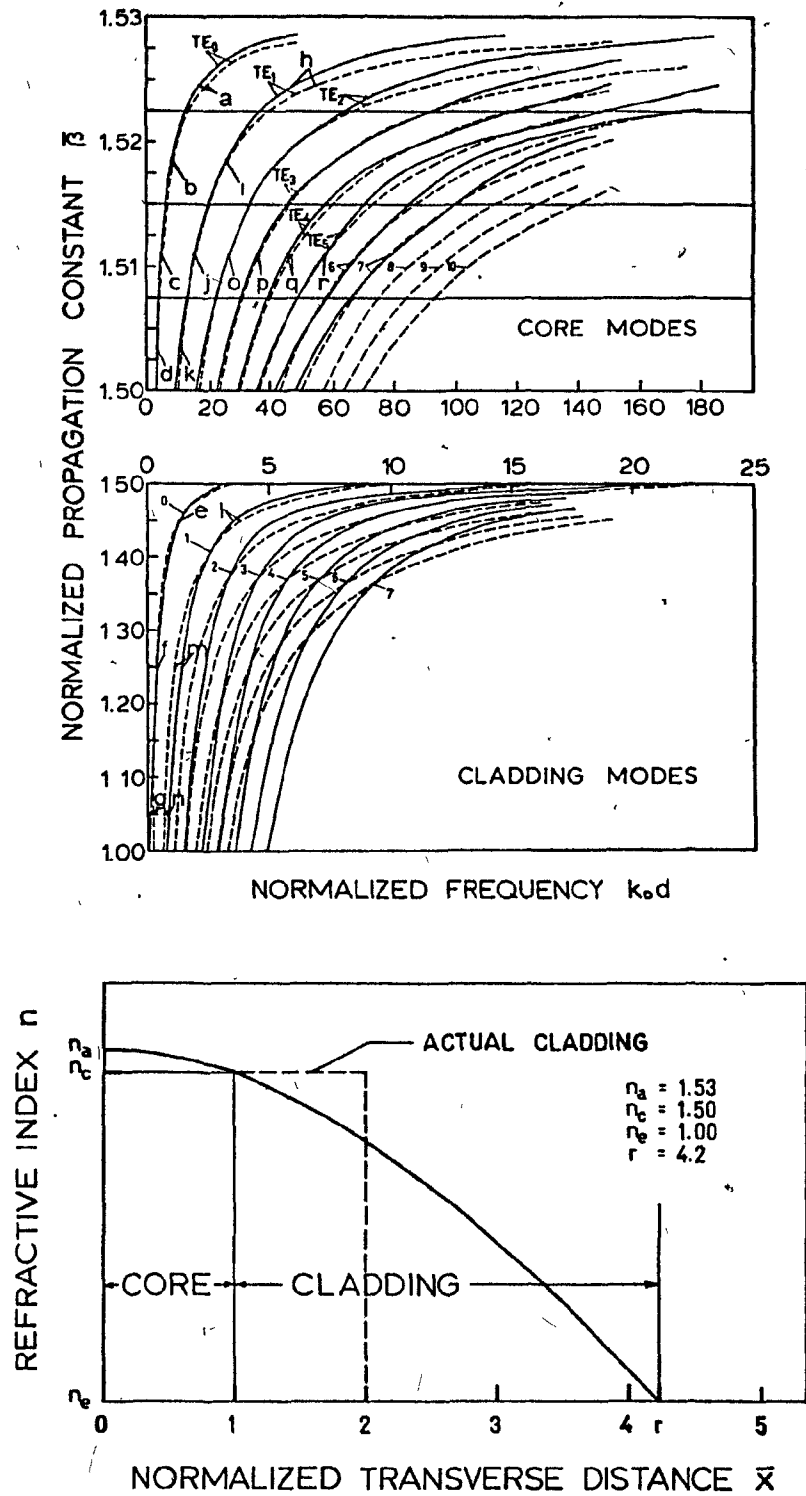


Figure 4.1 Combination of the dispersion curves (Fig. 2.3) and the index profile (Fig. 3.1).

profile was chosen to be merely a continuation of the parabolic core profile as shown in the bottom diagram of Fig. 4.1. This is also the reason for the lack of agreement in the cladding modes determined by the two methods. Indeed, there is a crossing of these modes in the region $\bar{\beta} \approx 1.4$, which also corresponds to the approximate value of the refractive index at which the two cladding profiles intersect. The dispersion curves resulting from the WKB method (---) are to the right of those given by the step-index method above the crossing points, while below these points they lie to the left. This can be explained qualitatively by considering the difference between the fields occurring in the two profiles.

The alphabetically labelled points on the dispersion curves were chosen for the computation of the E and H fields for several TE modes. The important field characteristics associated with these are listed in Table 4.1. For a fixed value of $\bar{\beta}$ above the intersection between the WKB and the actual cladding profile used in the step-index method, the WKB field decays sooner, at a lower value of \bar{x} as can be verified by referring to the field plots in Fig. 4.2. This results because the turning point, which corresponds to the value of \bar{x} where $n(\bar{x}) = \bar{\beta}$, occurs for $\bar{x} < 2$ in the WKB fields, where $\bar{x} = 2$ is the position of the turning point for the fields in the step-index method. For a particular mode, the turning points, which are located symmetrically about $\bar{x} = 0$ and define the boundaries of the oscillatory field, are closer together in the WKB profile. This means that the same number of oscillations occur within a shorter distance than in the step-index

Table 4.1 : Important field characteristics

LABEL	$\bar{\beta}$	STEP		WKB					
		k_{od}	\bar{x}_t	k_{od}	\bar{x}_t	\bar{x}_p	D	H_{zN_t}	
TE ₀	a	1.5246	16.723	0.354	18.364	0.424	0.886	0.212	-0.574
	b	1.5185	8.064	0.612	8.634	0.619	1.294	0.310	-0.574
	c	1.5110	4.714	0.791	5.234	0.796	1.663	0.398	-0.559
	d	1.5035	3.384	0.935	3.758	0.940	1.965	0.471	-0.564
	e	1.4500	1.341	2.000	1.259	1.633	3.423	0.822	-0.569
	f	1.2500	0.425	2.000	0.376	3.055	6.471	1.569	-0.586
	g	1.0500	0.132	2.000	0.230	4.000	8.589	2.107	-0.589
TE ₁	h	1.5246	47.887	0.354	55.092	0.424	0.646	0.102	-0.459
	i	1.5185	25.133	0.612	25.902	0.619	0.943	0.149	-0.446
	j	1.5110	15.346	0.791	15.701	0.796	1.213	0.192	-0.456
	k	1.5035	10.543	0.935	11.275	0.940	1.433	0.226	-0.455
	l	1.4500	3.422	2.000	3.777	1.633	2.493	0.395	-0.481
	m	1.2500	1.377	2.000	1.128	3.055	4.697	0.754	-0.479
	n	1.0500	0.865	2.000	0.691	4.000	6.206	1.013	-0.386
TE ₂	o	1.5110	26.108	0.791	29.169	0.796	1.093	0.136	+0.413
TE ₃	p	1.5110	35.827	0.791	36.637	0.796	1.033	0.109	+0.401
TE ₄	q	1.5110	45.847	0.791	47.104	0.796	0.996	0.092	-0.388
TE ₅	r	1.5110	57.162	0.791	57.572	0.796	0.971	0.081	-0.375

method and tends to suggest WKB modes of shorter wavelengths, and hence higher values of k_0d . On the other hand, for a fixed value of $\bar{\beta}$ below the intersection, the turning point of the WKB field occurs at $\bar{x} > 2$ so that the decay is less rapid than in the field given by the step-index method since :

$$\gamma_{\text{step}} = \{\bar{\beta}^2 - n_e^2\}^{\frac{1}{2}} > \gamma_{\text{WKB}} = \{\bar{\beta}^2 - n^2(\bar{x})\}^{\frac{1}{2}}$$

where $n(\bar{x}) > n_e$ for $2 < \bar{x} < r$

This suggests WKB modes of longer wavelengths and hence lower values of k_0d . The solid curves consequently represent the actual cladding modes since they were derived by assuming the true cladding profile.

Although Fig. 4.2 shows only the fields for the TE modes, those for the TM modes are related through the principle of duality. For a given value of $\bar{\beta}$, k_0d is only slightly different in each case and so the normalized fields are also slightly different. For the scale used however, the difference is not very noticeable, and hence, the TM fields are not presented.

The discrepancies between the TE fields obtained by the two methods are due in part to the different values of k_0d obtained in the dispersion curves for a fixed value of $\bar{\beta}$, and in part to the basic difference between the two approximations. It should be also remembered that the WKB fields near the turning point \bar{x}_t result from the graphical construction used to eliminate the singularity as explained in section 3.1.1. The H_z fields exhibit discontinuities in their slopes at the boundaries between the various steps in the core. The actual H_z fields in the core should be smooth although discontinuities in the slope will

TE₀

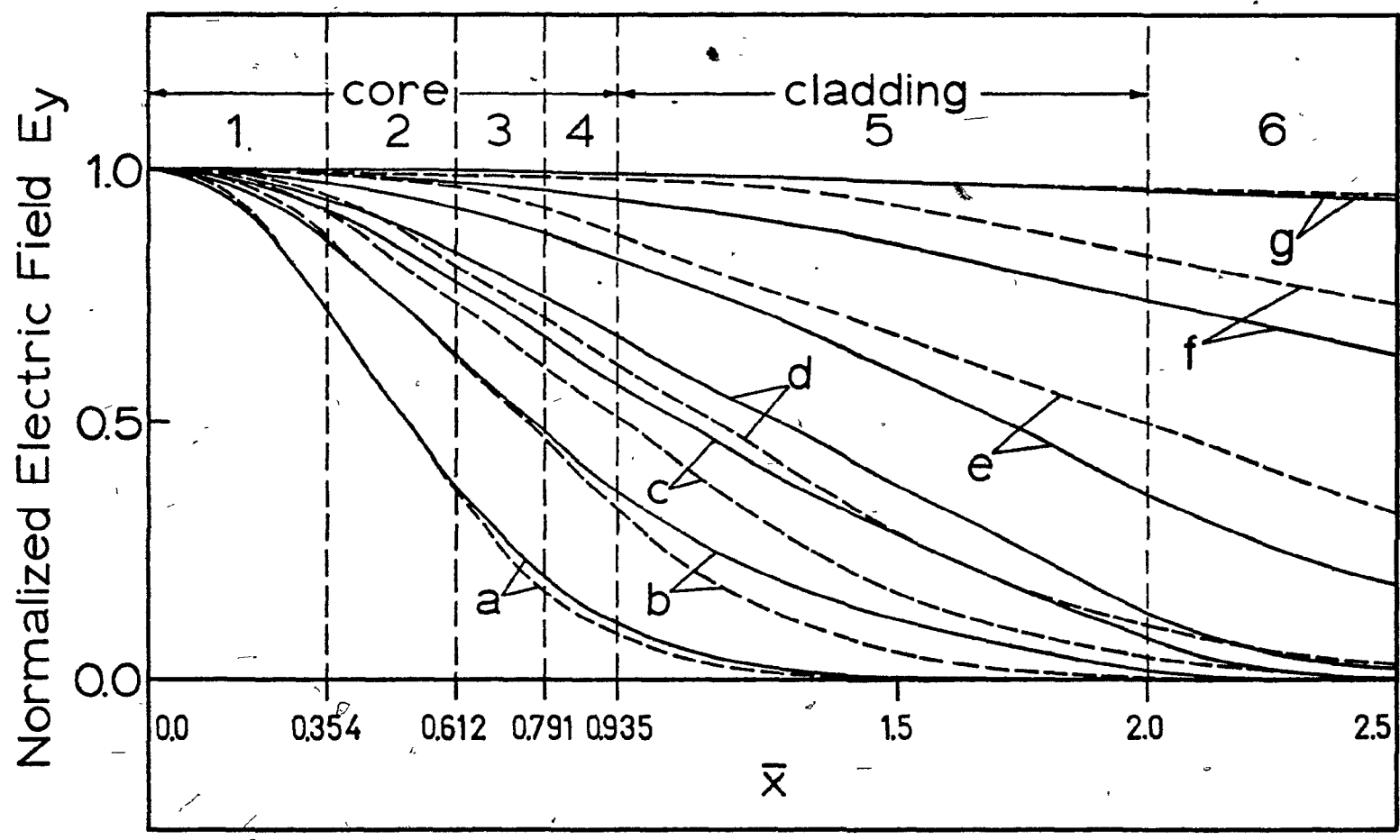


Figure 4.2(a) Plot of the E fields for the TE₀ mode using the step (—) and WKB (---) methods.

TE₁

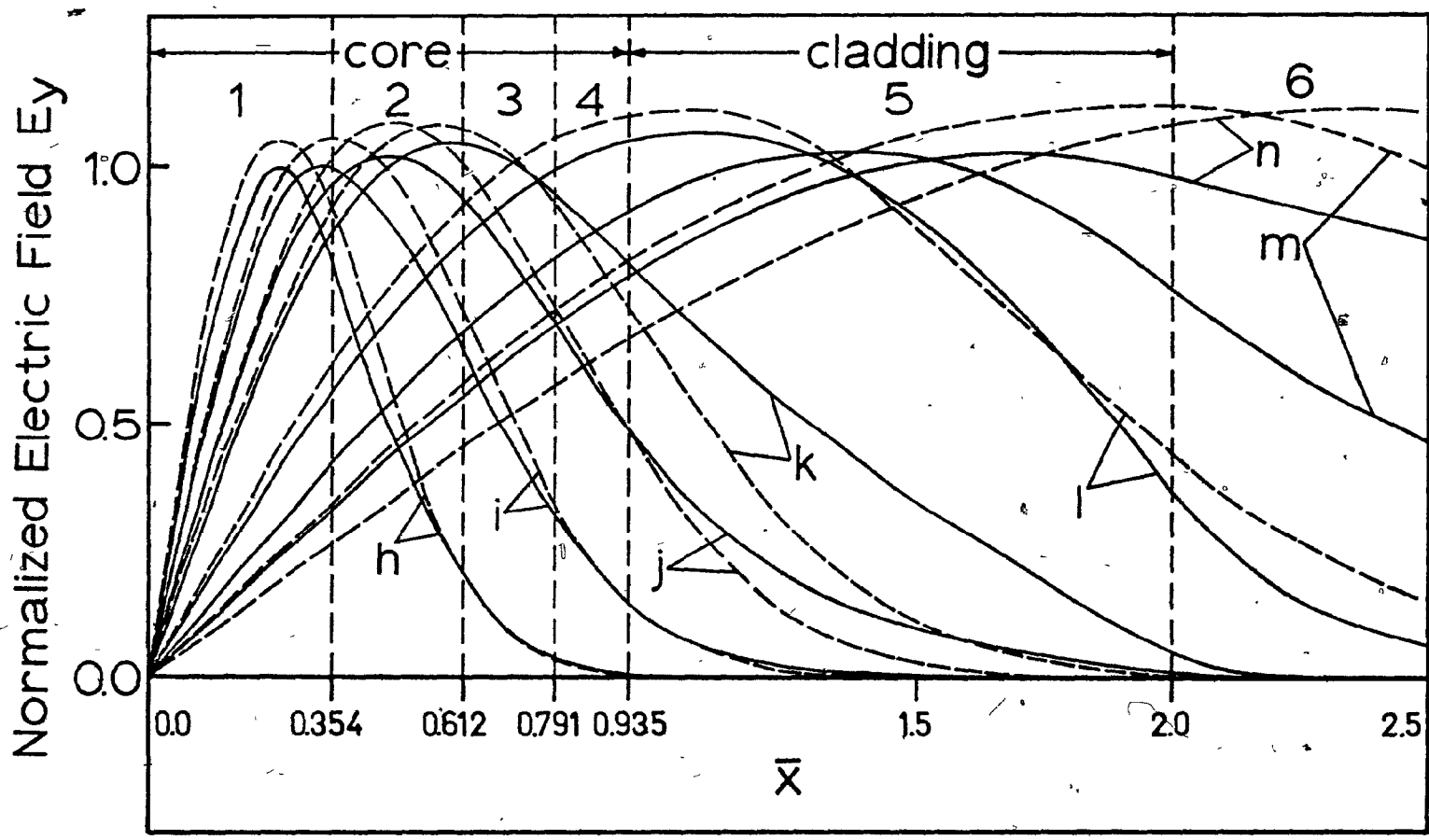


Figure 4:2(b) Plot of the E fields for the TE₁ mode using the step (—) and WKB (---) methods.

TE₀

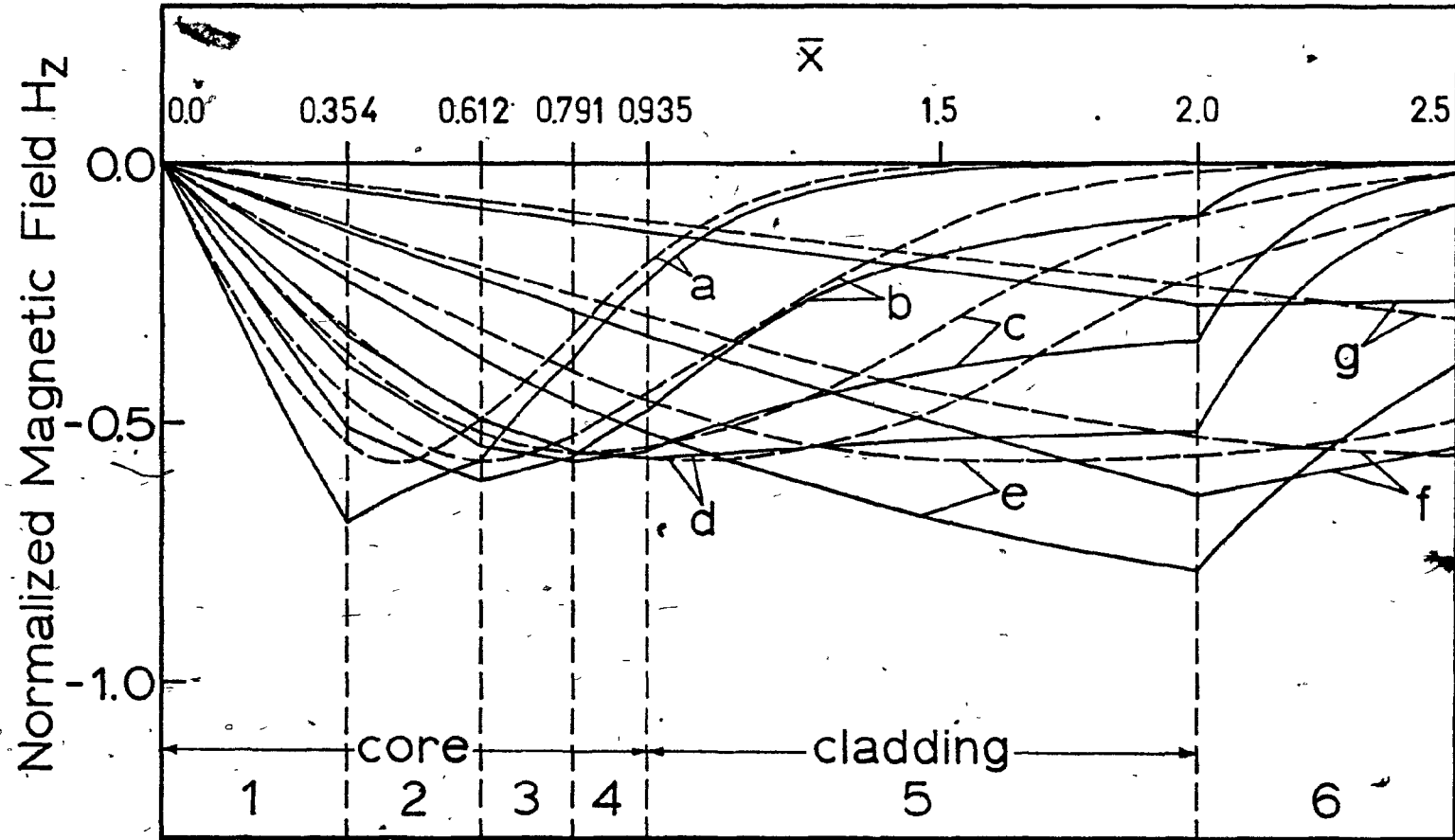


Figure 4.2(c) Plot of the H fields for the TE₀ mode using the step (—) and WKB (---) methods.

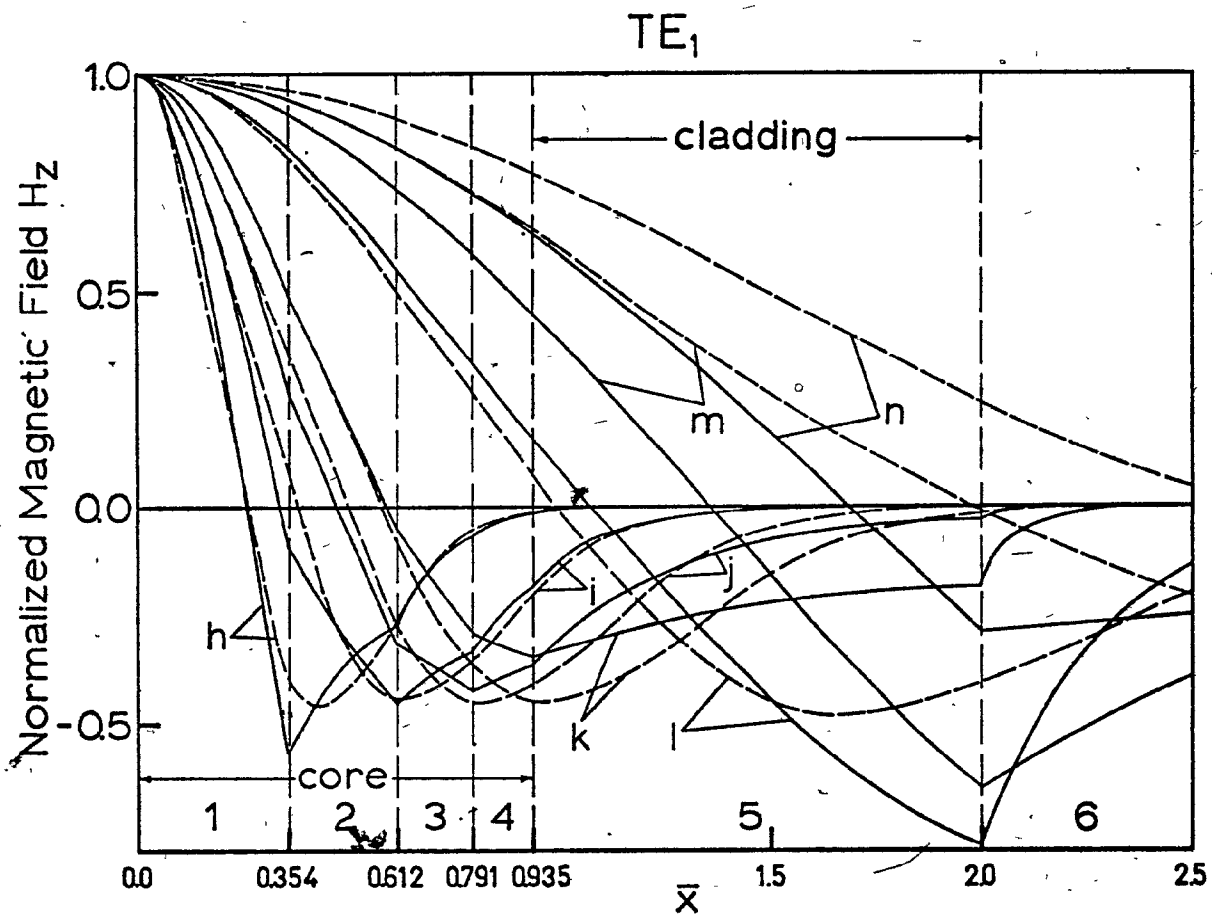


Figure 4.2(d) Plot of the H fields for the TE_1 mode using the step (—) and WKB (---) methods. 4-9

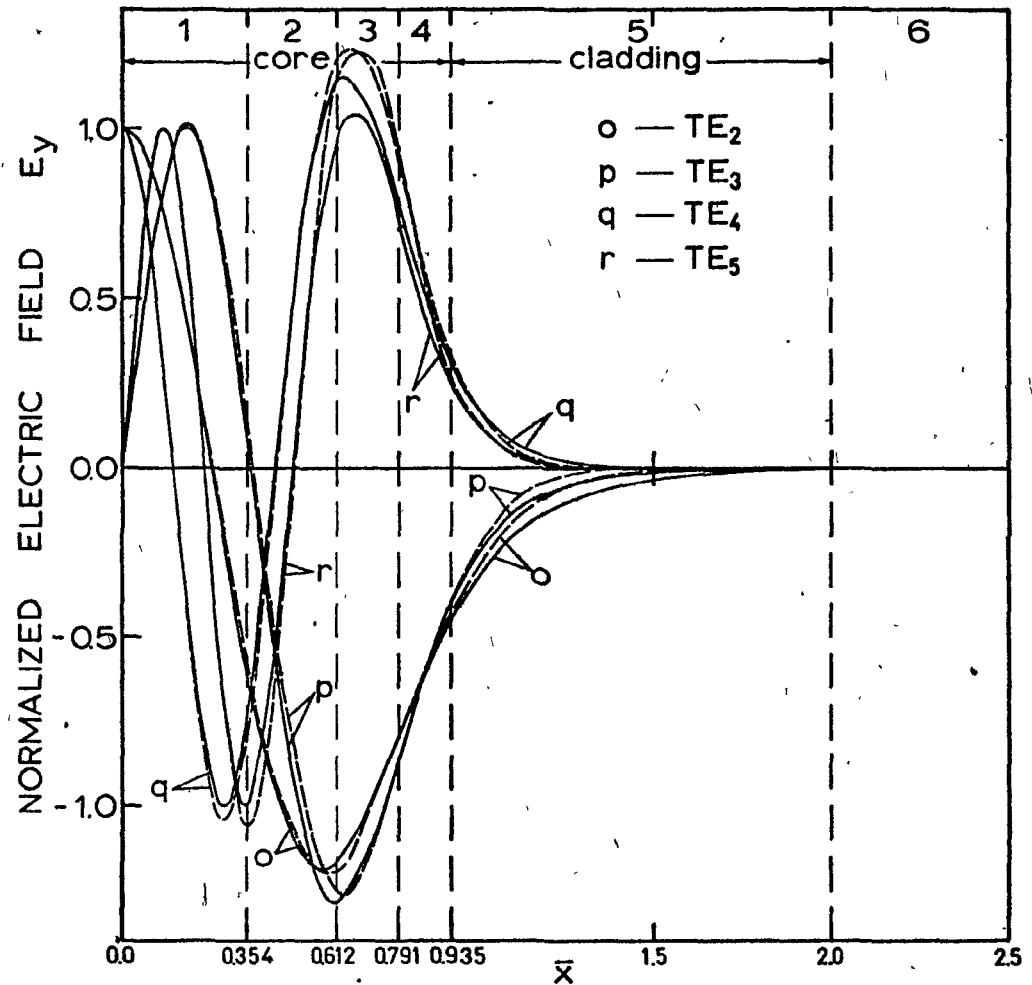


Figure 4.2(e) Plot of the E fields for the higher order TE core modes using the step (—) and WKB (---) methods.

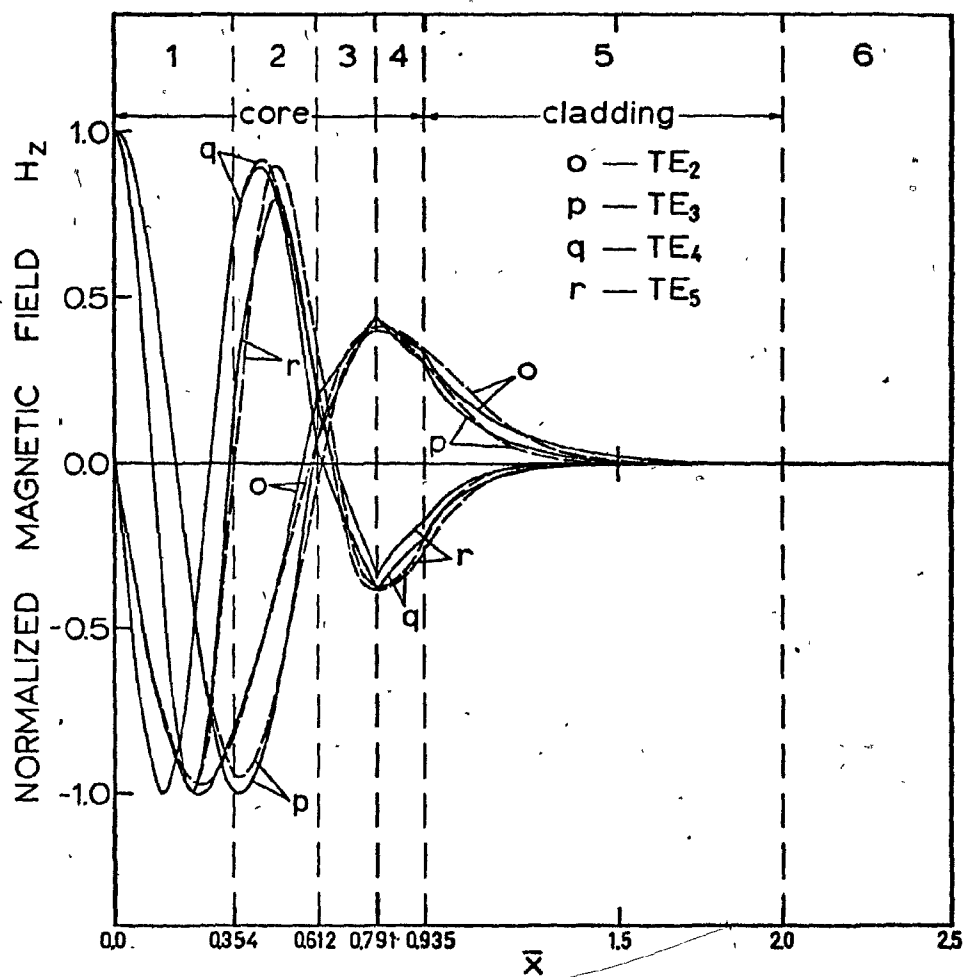


Figure 4.2(f) Plot of the H fields for the higher order TE core modes using the step (—) and WKB (---) methods.

still exist at the two cladding interfaces. The fields for the higher order modes show close agreement. This is due to the close agreement between the dispersion curves at the chosen points. The major difference occurs in the vicinity of the turning point. From Table 4.1 and the field plots it can be seen that for a particular mode, as $\bar{\beta}$ decreases, the turning point \bar{x}_t moves away from the center of the slab waveguide. As cutoff is approached, the corresponding field becomes broader and penetrates more into the cladding. Further, in the WKB method, the deviation D increases so that the singularity affects a larger portion of the field. On the other hand, for fixed $\bar{\beta}$, the turning point is fixed and the singularity has less effect with increasing mode number.

4.2 Conclusions

Two approximation techniques have been employed in the analysis of the propagation characteristics of an inhomogeneous symmetric slab waveguide, and these are found to be complementary.

The step approximation is useful in computing the dispersion curves of the core modes with low values of k_0d and for the cladding modes. The WKB approximation allows the computation of the core modes at about a tenth of the computing time (for $N = 4$), but for values of $\bar{\beta}$ approaching n_a (1.53) and near cutoff, substantial inaccuracies arise. This method, however, is especially useful for high order modes as the step method encounters some computational difficulties for large values of k_0d . For field computations, the step method required an average of 1.7 seconds of execution time per field, while the WKB method required

about 2.1 seconds due to the numerical integration process involved. Consequently, for field computations, the step method appears more advantageous especially since it does not involve turning point inaccuracies. However, for high order modes the WKB method is again useful since the singularity has not much effect and the step method is again affected by computational difficulties.

P A R T I I

DEPOSITION OF A MONOMOLECULAR-LAYERED-FILM

AND

THE DETERMINATION OF ITS BIREFRINGENCE AND THICKNESS

THROUGH ITS APPLICATION AS AN ANISOTROPIC OPTICAL WAVEGUIDE

CHAPTER 5
FABRICATION PROCESS

5.1 Film Chemistry

Only a brief description of the film's nature and coating mechanism will be given here, since excellent accounts of the theory of monolayer transfer giving schematic diagrams which help to visualize the film's molecular arrangement during coating, have been presented elsewhere (40).

According to Langmuir's method which was later developed by Blodgett (33)-(35), a single molecular layer (monolayer) of stearic acid is spread on the surface of a water solution containing barium (Ba) ions. The carboxyl group or "head" of each stearic acid molecule, touches the surface of the water. These react with the Ba ions to form the barium stearate (Ba-H-St) soap film. The thickness of the film is determined by the length and tilt of the hydrocarbon (CH₃) chain which extends outward from the "head", normal to the water surface. If a clean glass slide (made hydrophilic) is now raised slowly out of the water, the molecular heads will attach themselves to the glass if the film is maintained under a constant surface pressure. As the slide is raised, the water recedes slowly from between the glass and the film and the slide emerges completely dry, being coated with one monolayer of Ba-H-St. The second layer will be deposited as the slide is slowly dipped into the water. In this case, the slide surface, which has been rendered hydrophobic by the hydrocarbon chains, will adhere to the tips of those same chains of the film spread on the water surface. As a result, the film is folded back and forth on

itself as the slide is lowered and raised out of the water, so that each time, a new layer is deposited with molecules in successive layers being oriented in opposite directions.

5.2 Equipment and Procedure for Monolayer Deposition

The apparatus used to coat glass slides with successive monolayers is shown in Fig. 5.1. It consists of a Plexiglas trough used to contain the water solution or subphase upon which the monolayer is spread. A motorized dipping device has been set up to obtain smooth dipping at a controlled speed. Both the dips per minute and the number of dips are conveniently indicated. The bath temperature is maintained below 20°C by means of a pump which circulates ice-water through a cooling coil. In order to reduce contamination by dust particles, a Plexiglas sheet is used to cover the trough and the whole system is housed in a tent.

5.2.1 Equipment Considerations

The criteria upon which the trough design is based will become apparent by considering the various functions it must perform. Since the subphase will be contained therein, the trough material must be chosen so it does not introduce contaminants or in any way react with the subphase. Early workers used metal troughs which had to be protected by a paraffin wax coat and glass sheets so as to minimize metal ion contamination. Even minute metal ion concentrations will affect the film-making process. This problem can be eliminated by choosing a plastic material. In particular, Teflon offers the advantage of being chemically inert



Figure 5.1 Equipment for the deposition of multilayer films.

and both hydrophobic and oleophobic. Since plastics in general tend to deform, a rigid supporting structure is required. Plexiglas has been used in the present case as a matter of convenience and although no noticeable contamination has been detected even when the subphase was left standing in it for weeks, it must be kept in mind that plasticizers or mold-release agents and adhesives might be a source of contamination.

Since the film will be spread on the surface of the subphase, this surface has been made accessible by many workers by filling the trough slightly above the brim. This requires the tray to be made with great precision and placed on a vibration-free table. In addition, to prevent spilling over, if the material is not already hydrophobic, the edges must be waxed. If a strip of glass is now placed across the trough, resting on the edges, it will form a barrier for any surface nonsoluble material. This barrier can be used to clean the surface by sweeping it along the length of the tray. In the present design, the liquid surface is kept below the brim. This facilitated both the trough construction and in certain ways, the film coating process. The need to maintain a constant subphase level and reduce vibrations, is not so stringent. The edges of the trough need not be waxed and further contamination is avoided especially since benzene has been used as a spreading solvent for the stearic acid and if it would come in contact with the waxed edges, it would spread wax out into the film. However, with this arrangement, the barriers had to be specially designed to sink through the surface while being supported by the trough edges. In addition, the passage of surface material at the barrier edges was minimized by means

of rubber strips glued to the barrier. The ratio of the trough surface area to volume was maximized by making the trough only 9 mm. deep except for a small section where the slide is dipped and into which the cooling coil is placed.

In the design of the automatic dipping device, it was necessary to ensure that excessive vibrations were not transmitted to the slide being dipped, as this would introduce irregularities in the film. The motor was therefore mechanically isolated from the system except for a very elastic driving belt. This in turn required that the slide holder assembly be balanced with an appropriate counterweight so that the turning force be maintained nearly constant. A smooth sinusoidal dipping motion was obtained as a result and its amplitude (or stroke) is continuously adjustable from zero to 4 cm. by means of an eccentric chuck.

Since the city cold water was not available, an ice bath was provided along with a pump to circulate cold water through the cooling coil. This coil, being made of 1/8" copper tubing, had to be coated with a thin layer of plastic to prevent metal ion contamination while at the same time, allowing sufficient heat transfer.

5.2.2 Method of Monolayer Deposition

Although there has been much work in recent years on the manufacture and analysis of thin multilayer films (40)-(44), the best sources for a detailed description of the technique and problems involved are still the original papers of Blodgett and Langmuir (33)-(35). Throughout the course of this work, these have been carefully referred to and

the method to be presented follows the same lines except for a few modifications which facilitated the process. It must be clearly understood that the purpose of this work was not to improve upon this existing technique, nor try to explain some of the subtle problems encountered, as both the facilities and expertise in this field were lacking. Rather, the purpose was to understand and set up this film-making process with the aid of the existing literature and check the film's feasibility as an optical waveguide material.

Right from the outset, the need for extreme cleanliness and care to avoid excessive contamination cannot be overemphasized. If it is remembered that the invisible film which is spread on the subphase is one molecule thick, it is readily realized that even minute traces of surface contamination will completely disrupt the film structure. Grease from skin, hair, and in general a greasy environment, will quickly spread on a clean water surface. All apparatus must therefore be scrupulously cleaned with strong oxidizing agents or detergents and then rinsed thoroughly.

The preparation of the aqueous subphase will first be considered although the details for the preparation of the various chemicals will be found in Appendix C.1. The solution which Langmuir and Blodgett found to be most suitable to build up thick films of up to 3000 layers, is a water solution containing : $30 \mu\text{M}$ (30×10^{-6} moles/liter) BaCl_2 which is the source of Ba ions, $200 \mu\text{M}$ KHCO_3 the buffer, the pH is set to 6.8 by addition of dilute HCl or NaOH, and $2 \mu\text{M}$ CuCl_2 which introduces a slight trace of Cu ions. It is interesting to note that although larger concentra-

tions of Cu ions ($> 10 \mu\text{M}$) cause the film to slip entirely, small amounts are actually needed to help prevent the fogging and cracking of films which are over 200 layers thick. In order to maintain the copper concentration constant as successive films are spread on the subphase, it is necessary to inject a light sprinkling of copper sulfide (CuS) along the bottom of the tray. This precipitate is only slightly soluble and should maintain the copper concentration at the proper level. The commercially available CuS had to be initially thoroughly washed since it contained substantial amounts of copper sulfate which is highly soluble. All the chemicals used should be reagent grade to insure the highest purity. The water which was used in this solution was distilled once and then purified by passing it through a resin deionizer. Although the specific resistance of the water exceeded the 700,000 to 1,000,000 ohm-cm. specification of Langmuir and Blodgett, organic matter is introduced by the resin deionizer which might affect the process. Others using this solution (41) found that the built-up films of Ba-Cu-H-St monolayers were extremely uniform and stable.

The stearic acid film can be spread on the surface of the subphase by first dissolving it in a spreading solvent like benzene or n-hexane. It is critical that this solvent be extremely pure as contaminants will disrupt the film structure. Even highly purified commercial grades will pick up greasy contaminants during packaging and handling. It might therefore be necessary to repurify the solvent in the lab before use. Once the stearic acid solution has been prepared, it is delivered to the surface by means of a micropipet held just above the surface.

Injection below the surface is to be avoided. The solution is fed rapidly so that it always remains visible, forming a few lenses on the surface. As the solvent quickly evaporates from these, the stearic acid is released as a single molecular layer which spreads out over the whole surface. In this case, 0.1 ml. of a benzene solution was used to cover an area of 2800 cm². Since stearate molecules have an area of 20×10^{-16} cm², the solution required a concentration of 0.023 M which was near the 0.03 M value used by others (41) who noticed that unsatisfactory results were obtained when the solution was too dilute.

As was pointed out previously, the film must be kept under a suitable constant surface pressure as it is being deposited on the slide. Langmuir ingeniously suggested the use of a hydrophilic oil like castor oil or oleic acid to act as a surface piston, exerting a constant pressure on the film. When a drop of this oil is transferred to the water surface, it breaks up into many tiny lenses and spreads as a monomolecular layer of oil throughout all the available area until an equilibrium surface pressure is established. Oleic acid compresses the film to 30 dynes/cm. while the more viscous castor oil exerts 17 dynes/cm. The surface pressure can be accurately measured by using a film balance. There are two fundamental types, the Wilhelmy type and the Langmuir type (40). The former yields an absolute measurement by determining the force on a plate partially immersed in the film-covered liquid due to surface tension. This is then compared to the force observed from a clean surface. In the latter method, the force exerted on a movable barrier separating the film from the clean surface is measured.

In an attempt to prevent oil contamination of the film,

Blodgett employed a waxed silk thread floating on the surface to isolate the film from the oil. This technique was used initially but it was found a bit unreliable and tedious, especially since many hundreds of layers were to be deposited, each spread film yielding about 50 layers. It was found that the oil was not completely blocked by the thread since any tiny kinks or sections where wax had been removed allowed the passage of oil. The thread was replaced by a floating barrier cut from a polyethylene sheet 9 mils thick (see Appendix C.3) and resting on the surface across the tray. Although there is necessarily a slight gap between the barrier and the tray edges, any oil which passes through should not penetrate too deeply into the film since the pressure is at equilibrium. As a precaution however, the film is never used up completely and a margin of about 15 cm. is left between the slide and the barrier yielding an average of 60 layers per spread film.

One other delicate area of concern is the deposition of the first layer. The glass slide must be scrupulously cleaned so that all grease and contamination be removed. A cleaning procedure which has been found adequate for this purpose is outlined in Appendix C.2. However, even with this thorough cleaning, the film did not seem to adhere strongly to the slide as it was raised very slowly out from the film-covered sub-phase. Langmuir found that the initial layer was more readily deposited from alkaline water ($\text{pH} \geq 8.5$) and for glass of high refractive index. The glass that is used in the present work is low index fused quartz to satisfy waveguide considerations. As suggested by Langmuir, it was found that if after depositing a few layers, the film was rubbed down using

tissue paper until no visible trace of the film remained, the slide would be left with a monomolecular layer which provides a very good foundation for building good films. The first layer could also be deposited by rubbing down molten wax or preferably ferric stearate, however this would make the first layer different from the rest.

Dipping speed, pH of the subphase, and its temperature are important parameters which affect monolayer deposition. After the slide surface has been rendered hydrophobic by rubbing down a film, the second layer is deposited as the slide is dipped slowly (1/10 r.p.m.). The deposition of the layer can be verified by observing the motion of the floating barrier which separates the film and oil monolayers. In addition, as the slide is lowered, the film is pushed downward and as it is raised, the opposite occurs. The meniscus therefore gives a good indication of the success with which the monolayer is being deposited. If the meniscus is not uniform, with an equal contact angle throughout, but rather shows unevenness, has an erratic jumpy behaviour, and especially during ascension, shows uneven shedding of water so that sections of the slide remain wet, then poor quality films will be obtained having many irregularities.

After a few first layers at slow speed, good quality films were deposited at a rate of about $1\frac{1}{4}$ r.p.m. . The speed is limited by the rate at which the ascending slide sheds water. Speed is greatly affected by temperature and pH. With decreasing temperature and increasing pH the speed increases since the film becomes more rigid, although very rigid films will completely slip. It was found that a pH range of 6.8 to 7.2 and a temperature range between 17°C and 20°C will yield good results.

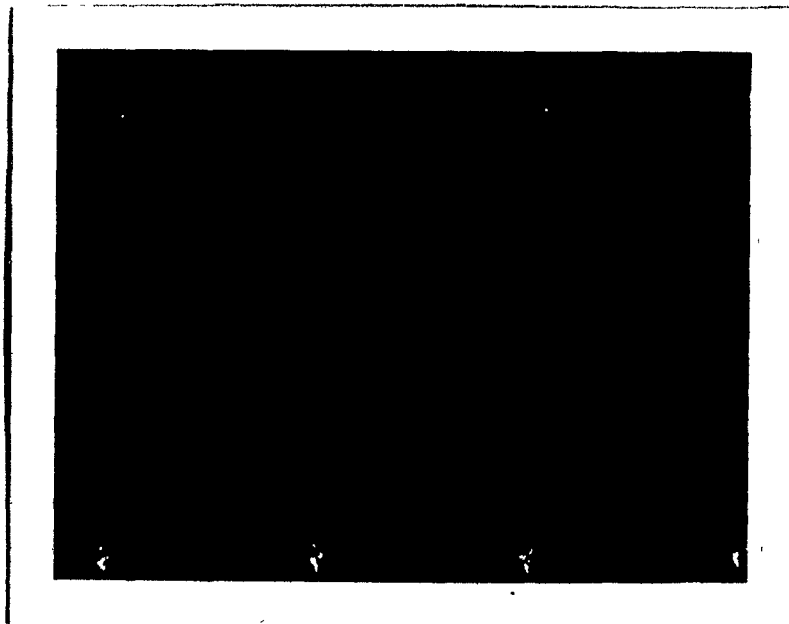
Having developed the major points which affect the film deposition process, the detailed procedure which was used in the present work has been outlined in Appendix C.3. It is certainly not intended to be the best procedure but rather a first attempt at establishing a fabrication system which has proven satisfactory. Suggestions as to certain improvements and modifications which could be made will be given in the conclusions.

5.3 Film Quality

Good quality films are uniform, with no gaps or irregularities, and have a minimum of contamination from foreign matter such as dust particles and oil droplets. To obtain films of this quality requires a great deal of effort with respect to the cleanliness of the equipment and environment in general, the preparation of the substrate surface, the maintenance of the proper pH, temperature and concentration levels in the subphase, and the special attention required to minimize oil contamination during the film deposition process.

A good indication of the film's quality can be obtained by observing the film under the microscope. Fig. 5.2(a) is a picture of a film with 57 layers, having a gap where no film has been deposited. Many similar gaps in the film occur throughout the whole slide and are due to poor cleaning of the substrate surface. This film was obtained by rubbing down some 50 layers of an even more poorly coated film deposited on a slide which had not been cleaned by the method outlined in Appendix C.2. When a clean slide was used, these gaps were not observed.

(a)



(b)

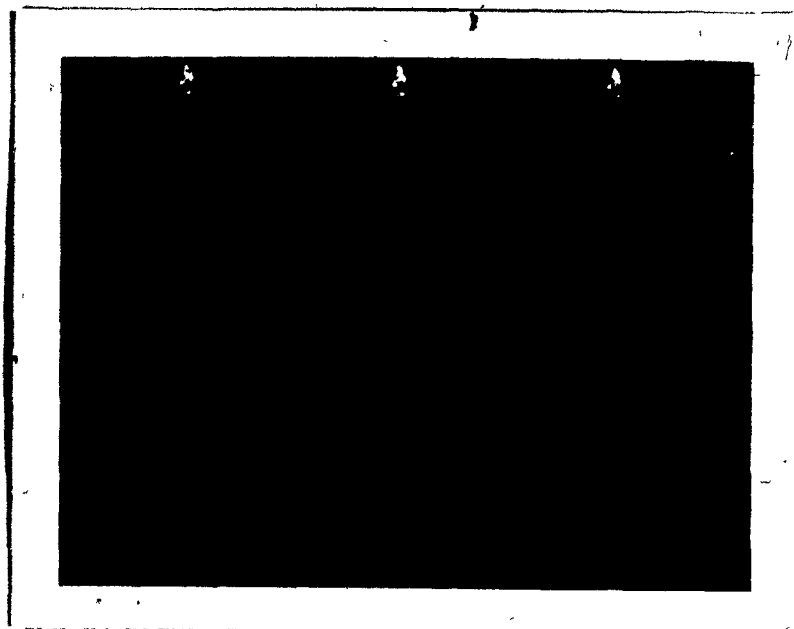


Figure 5.2 (a) Gap in a 57 layer film. X 200
(b) "Fogging" and "cracking" in a 280 layer film when
no copper ions are added. X 100

(c)

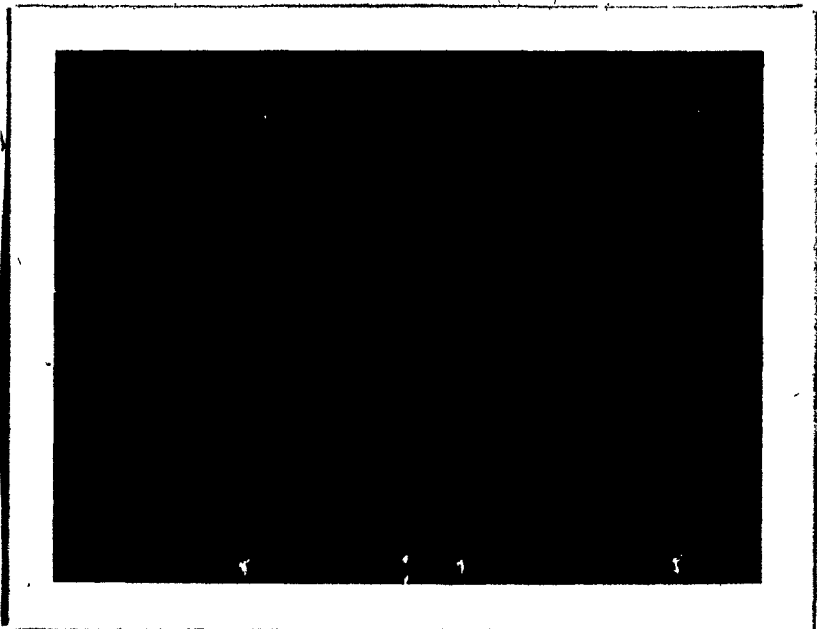


Figure 5.2 (c) "Fogging" at 600 layers even with copper ions added. X 200

This picture also shows the presence of some tiny specks even after a mere 57 layers. Blodgett labelled this condition "fogging" as it gave the films a fogged appearance. She noticed it in films having greater than 50 layers and said that it was successfully prevented by the introduction of a slight trace of copper ions as was mentioned previously. Fig. 5.2(b) shows cracks in a 280 layer film in addition to the specks. This condition, labelled "cracking", could also be prevented by the addition of copper ions. From the present work it was found that although "cracking" was completely eliminated by the copper ions, "fogging" was only greatly reduced but was still very much present. This can be readily observed from Fig. 5.2(c), a picture of a 600 layer film with copper ions present. The cause of this "fogging" condition is still somewhat of a mystery. It has been suggested (42) that this condition is due to the gradual crumpling and crystallite formation in the spread monolayer and it is advised that a new film be spread after about 20 layers. This seems to be a very possible cause although contamination by foreign matter such as dust particles and oil, especially in the benzene solution used to spread the film, could certainly cause irregularities in the film's layers. Even though slightly better quality films might be obtained by following these recommendations and being extra careful to minimize contamination, what is really needed are some major modifications to this rudimentary system which has been set up as part of a feasibility study on the possible use of this film to make thin-film waveguides. These modifications, to be discussed in the conclusions, have been suggested in part by the elaborate systems being

used by present-day workers who manufacture the film for biological studies, and studies into its possible applications, some of which were listed in the introduction.

CHAPTER 6FILM CHARACTERIZATION THROUGH WAVEGUIDE MODEEXCITATION AND MEASUREMENT6.1 Refractive Index and Thickness Measuring Techniques

Three well established techniques for the thickness determination of thin films are : ellipsometry, interferometry, and X-ray diffraction. Each of these has been used to determine the thickness of barium stearate multilayers. Blodgett and Langmuir (33),(34) measured the angles at which the intensity of polarized monochromatic light reflected from films having known numbers of layers, was a minimum. By taking the film's anisotropy into account, they were able to determine both the thickness and indices quite accurately. Two other methods which have been used (41) are the Mattuck and Hartman methods. The former is essentially a two-beam interferometric method whereby the measurement of the fringe shift caused by a film deposited on a stepped multilayer plate, results in the determination of the thickness and index of the film. The method is useful for the analysis of very thin films (10 to 250 Å) while the latter method, which is a polarimetric method, permits the measurement of thick multilayers. Tolansky's multiple-beam interferometric technique (45) has also been used (46) for the thickness measurement of fatty acid multilayers, and gives much higher precision than the two-beam fringe methods due to the increased sharpening of the fringes. However, this, like the previous methods, is plagued with the need for an accurate knowledge of the refractive index which in turn is complicated by the film's anisotropy.

To overcome this difficulty, Srivastava and Verma (36) have performed high precision thickness measurements on various types of multilayers including barium stearate by using a special technique which Tolansky formulated that is independent of the refractive index, anisotropy, heterogeneity and lack of transparency of the film. In this method, a stepped multilayer plate was prepared whereby a greater number of layers was present on one part of the plate and an almost opaque silver coating was deposited. The step thickness was then obtained through the observation of fringes of equal chromatic order after white light illumination. This light was reflected from the surface and never passed through the film making this method independent of the film's optical characteristics. These same workers have also performed X-ray diffraction studies to determine the molecular chain length and have found these results to agree within experimental error ($\pm 0.5 \overset{\circ}{\text{A}}$) with the interferometric values of the monolayer thickness. This implies that the molecules in the monolayers are perpendicular or very nearly so since if a substantial tilt were present, the layer thickness would be less than the molecular chain length.

One final method which has been used extensively to determine the optical constants of reflecting surfaces and film-covered surfaces, is ellipsometry (47). Both the refractive index and thickness of the film can be determined through the observation of the changes in the polarization of the reflected light. The advantage of this technique is that the film-coated surface can be scanned so that not only the film's thickness, but also a measure of its evenness can be obtained. In addition,

the film need not be coated with additional layers or be silvered as this would preclude its use as a thin-film waveguide. The required measurements are also relatively easy to perform although a precision retardation plate and polarizers are needed. Ellipsometric measurements have been performed (47) with accuracies in thickness down to 1 Å and 0.002 for the refractive index. In recent years, biologists (43), (44) have carried out studies on biological surfaces including barium stearate multilayers with the aid of ellipsometry, and found it to be a convenient tool to perform surface studies. However, the ellipsometric theory used for these measurements did not take into account the film's birefringence but assumed it to be optically isotropic with a value of index midway between Blodgett's values. Reasonable agreement in thickness was obtained as the anisotropy is not too pronounced. In order to obtain a better appreciation for the method and look into the possibility of its use as a thickness measuring tool, a detailed analysis of the isotropic theory was carried out (48) and a computer program written to generate a Ψ - Δ plot from which the thickness and index could be immediately obtained from the experimentally determined Ψ and Δ , the amplitude and phase of the ratio of the Fresnel reflection coefficients for the TE and TM rays. However, preliminary measurements proved to be very inaccurate due to the difficulty in making precise measurements. One reason for this is that the difference in the refractive index of the substrate and film is only about 0.05 yielding a very low reflection from the film-substrate interface. In addition, a high precision, calibrated compensator and polarizers were needed since the accuracy required is of the order of

the limiting values given previously. Even with better equipment, it is anticipated that the film's anisotropy and lack of homogeneity in preparation will make the accuracy much inferior to that of the other techniques. Engelsen (49) has recently developed the ellipsometric theory for anisotropic films and has carried out experimental measurements on some of Langmuir's multilayer films with the aid of an elaborate computer program to fit the experimental data. He obtained accuracies in the indices of the ordinary (TE) and extraordinary (TM) rays of ± 0.005 while the thickness was accurate to a fraction of an Angstrom. These measurements were performed on films less than 150 layers thick, and the results were compared with those given by the isotropic theory showing it to be quite inaccurate.

Recently, a method of measuring the refractive index and thickness of thin transparent films by observing the interference pattern in the light scattered by the film has been described (50). This technique renders an accuracy of 1 part in 10^3 for the index and 1 part in 10^2 for the thickness. For inhomogeneous thin-film waveguides, the refractive index profile was determined by using an optimization algorithm on the measured reflection coefficient data (51).

The current work in integrated optics and thin-film waveguides has caused the emergence of a new, highly accurate method of thin-film index and thickness measurements. P. K. Tien (24), (32), through the development of the prism-film coupler, has been able to excite and observe waveguide modes in semiconductor and organosilicon films. These modes are associated with discrete angles of the incident light beam

which are in turn related to the film's thickness and refractive index through the waveguide theory. By optimizing these quantities with the aid of a computer program to yield the best agreement between the theoretical and experimental angles for the first four modes, he determined the index with an accuracy better than one part in 1000, while for the thickness it was better than 1%. This same technique was used in the present work to determine the refractive index and thickness of barium stearate multilayers deposited on a fused quartz substrate. In this case however, the theory for an anisotropic slab waveguide was used. Many experimental measurements had to be taken due to some difficulty in obtaining accurate, reproducible data. Despite this, the experimental and theoretical agreement has turned out to be reasonably good. As will be shown, the method which has been used to evaluate the thickness and index treats these two parameters independently. This is very important since the thickness was not accurately known due to possible inhomogeneities in the film structure and also as a result of the possible deformation introduced by the coupling method as will be described in the next section.

6.2 Light Coupling, Mode Observation and Measurement

6.2.1 The Prism-Film Coupler

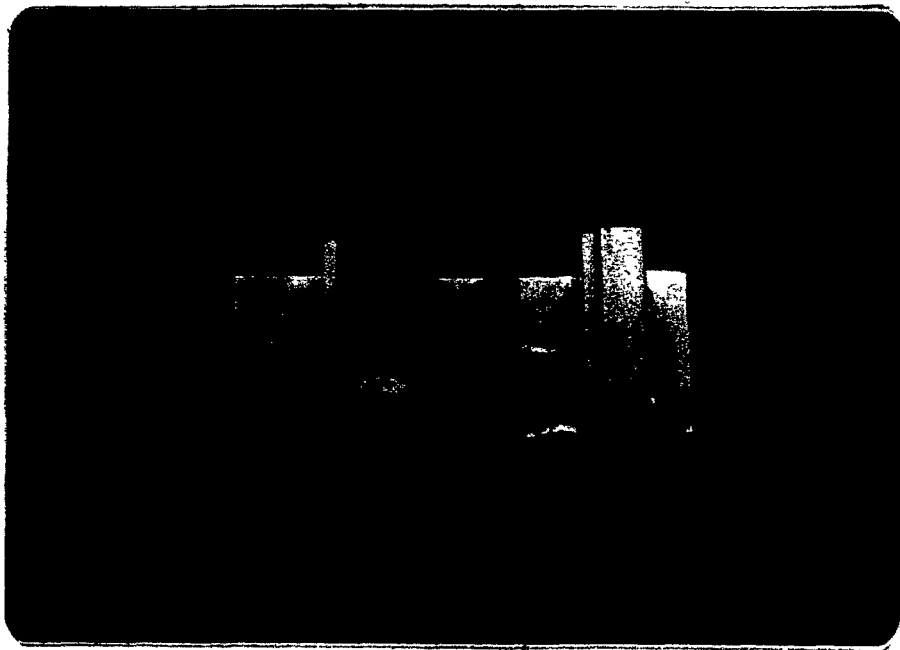
Various methods have been devised to efficiently couple a laser beam into a thin-film waveguide. The method which has been used in this work is the prism-film coupler developed by P.K. Tien (5), (24), (52), (53) and R. Ulrich (52), (54). In this method, a prism of slightly

higher index than the film, is mechanically compressed against the film such that the intervening gap is reduced to approximately half a wavelength. The reflection of light at the prism base is thereby frustrated and energy is coupled into the film through the evanescent fields in the gap. This transfer of energy or "optical tunneling" between the prism and the film, will only occur for certain discrete angles of the incident beam on the base of the prism. To satisfy the boundary conditions, the tangential field components must be continuous across the prism-film interface. As was discussed in the first part of this work, due to the finite thickness of the waveguide core (or film), only certain values of the normalized propagation vector $\bar{\beta}$ are allowed, which in a ray picture correspond to discrete ray angles in the film. The incident ray angles allowed in the prism are then just given by Snell's Law. Tien has termed these allowed angles "synchronous directions" since at these directions of the incident beam, the propagation vector is continuous through the prism-film interface. With this method, an optimum theoretical coupling efficiency of 81% has been predicted (5).

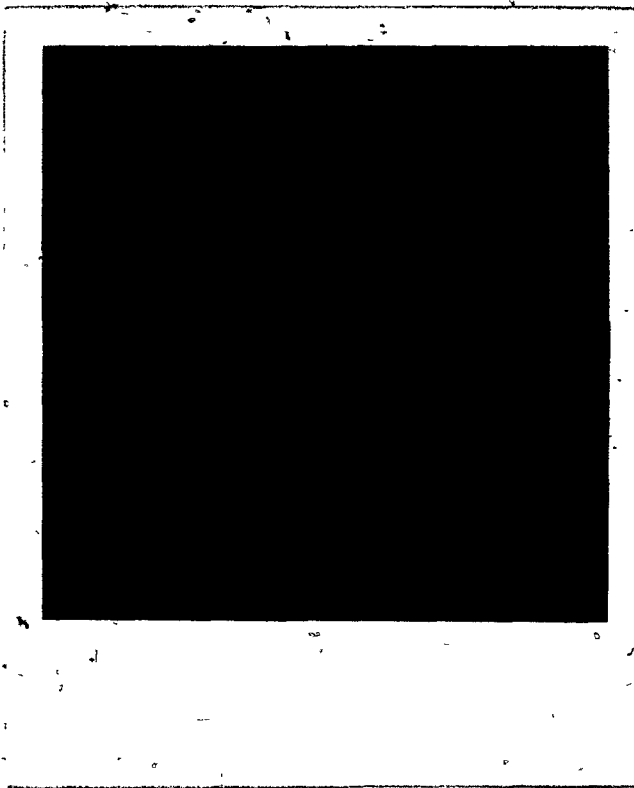
Another coupling method which has the same maximum excitation efficiency, is the grating coupler. Etched gratings made with photolithographic techniques (55), or photoresist gratings fabricated by a holographic method (30), (56), offer the advantage of being a more rugged, convenient, and practical coupling means. This is also true of the tapered film coupler (57); however only the prism-film coupler has been used to excite the waveguide modes in the multilayer film because of the difficulty in implementing the other methods. The prism coupler

itself requires very delicate adjustment due to the soft nature of the film.

A picture of the device used to compress a 60° prism onto the film-coated quartz slide, is shown in Fig. 6.1(a). Pressure is applied by means of a screw having a plastic tip to avoid scratching or possibly breaking the slide. The film, which is sandwiched between the slide and the prism, remains separated from the latter by a considerable gap due to dust particles, irregularities in the film, and unevenness in the slide and prism surfaces. It is therefore necessary to apply sufficient force to reduce the gap at the pressure point to less than half a wavelength. A dramatic indication of the behaviour of the gap around the pressure point can be obtained by observing Newton's rings as has been demonstrated in Fig. 6.1(b). These rings should be circular, indicating a smooth increase of gap with increased radial distance from the pressure point. If there are major irregularities in the film, the interference fringes will be distorted. The pressure should be increased until the observed reflection at the prism base is just frustrated at the pressure point. It is not possible to avoid some slight damage to the film since it is very soft and at those points where microscopic dust particles act as spacers, film damage is inevitable. This is not too serious as long as a major part of the area at the pressure point is not affected. If however, slightly too much pressure is applied, the crystal structure in the film will be permanently deformed in some areas due to direct contact with the prism base, and when the pressure is released, sections of film will be removed by adhering to the prism. Fig. 6.2(a) is a



(a)



(b)

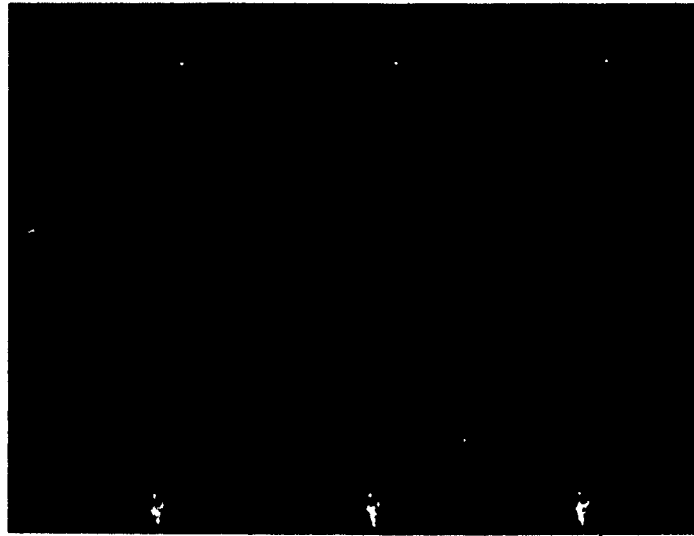
Figure 6.1 (a) Prism-film coupler assembly.

(b) Newton's rings around the pressure point.

microscope picture of the film area around the pressure point. It can be seen that there are many points of contact where the film has been removed due to a slight overpressure, although a few of the smaller damages would still be present even with proper pressure applied. An expanded view of the larger central area where the major damage has occurred is shown in Fig. 6.2(b). From this it can be observed that the film is in fact very brittle and breaks by cracking into many tiny sections as is expected from a crystalline film.

The optical tunneling which occurs between the prism and film at the pressure point is reciprocal. In other words, the energy which is transferred to the film can also tunnel back to the prism through the evanescent field in the gap unless this is prevented by increasing the size of the gap outside the area of illumination by the incident beam. Tien (5) used a right angle prism and applied the pressure with a knife edge less than 1 mm. from the sharp rectangular corner of the prism. In this way, the energy in the semiconductor film after the prism's corner, was totally decoupled from the prism and decreased only as a result of scattering and absorption losses in the film. This was attempted with the multilayer film without success as might have been anticipated since the film is very soft and the corner of the prism just digs into the film destroying it completely in this region. Unlike the previous case where the prism was uniformly supported by a large contact area around the pressure point, here the support is only on one side. One way of getting around this problem would be to use the 60° prism as before, after having made a tiny groove in the base which would rest just above

(a)



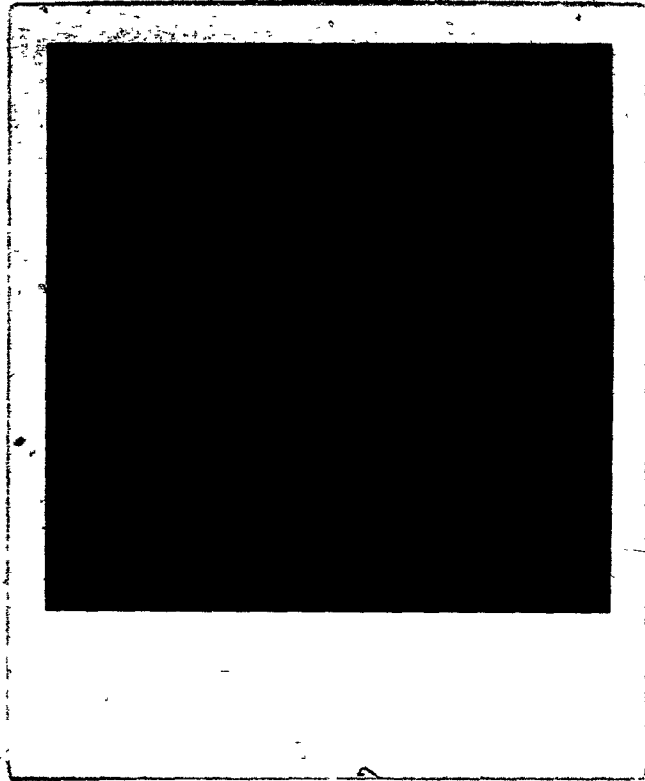
(b)



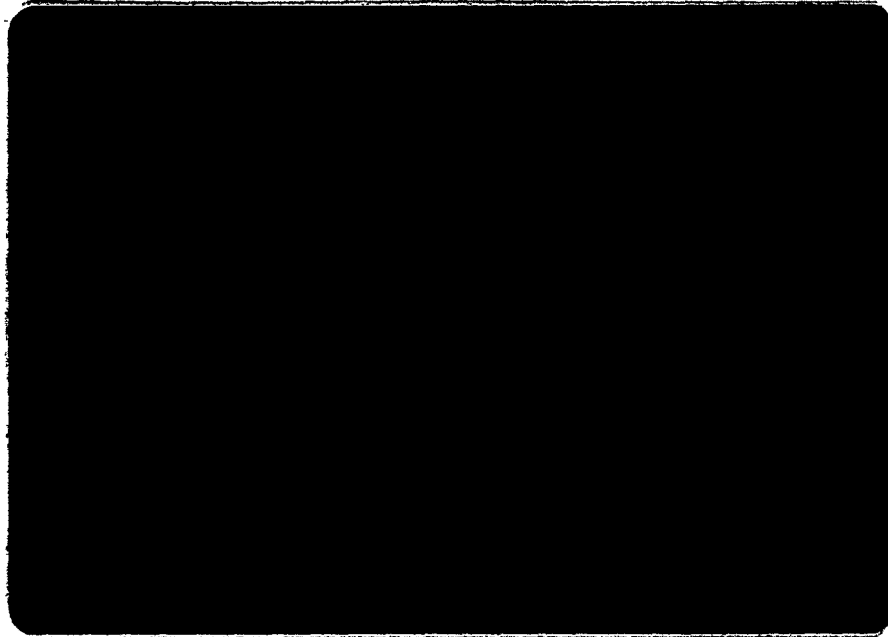
Figure 6.2 (a) Film damage due to a slight overpressure at the coupling point. X 40, 109 layers
(b) Expanded view of central damage showing the film's brittle nature. X 400, 109 layers

the decoupled beam in the film. However, even without this operation, the decoupling as demonstrated by Newton's rings, was sufficient to permit a 3 cm. streak in the film as shown in Fig. 6.3(a).

The slide was coated with 109 layers yielding single mode operation very near the cutoff of the first mode, the TM_0 mode. As more layers were added, the mode was brought farther away from cutoff which means that the evanescent field in the gap due to the energy in the film, would be smaller. The effect of increasing the film thickness and bringing the mode farther away from cutoff is twofold. Firstly, the energy is more concentrated in the film and should therefore decay at a slower rate. From a ray picture, as a mode is brought away from cutoff, the angle the ray makes with the plane of the film becomes smaller and therefore the distance between successive reflections in the zig-zag ray path increases. This suggests that less energy is lost per unit length of film. Since the "optical tunneling" occurs through the coupling of the evanescent fields in the gap, the second effect of bringing the mode farther away from cutoff and thereby reducing the evanescent field, is to reduce the amount of energy coupled into the film. Intuitively, this seems reasonable since if the coupling between the prism and the film is reduced, less energy will tunnel into the film, but the energy that does get in should stay in longer. The second of these two opposing effects was observed to be dominant causing the streak to decrease in length with increasing film thickness as a result of the decreased coupling through the evanescent fields. The reason for the rapid decrease in the energy in the film, even after it is totally decoupled from the



(a)



(b)

Figure 6.3 (a) A 3 cm. streak in film due to coupling in of TM_0 mode.
(b) Streak stops abruptly where film has been scratched.

prism, must be due to scattering centers but particularly to surface defects which will transfer energy into the radiation and substrate modes. Indeed, when a very poor quality film, obtained as a result of poor substrate preparation, was used, a streak only a few mm. long was observed and a faint beam was noticed in the substrate which emerged at the end of the slide and illuminated the whole spectrum of substrate modes on a screen.

To demonstrate that this decrease in the length of the streak is in fact due to the mode being brought farther from cutoff and not due to a possible increase in film losses with thickness, more layers were deposited until the TE_0 mode was just at cutoff. This occurred around 140 layers. At this point the TM_0 streak was substantially reduced to about 1cm., however, the TE_0 streak was 2 cm. long which supports the previous argument. Fig. 6.3(b) gives visual proof that the energy is indeed guided in the thin film since the streak stops abruptly where the film has been scratched.

6.2.2 Experimental Technique for Mode Observation and Measurement

To facilitate the excitation of the waveguide modes and accurately measure their respective launching angles into the prism coupler, the instrumentation shown in Fig. 6.4 was set up. In addition, this figure shows some of the equipment used for the film manufacture. The measuring equipment consists of a He-Ne gas laser and polarizer mounted on a movable arm whose angular displacement can be directly measured on a scale to 1/100th of a degree. This allows the variation

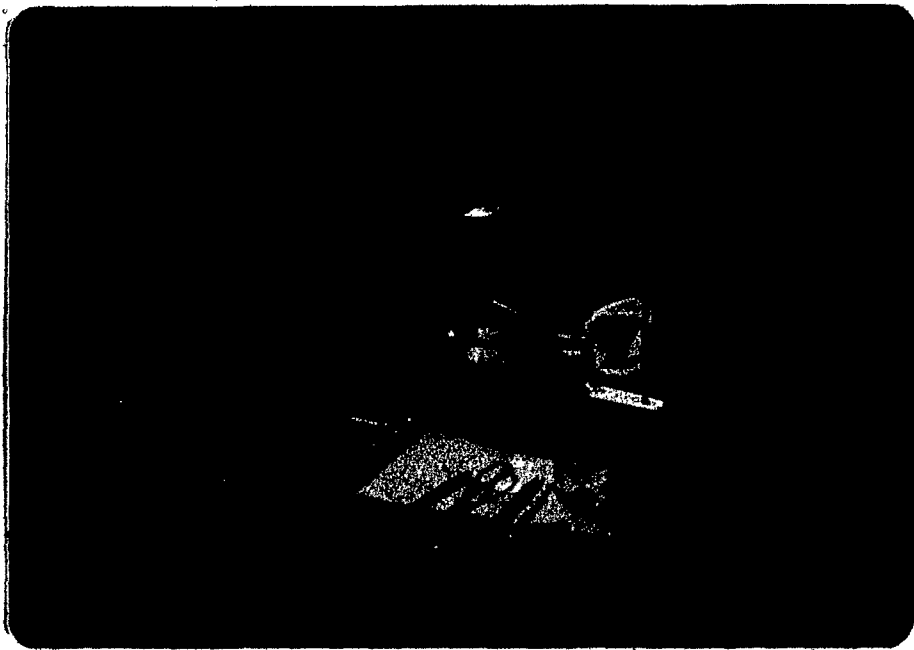


Figure 6.4 Mode excitation and measuring instrumentation along with some equipment used for the film manufacture.

of the angle of incidence at which the laser beam strikes the coupling point at the base of the prism. The prism-film coupler assembly is mounted on a micropositioner which in turn is fixed to a precision gimbal. These allow the fine adjustments necessary for accurate control of the beam position for mode excitation. This setup has also been used to make Brewster angle measurements for the refractive index determination of the prism and substrate. Details concerning the equipment calibration and alignment will be found in Appendix D.1.

The method used to measure the synchronous directions will now be described and reference will be made to Fig. 6.5. For drawing convenience, the film thickness has been greatly exaggerated. Once the thin-film waveguide and prism have been appropriately mounted with the correct pressure applied as was described earlier, the assembly is placed on the positioner which rests directly above the pivot of the movable arm. Its position is adjusted so that the prism face is nearly parallel to the displacement direction as shown in Fig. 6.5, and the coupling point is nearly above the pivot. It is necessary that the laser and gimbal have been previously aligned, as outlined in Appendix D.1, to avoid excessive positioner adjustment as the angle of the laser beam is varied. The laser height is then set so that the beam falls on the coupling point. Since a 60° prism was used, it was convenient to align the coupler assembly so that normal incidence on the prism face would occur with the laser at 30° . This can be readily performed by adjusting the gimbal movements until the reflected beam, which emerges from the opposite prism face and impinges on a screen, forms a cluster of spots

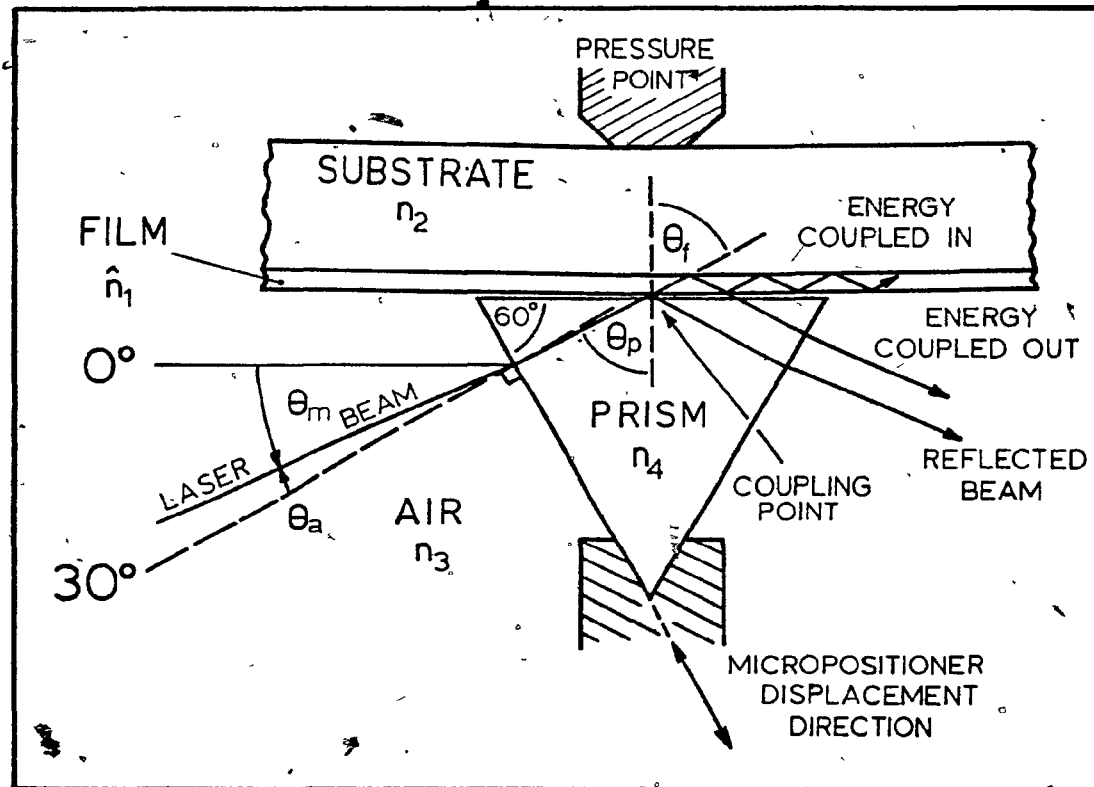


Figure 6.5 Mode angle determination with the prism-film coupler.

due to the multiple reflections between the laser and prism. By slight adjustment of the azimuth and elevation, the cluster should be distributed symmetrically about the main spot. Once this has been performed, the coupler alignment is complete and it is only necessary to vary the angle of the laser beam while, at the same time adjusting the micropositioners, to maintain the beam at the coupling point, until a mode has been excited. Referring again to Fig. 6.5, the angle of the laser beam θ_m is read directly from the scale at the end of the movable arm.

$$\text{Then : } \theta_a = 30^\circ - \theta_m \quad (6.1)$$

$$\theta_p = 60^\circ + \sin^{-1} \left[\frac{n_a \sin \theta_a}{n_p} \right] \quad (6.2)$$

where n_a and n_p are the indices of the air (n_3) and prism (n_4)

From equation (D.7) in Appendix D, the normalized propagation constant is given by :

$$\bar{\beta} = n_o \sin \theta_o = n_e \sin \theta_e = n_p \sin \theta_p \quad (6.3)$$

Here, n_o and n_e are the effective indices for the ordinary (TE) and extraordinary (TM) rays making angles θ_o and θ_e respectively with the normal to the film. Since the film is birefringent, having positive uniaxial anisotropy (34), and the molecular chains have been found to be perpendicular (36), the refractive index tensor has been assumed to be diagonal which still allows the separation of the waveguide modes into the TE and TM polarizations.

$$\hat{n}_1 = \begin{bmatrix} n_{1x} & 0 & 0 \\ 0 & n_{1y} & 0 \\ 0 & 0 & n_{1z} \end{bmatrix}$$

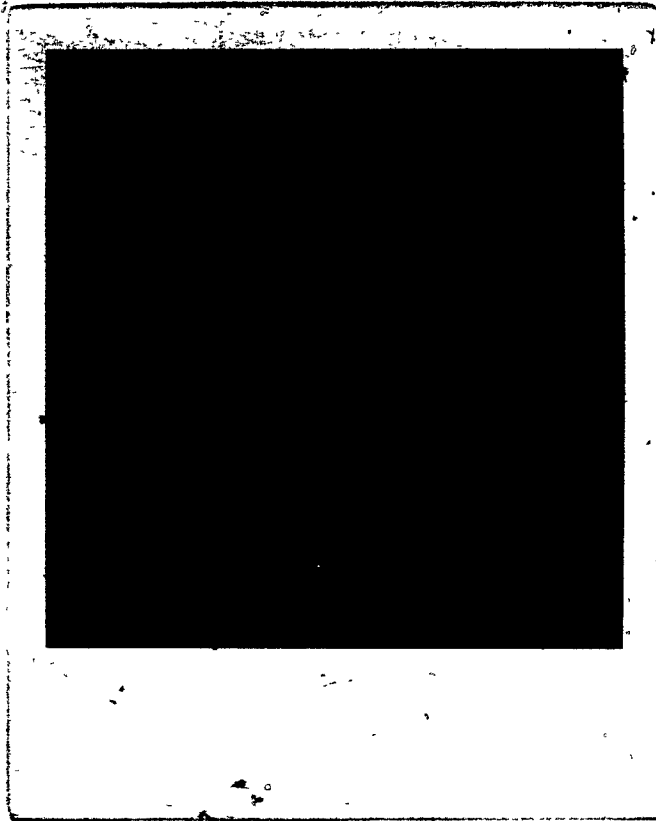
As the anisotropy is uniaxial, $n_{1y} = n_{1z}$, and its positive nature is a result of $n_{1x} > n_{1z}$. In Appendix D.2 it has been shown that :

$$n_o = n_{1y}$$

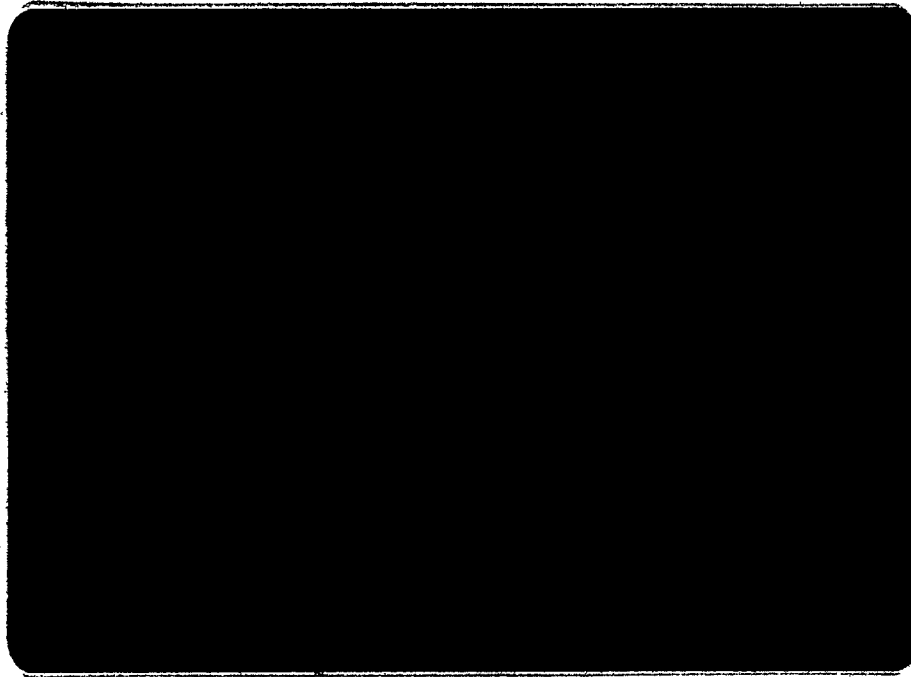
$$\left[\frac{1}{n_e} \right]^2 = \left[\frac{\cos \theta_e}{n_{1z}} \right]^2 + \left[\frac{\sin \theta_e}{n_{1x}} \right]^2$$

These results show that the TE waves are not affected by the film's anisotropy. The angle θ_f made by the rays in the film, is equal to either θ_o or θ_e depending on which type of mode is excited.

By setting the polarizer's axis of transmission parallel (or perpendicular) to the plane of incidence, the TM (or TE) modes will be excited. During mode excitation various phenomena take place which readily indicate this event. The first thing which is observed is the appearance on the screen of a bright vertical line passing through the bright spot formed by the reflected beam. This is shown in Fig. 6.6(a) where smoke has been used to render the laser beam visible. This line is slightly curved since the screen intersects a cone of rays whose vertex is at the coupling point. The cone represents the synchronous direction or allowed angle in 3 dimensions. A whole section of the cone is illuminated rather than just a line because of scattering in the film and because the beam is not perfectly collimated. Another observation is the occurrence of the streak which represents the energy coupled into and carried by the film. The bright spot due to the reflected beam, also decreases somewhat in intensity during mode excitation. By careful observation, a dark vertical line can be seen in this spot. This is



(a)



(b)

Figure 6.6 (a) Excitation of the TM_0 mode.
(b) Excitation of a substrate mode.

again due to the fact that the beam is not perfectly collimated and only those rays at the correct angle will be coupled in. This indicates that the linewidth of the mode is very narrow, which is important if this method is to be used for accurate measurements. The synchronous directions are most sharply defined at weak coupling, when the compression at the coupling point reduces the gap width just enough to barely excite the mode. A final observation is the increased brightness of the film in the area around the coupling point. The illuminated area directly in front of the slide is due to the light scattered into the substrate. If the thin-film waveguide can support several modes, the excitation of one will cause the others to be excited to a lesser extent due to scattering. The modes which are closer to the main mode and are of the same polarization are excited to a greater extent. The substrate modes are easily excited by increasing the laser beam angle beyond cutoff. Fig. 6.6 (b) shows the light beam in the substrate bouncing back and forth between the slide surfaces. These modes form a continuum as the slide is many thousands of wavelengths thick so that there is no observable discreteness in the allowed angles. Ray theory will readily describe the situation here.

As far as optical signal processing is concerned, it is necessary to couple the beam in at one point and let it propagate in the film through some thin-film device such as an electrooptical modulator where signal information can be impressed on the light beam as intensity modulation. The beam can then be coupled out with another prism after the device. By using the arrangement depicted in Fig. 6.7(a) where two

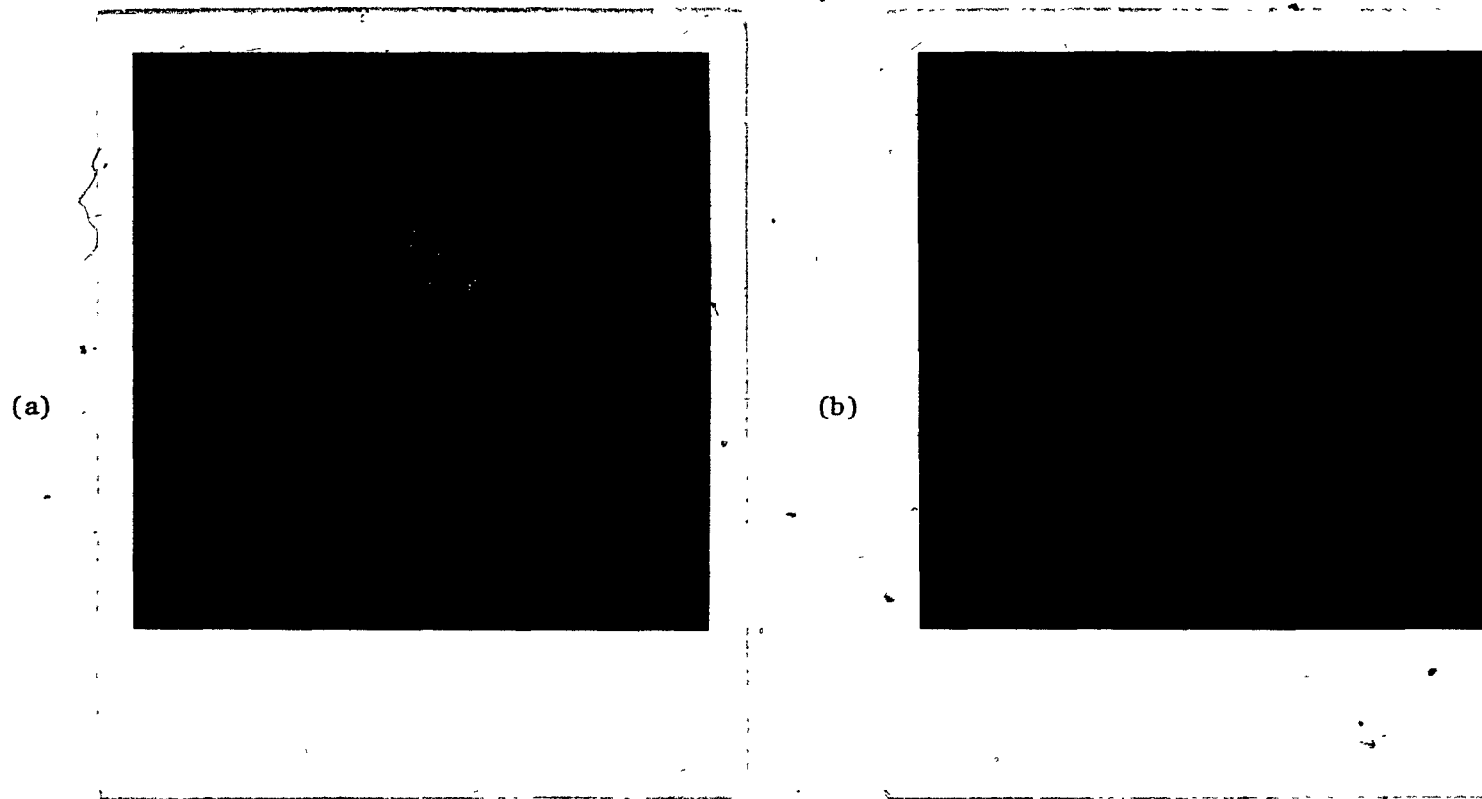
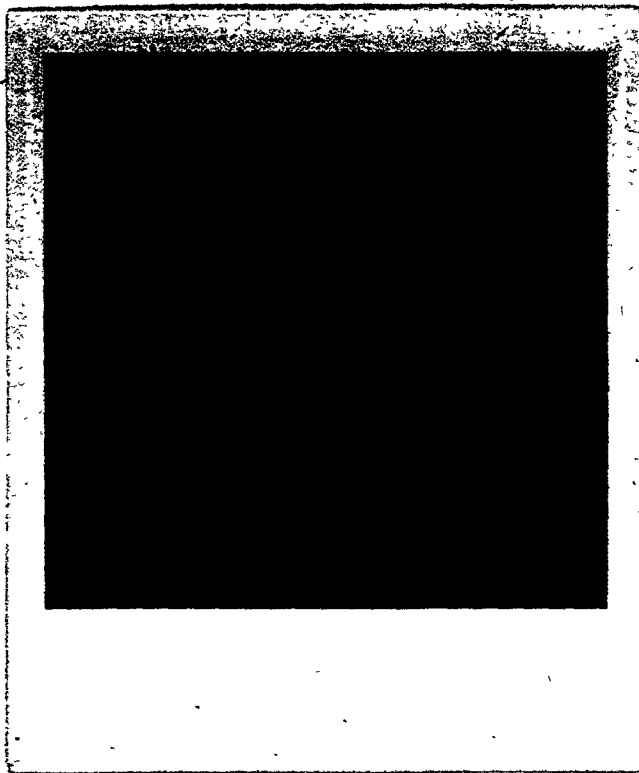


Figure 6.7 (a) Prism-film coupler assembly with 2 pressure points to couple the light in and out of the film.
(b) TM_0 mode coupled in and out after a $1\frac{1}{4}$ cm. guidance in the film.

pressure points are applied $1\frac{1}{4}$ cm. apart, it was possible to couple in some of the light at the right pressure point, and after a short distance couple all the light out at the left pressure point. This has been displayed in Fig. 6.7(b). Notice that the streak terminates at the left pressure point as all the energy is coupled out. The faint beam and spot below the main reflected beam dramatically show the energy being coupled out. Fig. 6.8(a) is a close-up of the streak between the two pressure points while Fig. 6.8(b) shows the TM_0 mode. The line at the right represents the energy coupled out immediately along with the bright spot of the reflected beam, while the left line is totally due to the energy which has travelled along $1\frac{1}{4}$ cm. of film before the gap becomes small enough to allow the light to tunnel back into the prism. The interference fringes due to the two pressure points look like equipotential lines about two like charges in close proximity. This implies that the gap increases only gradually between the two points which is the reason for the large amount of energy coupled out immediately from the right point. Since two right angle prism cannot be used due to the soft nature of the film, an abrupt increase in the gap could be obtained by making a tiny groove in the base of the prism along the beam path between the coupling points. This would certainly increase the energy carried in the film.

With the deposition of more and more layers on the slide, the film thickness was slowly increased. By exciting and measuring the mode angles at various stages in the thickness, the dispersion curves were obtained. These will be examined in detail in the next section. In Fig. 6.9(a), the TE_0 mode has been excited with 173 layers in the film. The

(a)



(b)

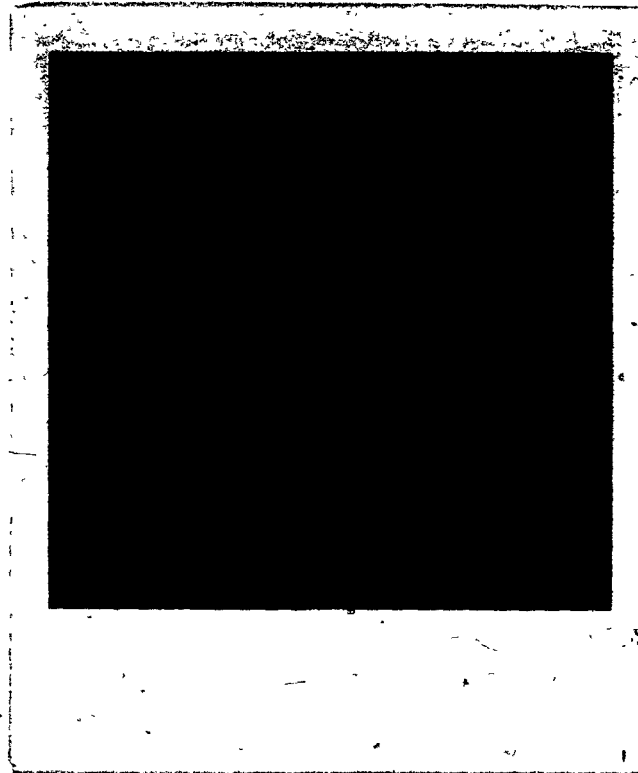


Figure 6.8 (a) Streak stops at the second pressure point since all the energy is coupled out.
(b) TM_0 mode coupled out immediately (right) and after a $1\frac{1}{4}$ cm. travel in the film (left).

TM_0 mode is barely visible at its left. When the thickness was increased to 361 layers, the TM_1 mode was excited and is shown in Fig. 6.9(b). In this picture, a hole was made in the screen through which the reflected beam was made to pass. This allowed a better definition of the other modes. Notice that the TM_0 mode is brighter than the TE_0 mode which lies between the two TM modes. By the time 541 layers had been deposited, four modes could be excited as shown in Fig. 6.9(c). From right to left they are : TE_1 , TE_0 , TM_1 ; TM_0 . Notice that the TM_1 and TE_0 modes have crossed each other. To make the TM modes more visible, the polarizer was removed. Finally, after 601 layers, 5 modes were allowed. In Fig. 6.9(d) the right-most mode is TM_2 while the rest are unchanged from the previous case.

6.3 Matching of the Experimental and Theoretical Propagation Characteristics to Determine the Film's Birefringence and Thickness

The multilayer film which has been used to coat the substrate has positive, uniaxial anisotropy with an optical axis perpendicular to the film surface. Under this condition, the refractive index tensor of the film n_1 is diagonal and the TE and TM modes are separable. The anisotropic theory yielding the dispersion relations will be found in Appendix D.2. An indication of the film's anisotropy was given by the behaviour of the modes discussed in the previous section, since in an isotropic film the modes do not cross and the TE and TM modes follow each other in succession. The more general case of arbitrary anisotropy

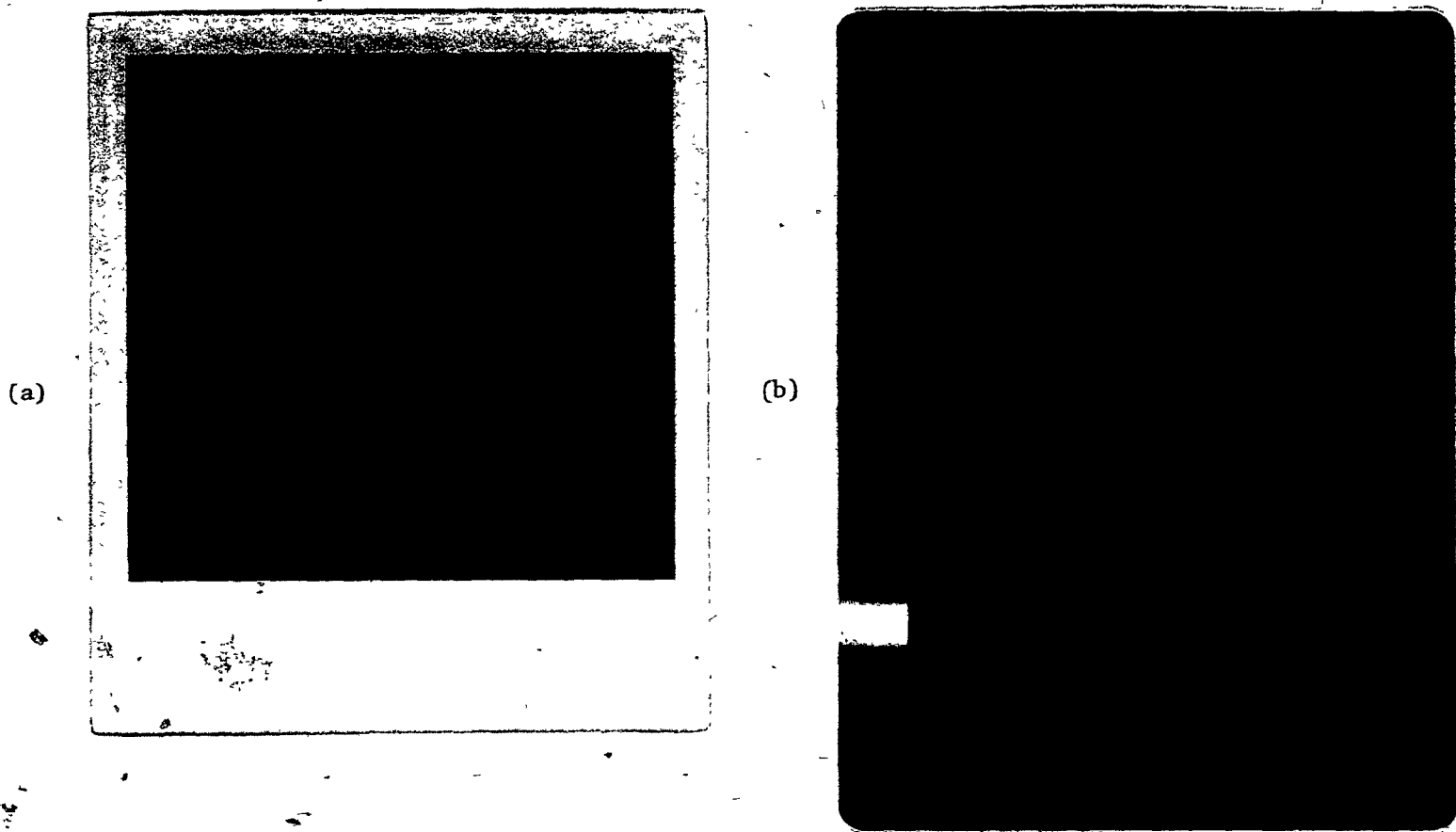


Figure 6.9 (a) Excitation of TE_0 mode (right) and scattered energy into TM_0 mode (left).
(b) Excitation of TM_1 mode (right) and scattered energy into TE_0 mode (middle) and TM_0 mode (left).

(c)



(d)

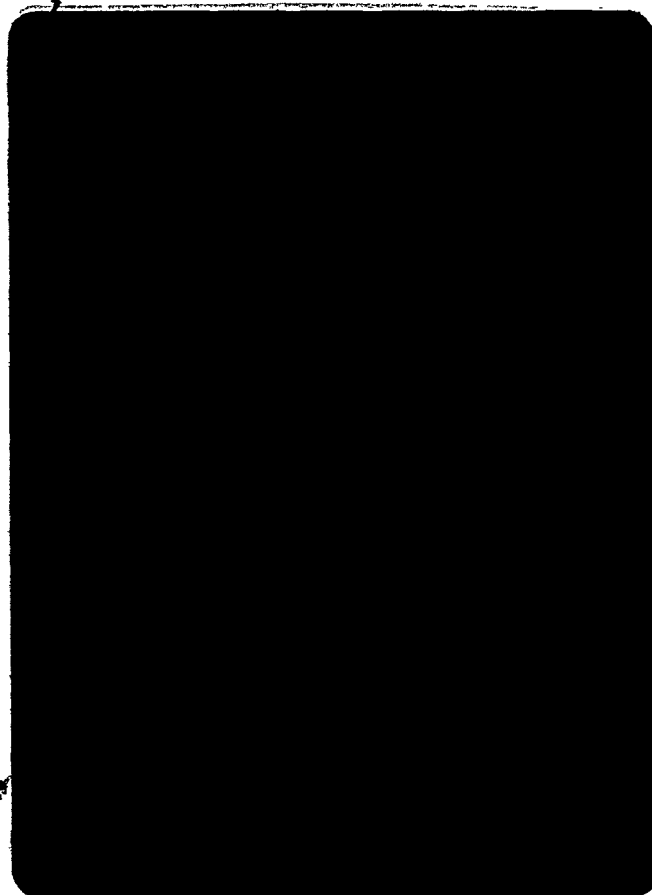


Figure 6.9 (c) Excitation of TE_1 mode (right) and scattered energy into TE_0 , TM_1 , TM_0 modes (right to left).
(d) Excitation of TM_2 mode (right) and scattered energy into TE_1 , TE_0 , TM_1 , TM_0 modes (right to left).

(58) would result in hybrid modes and greatly complicate the analysis. This has been found to be unnecessary as the experimental results fit quite well with the theory.

For the TE modes, the dispersion relation given by equation (D.4) can be just written as :

$$(k_0 d)_i = F_i(\bar{\beta}_i, n_{ly}) \quad (6.4)$$

This simply means that for the i th mode, the thickness d is a function of the unknown n_{ly} and $\bar{\beta}_i$, which can be related to the allowed angle through equations (6.1) to (6.3). This angle can be measured fairly accurately, however, the thickness is not known precisely since film compression and irregularities can cause a substantial difference between the actual thickness and that theoretically predicted from a knowledge of the number of layers. By treating $(k_0 d)_i$ also as an unknown, at least two TE modes are required to solve (6.4). In general, for a particular film thickness, $\bar{\beta}_i$ $i = 1, \dots, N$ can be experimentally determined where N is the number of TE modes observed. Since $(k_0 d)_i$ must be the same for all these modes as long as the pressure and coupling position is not adjusted during the entire measurement, the unknown n_{ly} can be determined by minimizing the average difference G between every two $(k_0 d)_i$ given by :

$$G = \frac{2}{N(N-1)} \sum_{i=1}^{N-1} \sum_{j=i+1}^N |F_i - F_j| \quad (6.5)$$

In this way, the value for n_{1y} can be determined for various thicknesses and the results averaged. For the TM modes, the dispersion relation given by equation (D.6) can also be written as :

$$(k_0 d)_i = F_i(\bar{\beta}_i, n_{1x}, n_{1z}) \quad (6.6)$$

Since the film is uniaxial, the previously obtained value for n_{1y} can be substituted for n_{1z} and the same minimization method used to evaluate n_{1x} . This yields the optimum diagonal index tensor for the given experimental data. In addition, for each thickness at which the modes have been measured, an optimum value of $k_0 d$ is obtained. If an account of the number of layers is kept, an estimate for the monolayer thickness can be obtained. Then by averaging out all these estimates, an optimum monolayer thickness value will be found.

A computer program has been formulated to carry out the minimization and averaging of many sets of data. First the TE data is inserted to obtain an average value for n_{1y} . Then by inserting this value along with the TM data, n_{1x} is found. A program flow chart will be found in Appendix D.3 along with some further explanations. The data and results are listed in Table 6.1. The accuracies associated with the average values of index and thickness are their standard deviations.

Once the refractive index tensor has been obtained, the dispersion curves can readily be generated with the aid of a simple program which is also described in Appendix D.3. These curves are displayed in Fig. 6.10 where $\bar{\beta}$ has been plotted against the normalized frequency $k_0 d$ which has also conveniently been related to the number of monolayers at

Table 6.1 : Data and Results for Index and Thickness

EXPERIMENTAL DATA					COMPUTED RESULTS				
NO. OF LAYERS	MODE TYPE	$\bar{\beta}$			n_{ly}	n_{lx}	AVERAGE k_{od}	ϵ	MONOLAYER THICKNESS (A)
		0	1	2					
359	TM	1.5277	1.4596			1.5546	9.041	0.003	25.36
361	TM	1.5248	1.4587			1.5513	9.090	0.006	25.36
395	TM	1.5319	1.4679			1.5556	9.803	0.006	25.00
421	TM	1.5318	1.4719			1.5536	10.295	0.000	24.63
427	TM	1.5354	1.4760			1.5568	10.480	0.004	24.72
461	TM	1.5375	1.4852			1.5559	11.467	0.003	25.05
	TE	1.4885	1.4572		1.5013		12.273	0.005	26.81
481	TM	1.5367	1.4865			1.5543	11.759	0.004	24.62
	TE	1.4885	1.4579		1.5005		12.747	0.004	26.69
493	TM	1.5391	1.4922			1.5554	12.323	0.010	25.17
	TE	1.4899	1.4582		1.5023		12.569	0.006	25.68
527	TM	1.5419	1.4973			1.5573	12.780	0.003	24.42
	TE	1.4906	1.4595		1.5024		12.967	0.007	24.78
541	TM	1.5395	1.4972			1.5540	13.157	0.012	24.49
	TE	1.4906	1.4601		1.5021		13.192	0.004	24.56
559	TM	1.5430	1.5029			1.5567	13.655	0.001	24.60
	TE	1.4920	1.4625		1.5028		13.727	0.009	24.73
593	TM	1.5438	1.5084	1.4591		1.5554	14.910	0.136	25.32
	TE	1.4922	1.4653		1.5018		14.755	0.015	25.06
601	TM	1.5413	1.5058	1.4584		1.5528	14.940	0.222	25.04
	TE	1.4923	1.4647		1.5023		14.463	0.015	24.24

Average values for barium stearate multilayers :

$$n_{lx} = 1.5549 \pm 0.0017, \quad n_{ly} = 1.5019 \pm 0.0007$$

$$\text{Layer thickness} = 25.06 \pm 0.67 \text{ \AA}$$

$$k_{od} = (0.02486 \pm 0.00066) \times (\text{No. of Layers})$$

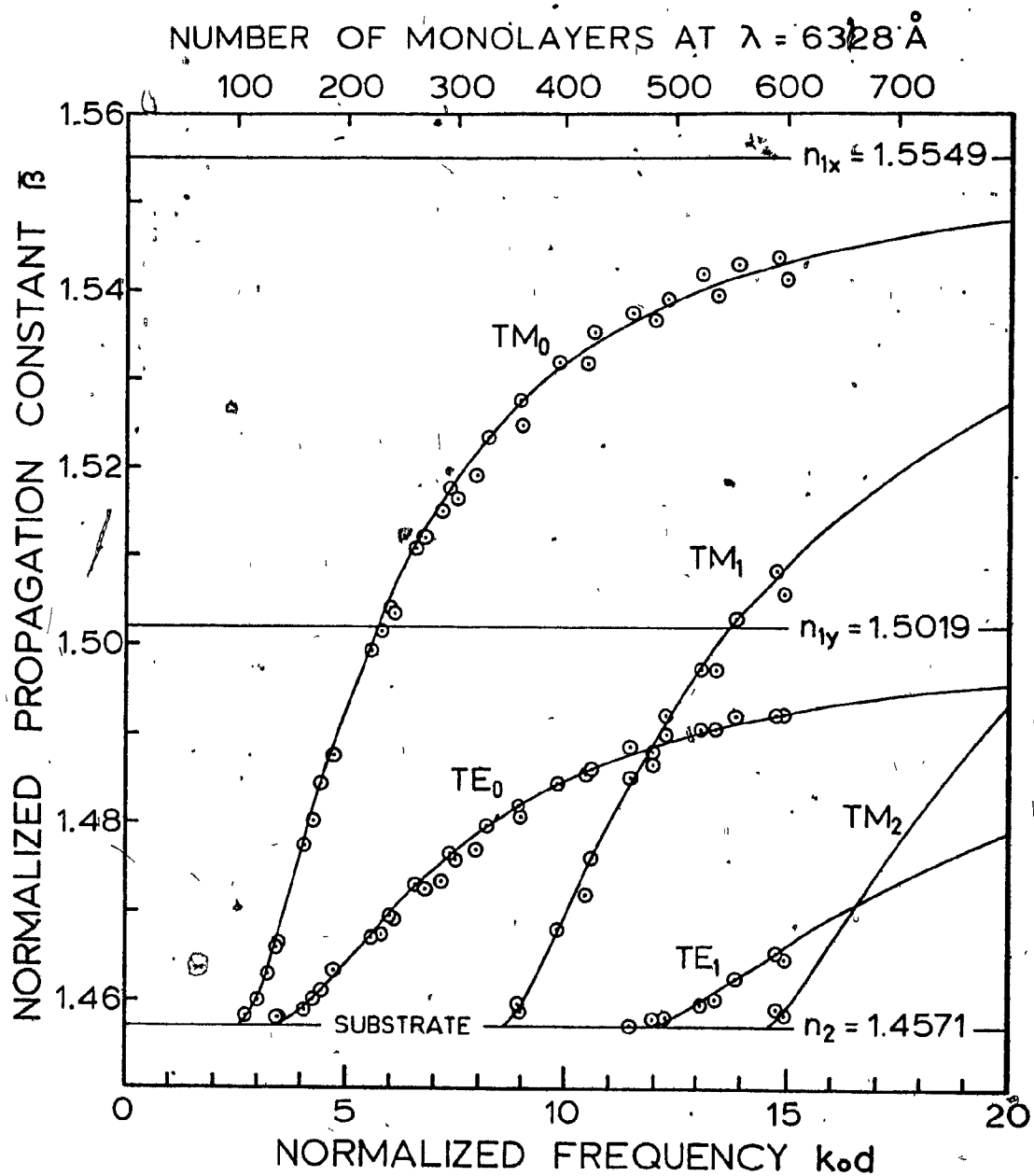


Figure 6.10 Comparison of the theoretical dispersion curves with the experimental data for the anisotropic thin-film waveguide.

the He-Ne laser frequency of 6328 Å. To do this, the previously determined average layer thickness of 25.1 Å has been used. It is interesting to note the behaviour of the TE and TM modes. The latter tend asymptotically to the higher index value n_{1x} while the TE modes tend to n_{1y} (or n_{1z}). This is quite reasonable as the TE modes represent polarization in the plane of the film where the index is really isotropic. On the other hand, the TM or extraordinary rays have an effective index n_e given by (D.9) which is a function of θ_e , the angle the ray makes with the film normal. As β increases, this angle approaches 90° and $n_e \rightarrow n_{1x}$.

The experimental data points have been superimposed on these curves and show a relatively good agreement with them. To plot these points, the value of k_0d used was that given from a knowledge of the number of layers and the computed average layer thickness. As was pointed out previously, this can be somewhat in error due to compression and irregularities in the film, and a better fit would have been obtained if the optimum values of k_0d resulting from the data fitting would have been used. This was not done, however, as it would not correctly represent the experimental data especially since the theory does not exactly describe the waveguide as it is far from being ideal.

Another cause of error, and the reason why so many data points had to be used, was the difficulty of making accurate angle measurements. Although the angles could be measured precisely to 1/100 th of a degree, the angle at which the mode was excited was not as sharply defined. This was due to several factors like the slight divergence in the laser beam, irregularities in the film, overcompression at the coupling point which

caused the mode line to broaden, and the fact that the peak of the mode excitation had to be determined visually since the observation most sensitive to angular movement is the dark line in the bright spot representing the energy coupled into the film. For each data point, the average of 3 to 6 angle measurements was taken depending on the spread of the data. Among the more inaccurate measurements, a typical spread of ± 0.025 in angle was obtained. This represents a spread of about ± 0.0002 in the value of β , which is only a slight variation on the scale used in the graph.

By comparing with the accuracy obtained by Tien (32) who readily detected changes in index of 0.1% and 1% in the film thickness; it can be stated that the results obtained here are indeed quite good since deviations in the index values are also in the 0.1% range while the thickness value has an accuracy of about 2%. It must be taken into consideration, however, that Tien's organosilicon films are of high optical quality and accurate measurements of the prism and substrate indices were made with an Abbé refractometer. The Brewster angle method was used to determine the prism's index although it is not very accurate as the intensity minimum is not sharply defined. A high quality polarizer would facilitate this task. By averaging 20 readings, a value of 1.7252 ± 0.0021 was obtained. The substrate, however, was made of fused quartz since its index had to be as low as possible from waveguide considerations. The lower the index, the fewer would be the required number of layers needed to excite a given number of modes. The refractive index of fused quartz at the He-Ne laser frequency was readily found to be

1.4571 by interpolation between tabulated values at specific frequencies (59).

In Table 6.2 the computed monolayer indices and thickness are compared with values determined by others. The values which have been obtained lie within the range of those determined by others. This reinforces the validity of the current method and suggests that it is at least comparable in accuracy to the other techniques.

Table 6.2 : Optical Constants of Ba-Cu-H-St Films

REFERENCE	n_{1x}	n_{1y}	LAYER THICKNESS (Å)	METHOD
Blodgett et al (34)	1.551±0.002	1.491	24.4	Interferometry
Bateman et al (41)	1.560	1.510	24.7 ±1.3	Mattuck
Srivastava et al (36)	—	—	25.3 ±0.4	X-ray
Srivastava et al (36)	—	—	26.2 ±0.3	Interferometry
This Work	1.555±0.002	1.502±0.001	25.1 ±0.7	Waveguide Theory

CHAPTER 7CONCLUSIONS AND DISCUSSION ON FURTHER WORK

The present work has demonstrated the feasibility of using Ba-Cu-H-St monolayers deposited on a fused quartz substrate, as a thin-film waveguide. A manufacturing process has been set up which employs the Blodgett-Langmuir molecular film technique to deposit single molecular layers on a substrate, allowing tremendous control on the thickness of the film. Although some major problems associated with the film manufacture need to be overcome if high quality, low-loss films are to be obtained, it has been shown that the film will support guided modes, and that these modes agree reasonably well with those theoretically determined. Indeed, the results show that the film is composed of positive uniaxial crystals whose optical axis is perpendicular to the plane of the film resulting in a diagonal permittivity tensor. Films up to 600 layers thick have been deposited and the modes at many intermediate thicknesses have been observed and measured through the establishment of an accurate measuring technique. By correlating these measurements with the anisotropic waveguide theory, it has been found that the refractive indices for the ordinary and extraordinary rays are 1.502 and 1.555 respectively, and that the monolayer thickness is 25.1 Å. These results are within the range of those obtained by others who have used various methods to compute the optical constants of these multilayers.

Several improvements can be made on the present fabrication system so as to both facilitate the deposition process, but more importantly,

to improve the film quality. The first and it is felt the most important modification would be to eliminate the use of oil to create the required surface pressure since it necessitates a very tedious cleaning process between the spreading of successive films, and even with this process, substantial oil contamination is still introduced. This should be replaced by some sort of mechanical drive to push a barrier acting as a surface piston. The proper pressure could be maintained by using a feedback system which employs a film balance to monitor the surface pressure and some control circuitry to relate this information back to the mechanical drive. Other workers (40), (43) have reported the use of a set of weights and pulleys to exert a constant pressure on a movable barrier. The pressure, which was measured with a film balance, was adjusted by varying the weights. One method (42) employs two solenoids on either side of the tray to exert a constant force on the movable barrier which is directly proportional to the applied current. However, the barrier movement is restricted to a 2 inch range and requires constant supervision and manual adjustment.

Another aspect of the system which could be looked into is the automatic dipping device since its dipping speed is not constant but rather sinusoidal and therefore requires more time than necessary to deposit each layer. One consideration might be to replace the entire mechanism by a pneumatic system where an air cylinder is used to produce a constant reciprocal dipping motion and whose speed can be controlled by regulating the air pressure. To minimize contamination, the whole process should be enclosed in a dust-free chamber wherein the substrate

cleaning and film deposition would be carried out continuously under "sterile" conditions. This would require an automatic system to handle and transport the slide from one operation to the next and a means of automatically cleaning the subphase surface and spreading new films. Vibrations could also be minimized by mounting the system on a vibration-free table, the level of which must remain constant for obvious reasons.

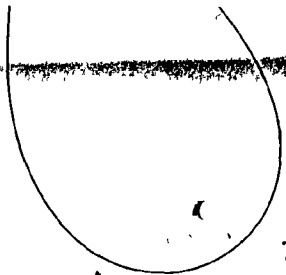
Despite the above suggestions however, the quality of the resulting thin-film waveguide will ultimately depend on how well the chemistry of the deposition process is understood and to what extent the various parameters which affect it can be controlled. This requires a good technical support from the experts in this field who are still studying and developing this science and are examining many types of film-forming compounds. Indeed, from practical considerations, these fatty acid soap films have the disadvantage of being soft and therefore easily deformed and damaged. Other compounds might offer more appealing mechanical properties in addition to a well-ordered crystal structure and supply a technological boost to the presently just developing integrated optics field.

Nevertheless, the present system offers the possibility of making single and multimode waveguides of satisfactory optical quality to allow further investigations into the film's properties and possible uses in non-linear optics like optical second harmonic generation (5), (27). Due to its marked anisotropy, the film's electrooptical properties should be tested and its feasibility as an optical modulator be determined.

A great deal of work has already been carried out (37) on the

determination of the electrical properties of this film. In particular, the dielectric properties of these multilayers were investigated. The dielectric constant and capacity as a function of frequency, have been studied. The maximum dc dielectric strength of barium stearate films was determined to be in the vicinity of 10^7 V/cm. while the ac strength varied from 2×10^5 to 10^6 V/cm. as the frequency was increased from 1 to 300 kHz. .

Electrooptical modulation (60), (61) of the light intensity is usually achieved through the application of an electric field across a birefringent crystal. By varying the field strength, the index difference between the crystal's slow and fast axes is changed resulting in a variation in the polarization of the emerging light. If an analyser is then used, this variation is transformed into intensity modulation. It should be possible to use this modulation scheme in the anisotropic multilayer waveguide by adjusting its thickness to the point where the TE_0 and TM_1 modes cross. This occurs when $k_0d \approx 11.95$ or at around 480 layers. Both the ordinary and extraordinary rays will then travel along the film as shown in Fig. D.2. Upon being coupled out, they will have a relative phase shift which is dependent on their respective path lengths, indices, and reflection phase changes. If an electric field is somehow applied across the film's thickness, it should be possible to vary n_{1x} and consequently change the optical path length of the extraordinary ray while leaving the ordinary ray unaffected. In this way, the polarization of the emerging beam could be changed and intensity modulation achieved with very low voltage applied due to the thinness of the film.

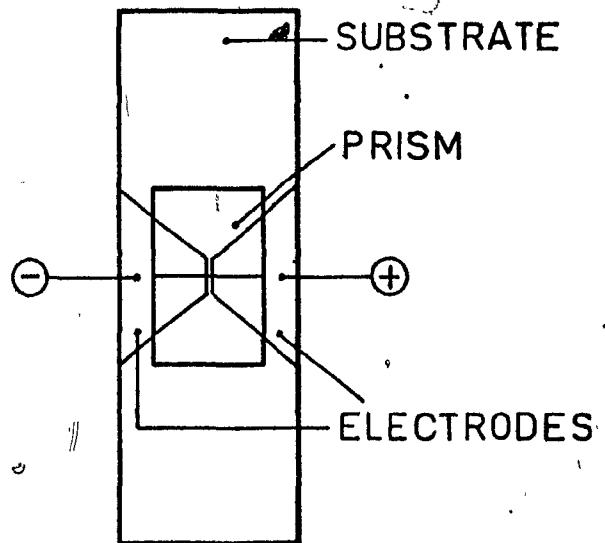


Another modulation technique that could be attempted is modulation of the synchronous direction. In this method, an electric field is again used to vary the index, but this time, the resulting change in the allowed ray angle is of interest. The birefringence property of the film is not used in this case. Due to the laser beam's divergence, it was found that only those rays very close to the synchronous direction were coupled into the film. This was indicated by the dark vertical line on the reflected spot. By applying a field across the plane of the film, n_{1y} should be varied slightly which in turn would result in a shift of the dark line of the TE modes.

The application of the field is not as difficult as in the previous case and a method has been illustrated in Fig. 7-1. The electrodes are thermally evaporated on a clean quartz slide. If gold is used, the surface will be hydrophilic while aluminum or silver will make it hydrophobic (37), (43). These electrodes should be as thin as possible so that the gap between the film and prism will not be too large. If the electrodes have a separation of say 50μ , a maximum of 500 volts can be applied if a 10^5 V/cm. ac rating is not to be exceeded. A deflection of the dark vertical line should be observed with a much lower field strength if the film is to be useful. Intensity modulation can then be realized by placing an aperture over the dark line so that when no voltage is applied the transmitted light is a minimum and increases with increasing voltage due to the shift of the dark line.

These suggestions have been given so as to furnish some incentive in the hope that further work be carried out as it is felt that this film does have the potential for very practical applications in thin-film devices.

TOP VIEW



EDGE VIEW

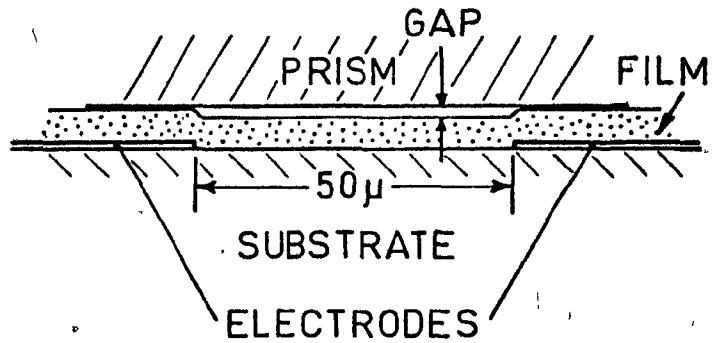


Figure 7.1 Thin-film electrooptical modulator.

APPENDIX ADESCRIPTION OF COMPUTER PROGRAMS UNDER THE STEP APPROXIMATIONA.1 Computation of the Dispersion Curves

A generalized flow chart of the program used to compute and plot the dispersion curves for a finite cladding slab waveguide having a parabolic index distribution in the core which is approximated by N homogeneous steps, is shown in Fig. A.1. This program was written to be as general and flexible as possible. The number of steps used to approximate the core has been specifically left variable, N being read in with the rest of the data. This requires the program to generate an arbitrary size matrix of $(2N+1) \times (2N+1)$ and take its determinant. The first of these tasks is performed by the subroutine MATRIX while the determinant is evaluated by the function subprogram DET which is most efficient, taking into account the existing zeros and using gaussian elimination. TE and TM, even and odd modes can be computed by merely changing a few appropriately labelled cards in the program.

Once the data is read in, the program proceeds to compute the normalized position (x_1/d) and refractive index (n_1) of each step. Then, starting at $\bar{\beta} = n_2 + 0.0001$ (since at $\bar{\beta} = n_1$, $K = 0$ making the matrix singular), the roots are obtained with subroutine ROOT by using :

$$k_{0d} = m\pi / \{x_1 (n_1^2 - n_2^2)^{1/2}\}, \quad m = 1, 2, 3, \dots$$

as a first approximation. ROOT employs the "interval-halving method" to systematically search for a root. For the next value of $\bar{\beta}$, the first root of the last search is used as an approximation to the first root of the present search. If $\bar{\beta}$ has

just been incremented, this approximation will lie to the left of the actual root, while if $\bar{\beta}$ has been decremented, it will lie to the right. Taking note of the sign of the determinant, which changes value between the roots, the uncertainty as to whether the approximations to the rest of the roots lie to their left or right is removed. This uncertainty is introduced since the WKB approximation was used to establish the approximate root positions as it gave very close estimates. For even modes, the approximation to the n th root is just $(1+2N)$ times the value of the first even root, while for odd modes it is $(1+2N)/3$ times the value of the first odd root.

By incrementing and decrementing $\bar{\beta}$, above and below its starting value in steps of $DB1$, the core modes are computed. When $\bar{\beta}$ is near n_1 , k_{0d} is very large for high order modes and overflow problems might result due to the blow up of the exponential terms in the last row of the matrix.

For the cladding modes, the WKB approximation cannot be used due to the sharp difference in the cladding modes. Here again, the first root is approximated by the one obtained in the previous search and then subsequent roots are approximated by adding to the last root the interval between the previous two roots. By successively decrementing $\bar{\beta}$ by $DB2$, the cladding modes are computed.

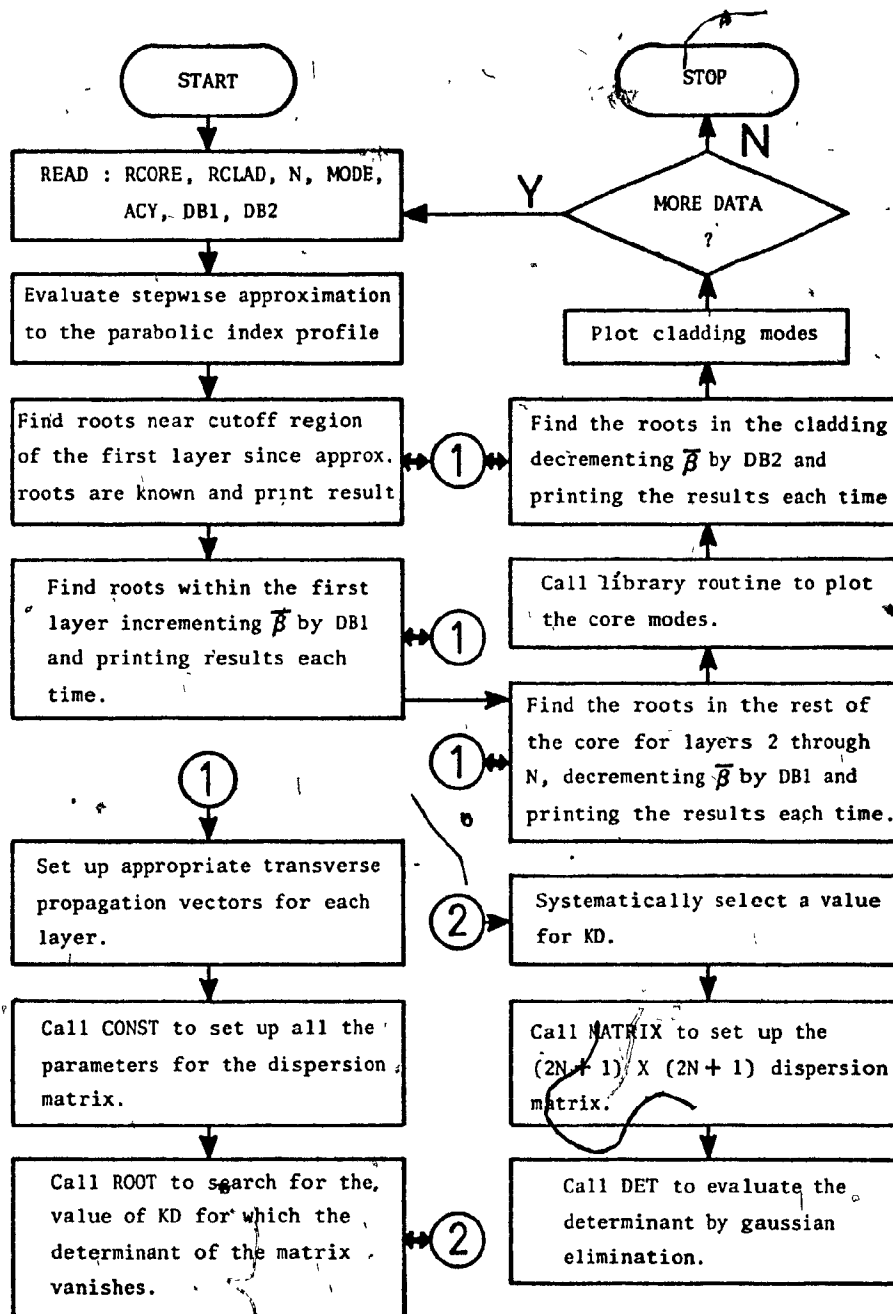


Figure A.1 Generalized flow chart for the dispersion curves program

A.2 Computation of the E and H Fields

Fig. A.2 describes the program used to compute and plot the E and H fields for a finite cladding slab waveguide having a parabolic index distribution in the core which is approximated by N homogeneous steps.

Definition of Labels :

B	- $\bar{\beta}$
KD	- $k_0 d$
RCORE	- n_a
RCLAD	- n_c
RATIO	- r
N	- N, number of steps used to approximate the core.
MODE	- number of modes to be computed.
ACY	- accuracy to which roots are determined.
DB1 , DB2	- increments in $\bar{\beta}$ used in the computation of the dispersion curves for the (1) core and (2) cladding modes.
NUM	- number of field points to be computed within each layer.
ME	- character data specifying 'TE' or 'TM' modes.
OE	- character data specifying 'EVEN' or 'ODD' modes.

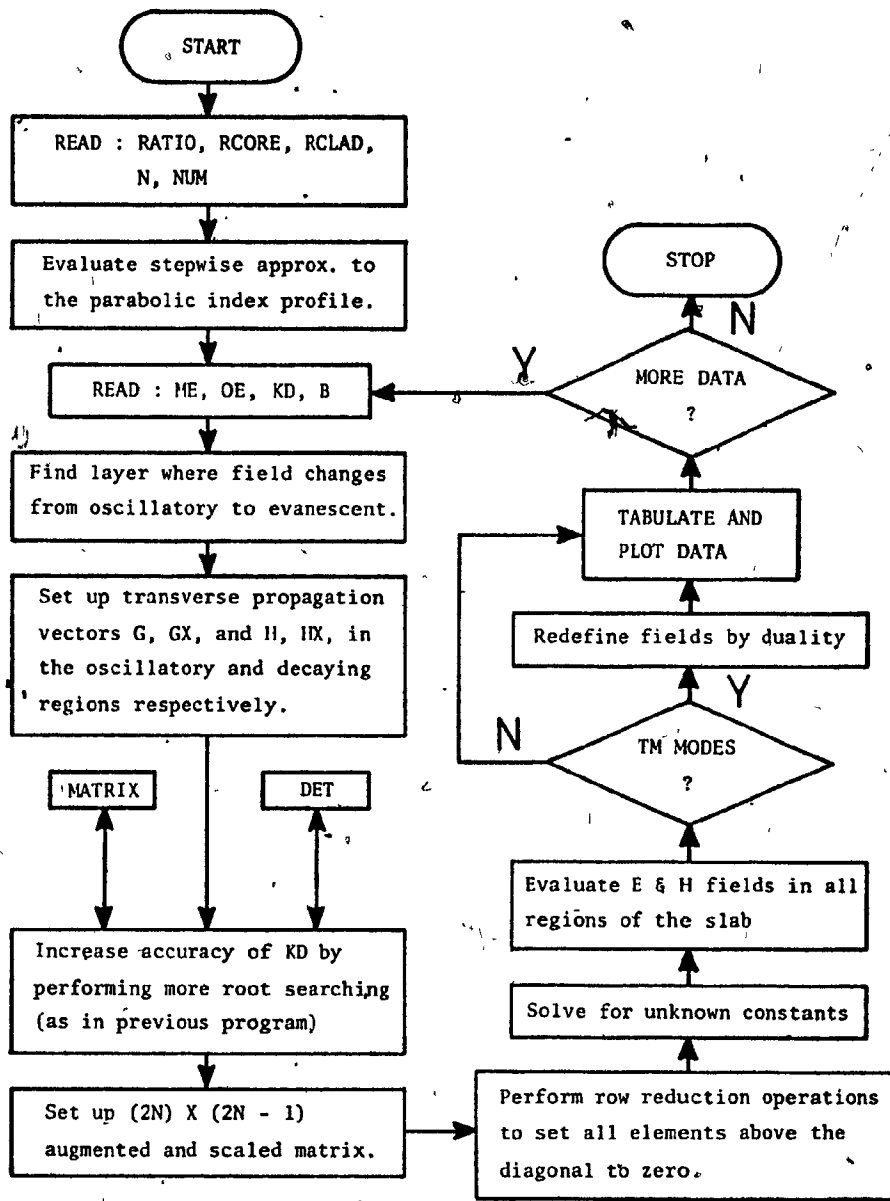


Figure A.2 Generalized flow chart for the fields program

APPENDIX BMATERIAL CONCERNING THE WKB METHODB.1 Nature of the WKB Approximation

A solution is sought for :

$$\frac{\partial^2 E_y}{\partial x^2} + K^2(x) E_y = 0 \quad (\text{B.1})$$

Let the solution be of the form :

$$E_y = F(x) e^{jS(x)} \quad (\text{B.2})$$

where $F(x)$ and $S(x)$ are real functions of x . Substitution into (B.1)

leads to :

$$\{F'' - F(S')^2 + K^2F\} + j\{2F'S' + FS''\} = 0$$

Since F and S are real functions, it follows that :

$$F'' - F(S')^2 + K^2F = 0 \quad (\text{B.3})$$

$$2F'S' + FS'' = 0 \quad (\text{B.4})$$

Multiplying (B.4) by F leads to :

$$(F^2S')' = 0$$

so that $F = C(S')^{-\frac{1}{2}}$, where C is a constant. If K varies slowly over one wavelength, it will be shown that F'' can be omitted in (B.3). With this approximation :

$$S' = \pm K \text{ or } S = \pm \int K(x) dx$$

Therefore from (B.2) :

$$E_y = CK^{-\frac{1}{2}} \exp\{\pm j \int K(x) dx\} \quad (\text{B.5})$$

Rewriting (B.3) as :

$$\frac{F''}{F} = (S')^2 - K^2$$

F'' can be omitted in (B.3) and the approximation is valid if :

$$|(S')^2 - K^2| = \left| \frac{F''}{F} \right| \ll (S')^2 \quad (\text{B.6})$$

or if $S' = \pm K$ as before. Since (B.4) yields $F = C(S')^{-2}$, substituting this into (B.6) gives :

$$\left| \frac{F''}{F} \right| = \left| \frac{3}{4} \left(\frac{S''}{S'} \right)^2 - \frac{1}{2} \frac{S'''}{S'} \right| \ll (S')^2$$

This inequality will be satisfied if it is satisfied by each term alone :

$$\frac{3}{4} (S'')^2 \ll (S')^4 \quad \text{and} \quad \frac{1}{2} |S'''| \ll |(S')^3|$$

If the first relation is satisfied, so is the second since it can be obtained from the first to within a constant factor by differentiation.

By substituting $S' = K$, the necessary condition is :

$$|K'| \ll K^2 \quad \text{or} \quad \left| \frac{dK}{K} \right| \ll 2\pi \frac{dx}{\lambda_x} \quad (\text{B.7})$$

which means that the fractional change in K over an incremental distance dx , must be much less than that distance normalized relative to λ_x , the transverse wavelength.

B.2 The TM Case

The reduced wave equation for the TM modes is of the form :

$$H'' + p(x) H' + q(x) H = 0 \quad (\text{B.8})$$

$$\text{where } p(x) = -\frac{1}{\epsilon(x)} \frac{d\epsilon(x)}{dx}, \quad q(x) = \frac{\epsilon(x)}{\epsilon_0} k_0^2 - \beta^2$$

Letting $H = f(x)G(x)$ and substituting into (B.8) gives :

$$G'' + R^2(x) G = 0 \quad (\text{B.9})$$

$$\text{where } R^2(x) = (f'' + pf' + qf)/f$$

$$\text{and } f(x) = C \exp(-\frac{1}{2} \int p(x) dx), \quad C = \text{constant}$$

By substituting $p(x)$ as given in (B.8) into the expression for $f(x)$ gives :

$$f(x) = C \{\epsilon(x)\}^{\frac{1}{2}} \quad (\text{B.10})$$

Therefore, $H = \{\epsilon(x)\}^{\frac{1}{2}} G$ where C has been absorbed into the constant of G . Next, substituting (B.10) into the expression for $R^2(x)$ gives :

$$R^2(x) = S^2(x) - \beta^2 \quad (\text{B.11})$$

$$\text{where } S^2(x) = \frac{1}{2\epsilon} \frac{d^2\epsilon}{dx^2} - \frac{3}{4\epsilon^2} \left(\frac{d\epsilon}{dx}\right)^2 + \frac{\epsilon}{\epsilon_0} k_0^2$$

$$\text{Since } n(\bar{x}) = \{\epsilon(\bar{x})/\epsilon_0\}^{\frac{1}{2}} = n_a - (n_a - n_c)\bar{x}^2$$

Substitution into the expression for $S^2(x)$ leads to :

$$S^2(x) = k_0^2 n_{\text{eff}}^2(x) \quad (\text{B.12})$$

$$\text{where } n_{\text{eff}}^2(\bar{x}) = n^2(\bar{x}) - \frac{2(n_a - n_c)\{3(n_a - n_c)\bar{x}^2 + n_a\}}{n^2(\bar{x})(k_0 d)^2}$$

B.3 Computer Program Flow Charts

The computer programs used to compute and plot the dispersion curves and the E and H fields for a slab waveguide having a parabolic index distribution throughout the core, cladding and external regions, using the WKB approximation, are described by Figs. B.1 and B.2 respectively. Fields for the TE even and odd, core and cladding modes are

evaluated.

Definition of supplementary labels :

REXT - n_e
XEND - maximum value of \bar{x} to which fields are computed.
NPT - number of field points to be calculated in the core.

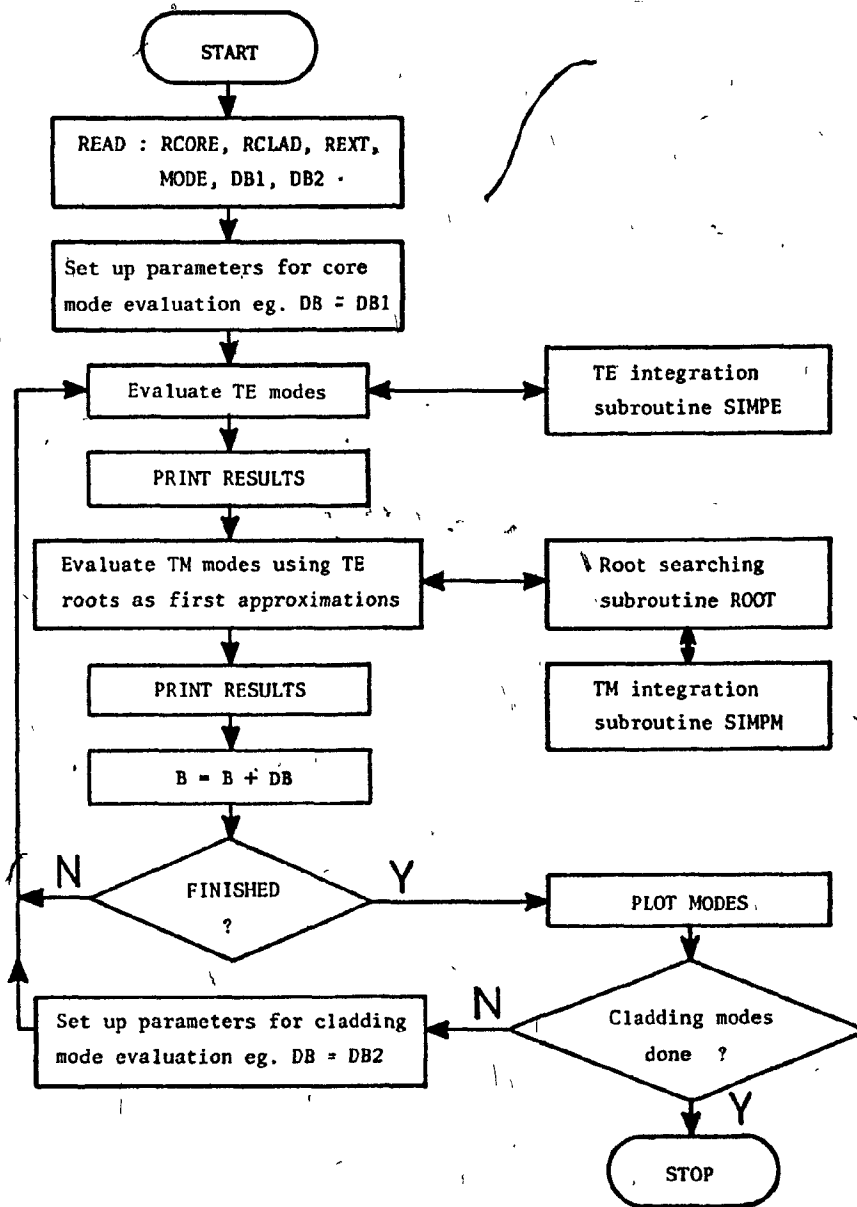


Figure B.1 Flow chart for the dispersion curves program

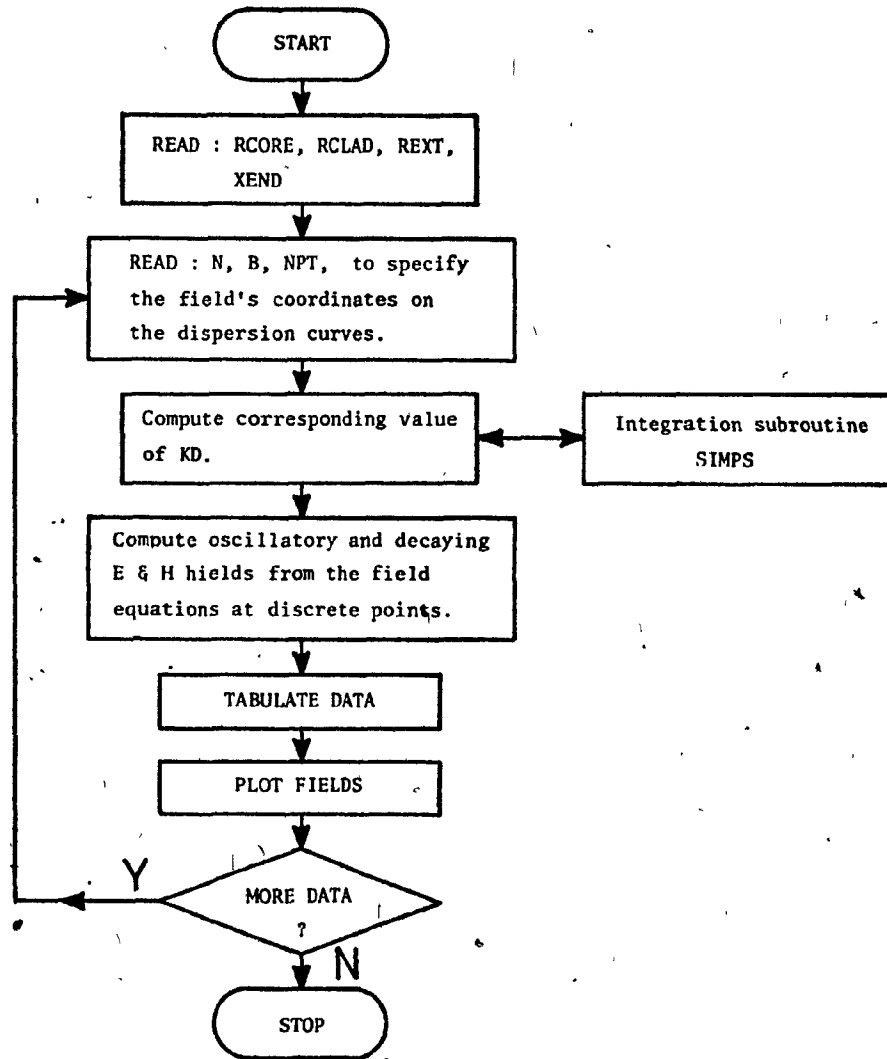


Figure B.2 Generalized flow chart for the fields program

APPENDIX CDETAILS CONCERNING APPARATUS AND PROCEDUREFOR FILM DEPOSITIONC.1 Preparation of Chemicals

Particular attention to cleanliness must be given during chemical preparation, otherwise large quantities of contaminants will be introduced. The most delicate operation is the preparation of the benzene solution of stearic acid. It is prepared in batches of 10 ml. and is stored in a stoppered graduated cylinder so that any evaporation can be accounted for and the concentration maintained nearly constant by the addition of more benzene. The stearic (octadecanoic) acid which has been used is grade 1 (99% pure) and must be stored below 0°C. Since only 0.1 ml. of solution is used to cover the subphase with a film, each batch has a potential of 100 spread films. However, it is recommended to discard the last 2 ml. of solution and prepare a new batch since the concentration of contaminants increases with use.

The weight of stearic acid to be dissolved in 10 ml. of benzene is readily found as follows. Since the area to be covered by the film is 2800 cm², while each stearate molecule covers an area of 20×10^{-16} cm² and stearic acid has a molecular weight of 284.5 gm./mole, then each spread film requires 0.6613 mg. of stearic acid. Therefore a batch of benzene solution is prepared by dissolving 66.13 mg. of stearic acid in 10 ml. of benzene thus giving a concentration of 2.324×10^{-2} M (moles/liter). The solution was kept at room temperature throughout the experiments and showed no noticeable degradation.

To facilitate the preparation of the subphase, concentrated stock solutions of the required chemicals were prepared. The appropriate subphase concentrations could then be easily established merely by adding small portions of these stock solutions to the 3 liters of distilled, deionized water in the trough by means of graduated pipets. The 30 μM concentration of BaCl_2 suggested by Blodgett can be established by adding 1 ml. of the 100 ml. stock solution. Since the molecular weight of $\text{BaCl}_2 \cdot 2\text{H}_2\text{O}$ is 244.3 gm./mole, the stock is prepared by adding 2.199 gm. to 100 ml. of distilled water.

The potassium bicarbonate buffer is prepared as a 500 ml. stock solution and 5 ml. of this is used to yield a subphase concentration of 200 μM KHCO_3 . Since its molecular weight is 100.12 gm./mole, 6.007 gm. are required to make the 500 ml. water solution.

The 2 μM copper concentration is set up by the addition of 1 ml. of a 100 ml. stock solution of CuCl_2 . It is found that 0.1023 gm. of $\text{CuCl}_2 \cdot 2\text{H}_2\text{O}$ must be used since it has a molecular weight of 170.5 gm./mole. Table C.1 has been prepared for easy reference.

Table C.1 : Chemical Preparation Data

CHEMICAL	M.W. gm./mole	STOCK VOL. (ml.)	SOLUTE WT. (gm.)	SUBPHASE CONC. (μM)	STOCK VOL. ADDED (ml.)
Stearic acid	284.5	10	0.06613	—	0.1
$\text{BaCl}_2 \cdot 2\text{H}_2\text{O}$	244.3	100	2.199	30	1.0
KHCO_3	100.1	500	6.007	200	5.0
$\text{CuCl}_2 \cdot 2\text{H}_2\text{O}$	170.5	100	0.1023	2	1.0

C.2 Substrate Cleaning Procedure

When a slide is used for the first time as a substrate on which a film is to be deposited, it must be thoroughly cleaned beforehand, otherwise the coating will be poor. The process which has been adopted is part of one being used in the solid state lab to clean silicon wafers. It consists of two steps, a degreasing step and a decontamination step as outlined below.

1. Degreasing Step

- (a) Boil in trichloroethylene for 8 min. and rinse in deionized, distilled water.
- (b) Immerse in acetone for 15 min. and rinse.
- (c) Immerse in methanol for 15 min. and rinse.

2. Decontamination Step

- (a) Boil in a solution of $H_2O:H_2O_2:NH_4OH$ mixed in a ratio 35:10:5 ml. for 8 min. and rinse.
- (b) Boil in a solution of $H_2O:H_2O_2:HCl$ mixed in a ratio 35:10:5 ml. for 8 min. and rinse.
- (c) Dry the slide by holding it over the hot plate.

Throughout this operation, the slide must only be handled with clean forceps or tweezers. If a slide has been previously coated with a film, this process need not be used as it is only necessary to rub the film down with tissue paper and start depositing new layers. However, if the deposition is found to be poor, the slide must be properly cleaned since the previous film must have contained some greasy contaminants. This initial cleaning of the substrate cannot be overstressed as the

quality of the film is highly dependent on how well the first few layers have been deposited. If the film does not properly adhere to the substrate, even after a few hundred layers, a seemingly good quality film will start to peel off in those areas where there was poor adhesion of the first layer.

C.3 Procedure for Monolayer Deposition

At the outset, the Plexiglas tray must be cleaned with detergent and rinsed thoroughly. It is then dried with some paper towels and rubbed with alcohol soaked tissue paper. The trough is filled with 3 liters of distilled, deionized water, the first 500 ml. being mixed with 1 ml. of the BaCl_2 solution, 5 ml. of the KHCO_3 buffer solution and 1 ml. of the CuCl_2 solution described previously. These quantities are added using the 1 ml. and 10 ml. graduated pipets. Having prepared the subphase, the cooling coil is submerged into the deeper section and the circulating pump is started to initiate cooling, and is turned off and on subsequently as required to maintain the temperature between 17°C and 20°C . Washed CuS is mixed with distilled water and a small amount is added to the subphase by means of a pipet so as to produce a uniform sprinkling of CuS . The addition should be so light that it is not visible on the tray bottom except when observed from a glancing angle. If CuS is used, the pH must not be lowered too much as an acidic solution will react with the CuS and release excessive amounts of copper ions into solution.

The pH was measured with the Fisher Accumet pH meter (Model 140). It will be found that pH determinations must be carefully performed since

the subphase is poorly buffered and is greatly exposed to the air. This causes the meter needle to drift slightly. The pH can be adjusted by adding a few drops of dilute HCl or NaOH and stirring. It should be set within a range from 6.8 to 7.2. The pH will be found to remain in this range due to the fact that the bath is in equilibrium with the carbon dioxide contained in the air. Blodgett quotes the equilibrium pH value at 6.9.

Any surface nonsoluble contamination such as oil and dust particles are removed by using the sweep barriers. First, a barrier is placed across the tray and the surface is swept slowly along its length until the barrier is a few centimeters from the end. This action not only pushes back the contamination behind the barrier, but also draws out that in front of it so that it can be removed by the second barrier. The process is continued a few times, alternating from one barrier to the next, each time cleaning and drying the barrier after removal with tissue paper. It is important that only the ends of the barrier be touched, otherwise oil and grease from the hands will contaminate it. In fact, plastic gloves should be worn during the entire operation as a precautionary measure. The floating barrier can now be deposited on the water surface in position 1 as shown in Fig. C.1, by holding it at its extremities. A test can be made to check for the presence of oil on the surface. With a clean stirring rod, the barrier is gently pushed at its midpoint on the side of the cooling coil. If little or no oil is present, it should easily float away for a short distance. This is continued until the sweep barriers are reached at the opposite end of the tray. If a

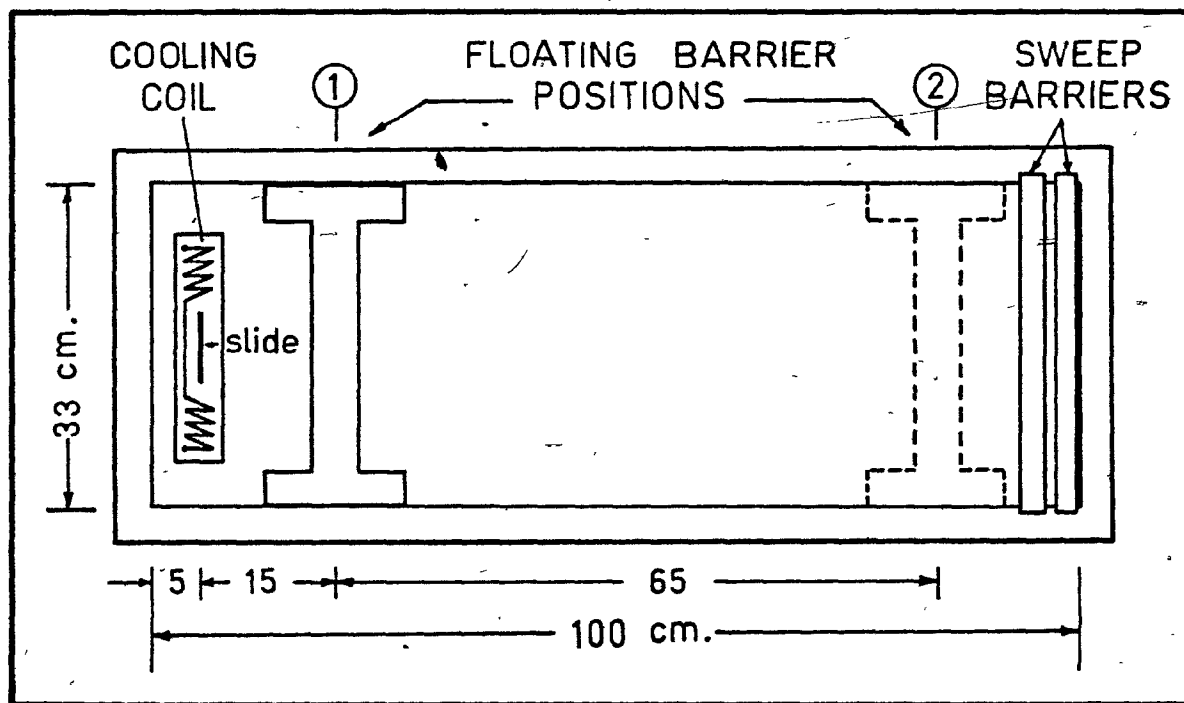


Figure C.1 Top view of film tray.

little oil is present, it will exert a surface pressure on the floating barrier and make it spring back after the stirring rod is removed. If this occurs at a distance of more than a few centimeters from position 2, the surface must be reswept, the floating barrier transferred to position 1, and the test reinitiated. If only very little oil is detected at position 2, the float is intermittently pushed as before, back to position 1. Here again, if too much oil is detected the surface must be reswept. This can be somewhat of a tedious process although extremely necessary if good quality films are to be obtained.

Once the surface has been cleaned, the tray is covered with the Plexiglas sheet to reduce dust contamination. The film can now be spread by transferring 100 μ l. of the benzene solution to the surface using the 100 λ micropipet. The pipet's tip should be held just above the surface and well away from the floating barrier, as benzene will readily dissolve it. The solution should be delivered to the surface continuously and rapidly so that the benzene always remains visible as a few lenses. As the benzene evaporates, the monomolecular film spreads out over the entire surface and exerts a pressure on the floating barrier pushing it back all the way to position 2. After the barrier has come to rest, the subphase surface should be viewed at a glancing angle to check for any visible signs of dust or unspread benzene lenses. If the latter are present, they usually occur around the spreading point near the cooling coil. This situation indicates that there was not enough area for the film to cover. This can occur if the benzene solution is too concentrated or if the surface has not been properly cleaned so that

residual film or oil has reduced the available area. These lenses or dust particles can be slowly removed by touching them with a clean spatula.

After allowing a few minutes for the benzene to evaporate and the copper ions to diffuse to the surface, one drop of "piston oil" is transferred to the surface between the float and the sweep barriers by inserting the pipet through a hole in the dust cover. Oleic acid has been found to be more suitable as it exerts about twice the pressure of castor oil. As soon as it touches the surface, the oil spreads out as a monomolecular layer and exerts a pressure on the floating barrier moving it a few centimeters, thus compressing the film. This quantity of oil is much more than required to cover the entire surface and remains collected in a few lenses from which it will spread as the film is slowly used up.

Once the temperature is below 20°C , the film deposition can begin. A clean (hydrophilic) dry quartz slide is mounted on the holder and positioned so that it just penetrates the water surface with the dipping device at its topmost position and adjusted for a 2 cm. stroke. As it is lowered, a clean slide will not pick up any film. With the speed set to $1/10$ r.p.m., the first layer is coated as the slide is raised at an average of 4 mm./min. This speed is slowly increased for subsequent layers towards $1\frac{1}{2}$ r.p.m. and is limited by the rate at which the ascending slide sheds water. As the film is deposited, the floating barrier moves about 9 mm. for each layer and by observing the shape and behaviour of the meniscus, a good indication of the evenness with which the film is being deposited is obtained. A smooth, uniform, well defined meniscus

indicates good deposition. Even if the coating is poor, as long as some film is being deposited, the process should be continued and after some 50 layers (25 revolutions), the film should be rubbed down with tissue paper until no visible trace of the film is left. This leaves a single molecular layer which provides a good foundation for building (34).

The process should be stopped when the floating barrier reaches a distance of about 15 cm. from the slide. To clean the surface, the slide is first removed and the farthest sweep barrier is removed, wiped, and placed in front of the floating barrier to reduce oil penetration towards the front of the tray. The oil lenses are then removed using small pieces of paper towel and subsequently the floating barrier is withdrawn and wiped gently with tissue paper. The sweep barrier is brought slowly to the middle of the tray and the other one is placed at its head. The barrier at midway is now brought to about 3 cm. from the end and the film behind it is rendered visible due to its compression and can be skimmed off with a microscope slide. An indication of the copper content is obtained by noticing the bluish-green color of the film. The surface can be cleaned reasonably well by successively sweeping with the barriers and removing the oil by sweeping the surface with large sections of paper towel.

The second film can be spread once the previously described oil test has been performed successfully. By proceeding in this way, films of many hundreds of layers can be obtained. If the tray is to be left standing for several hours without use, it is best to remove the cooling coil, clean the surface, and replace the dust cover.

APPENDIX DEQUIPMENT, THEORY, AND DATA FITTING PROGRAM FOR THE DETERMINATION OF
THE OPTICAL CONSTANTS OF THE MULTILAYER FILMD.1 Equipment Alignment

The instrumentation which has been used is illustrated in Fig. 6.4. The movable arm, on which rest the laser and polarizer, gives direct angular reading with a resolution of 1/100 th of a degree. This has been accomplished by making the arm 57.30 cm. long so that the length of the quarter circle would be 90.0 cm. This allowed the use of a flexible centimeter rule mounted on the base to indicate the angular position. By using a vernier attached to the movable arm, a resolution of 1/10 mm. was obtained.

Calibration of the angular measure was achieved through the use of precision 60° and 90° prisms. Initially, the laser was mounted on the stationary rail and its beam aligned parallel to it by observing the spot on a screen mounted on a carrier as the latter was moved along the length of the rail. The 0° position was immediately found by transferring the screen to the movable arm and adjusting its angular position until the spot was stationary as the screen was moved along the arm's length. The 60° position was obtained by mounting a 60° prism on the gimbal assembly which rested over the mechanical pivot on the stationary rail. This arrangement is shown in Fig. D.1. By adjusting the gimbal movements, the prism was positioned with one of its faces normal to the beam by observing the reflection of the incident beam back on the laser head.

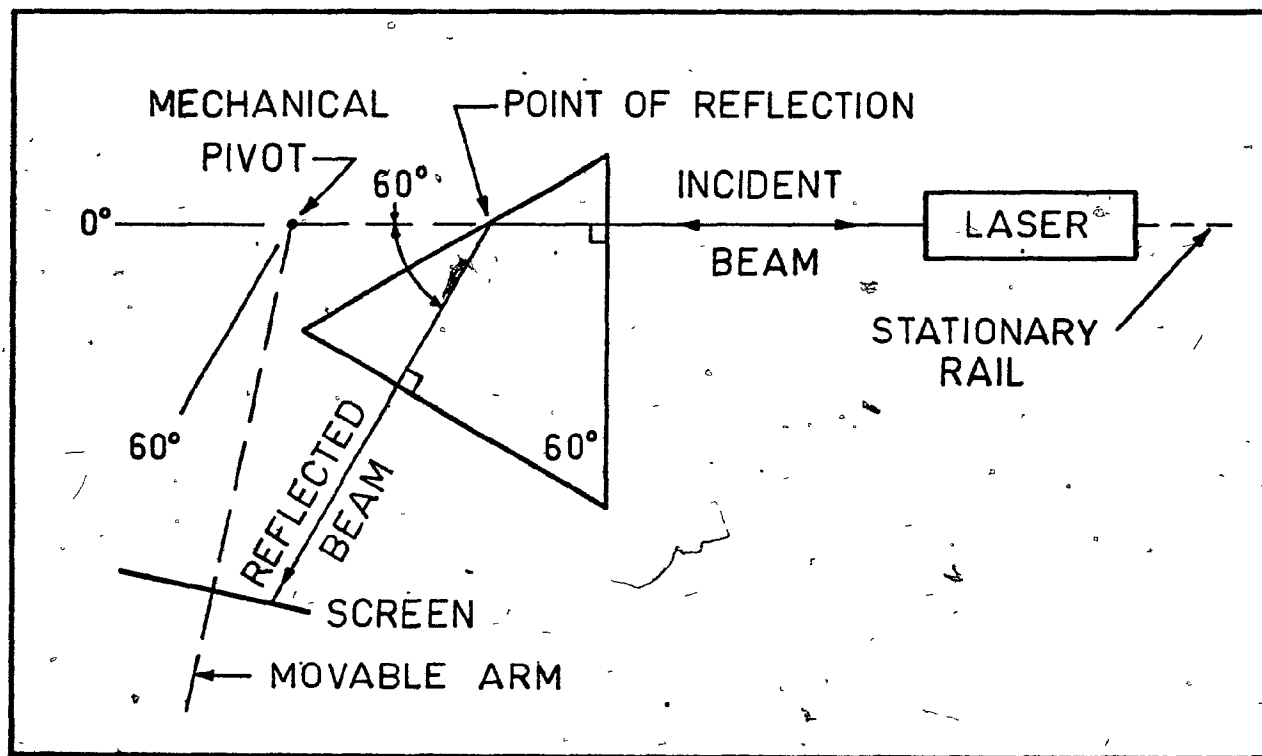


Figure D.1 Pivot and reflection point not coincident.

As implied by the figure, in order to use the reflected beam to set the 60° position, it is necessary that the pivot and point of reflection be coincident. With the screen close to the pivot, the prism was moved parallel to the incident beam until the spot was at the screen's center. Then, with the screen at its farthest point, the angular position of the arm was adjusted. The process was repeated until satisfactory alignment was achieved. In a similar way, a 90° prism was used to find the 90° setting and subsequently the flexible rule was positioned and fixed into place.

To facilitate the finding and measurement of the synchronous directions or mode angles, it was advantageous to align the gimbal so that its axis of rotation was coincident with the pivot. This resulted in a smaller positioner movement to maintain the beam at the coupling point as the laser angle was adjusted. First, it was necessary to find the axis of the gimbal. This was easily performed by mounting on it a vertical pin and observing the shadow it cast on an expanded laser spot as the gimbal was rotated. By adjusting its position successively in perpendicular directions until no motion was observed, the pin was brought in line with the gimbal's axis. To align this axis with the pivot, the laser was positioned on the movable arm so that its beam was parallel to it. Then by observing the shadow cast by the pin as the laser angle was varied from 0° to 90° , the gimbal assembly was successively adjusted until no motion was observed in the pin's shadow. At this point, the gimbal's axis of rotation passed through the pivot.

D.2 Derivation of the Dispersion Relations for a Thin-Film Waveguide whose Film has a Diagonal Permittivity Tensor

Starting from Maxwell's equations :

$$\begin{aligned}\nabla \times \mathbf{E} &= -\frac{\partial \mathbf{B}}{\partial t} \\ \nabla \times \mathbf{H} &= \frac{\partial \mathbf{D}}{\partial t}\end{aligned}\quad (\text{D.1})$$

and the constitutive relations :

$$\begin{aligned}\mathbf{D} &= \hat{\epsilon} \mathbf{E} \\ \mathbf{B} &= \mu_0 \mathbf{H}\end{aligned}\quad (\text{D.2})$$

where the permittivity of the film is given by :

$$\hat{\epsilon} = \begin{bmatrix} \epsilon_x & 0 & 0 \\ 0 & \epsilon_y & 0 \\ 0 & 0 & \epsilon_z \end{bmatrix}$$

The reduced wave equation for the TE and TM modes is readily obtained .

TE case :

$$\frac{\partial^2 E_y}{\partial x^2} - (k_y^2 - \beta^2) E_y = 0 \quad (\text{D.3})$$

where $k_y^2 = \omega^2 \mu_0 \epsilon_y$

With the waveguide geometry as shown in Fig. D.2, the dispersion relation is obtained by matching the E_y and H_z fields at the boundaries.

TE dispersion relation :

$$\tan(Kd) = K(\gamma + \delta) / (K^2 - \gamma\delta) \quad (\text{D.4})$$

where

$$\begin{aligned}K &= k_0 (n_1^2 - \beta^2)^{\frac{1}{2}} \\ \gamma &= k_0 (\beta^2 - n_2^2)^{\frac{1}{2}} \\ \delta &= k_0 (\beta^2 - n_3^2)^{\frac{1}{2}}\end{aligned}$$

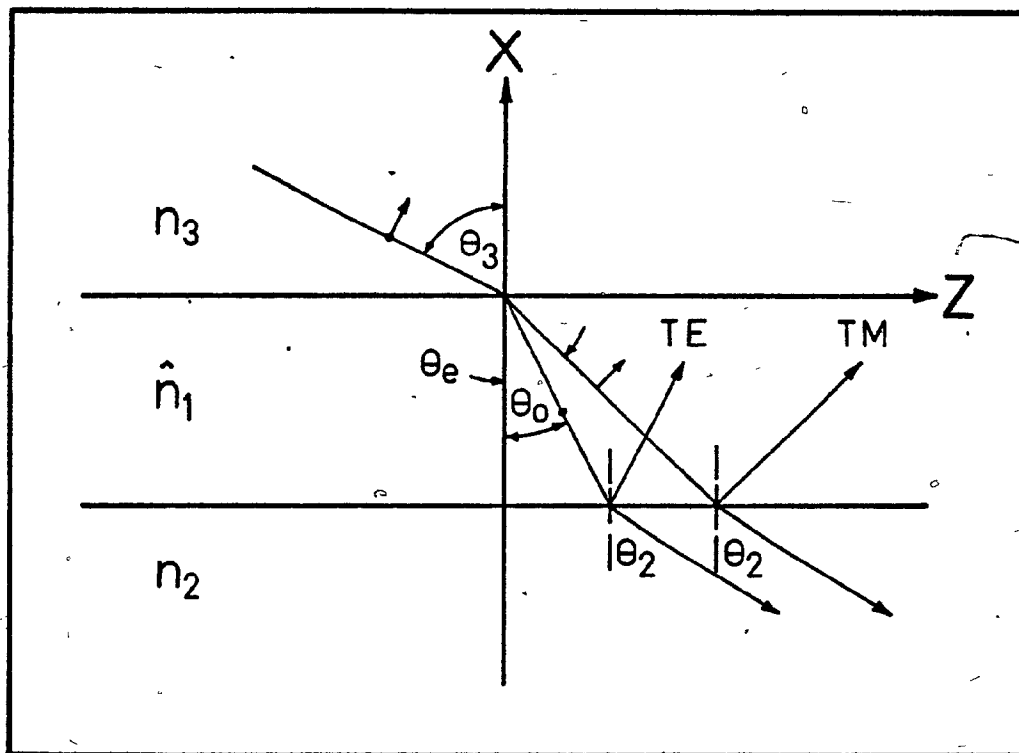


Figure D.2 Thin-film waveguide geometry showing the ordinary (TE) and extraordinary (TM) rays.

This is the same as for the isotropic case where the film index is just equal to n_{1y} . The reduced wave equation for the TM waves is :

$$\frac{\partial^2 H_y}{\partial x^2} + \left\{ k_z^2 - \beta^2 \frac{k_z^2}{k_x^2} \right\} H_y = 0 \quad (D.5)$$

where $k_z^2 = \omega^2 \mu_0 \epsilon_z$ and $k_x^2 = \omega^2 \mu_0 \epsilon_x$

By letting :

$$K^2 = k_0^2 \left\{ n_{1z}^2 - \beta^2 \frac{n_{1z}^2}{n_{1x}^2} \right\}$$

the dispersion relation takes the same form as for the isotropic case.

TM dispersion relation :

$$\tan(Kd) = \frac{n_{1z}^2 K (n_3^2 \gamma + n_2^2 \delta)}{(n_2^2 n_3^2 K^2 - n_{1z}^4 \gamma \delta)} \quad (D.6)$$

In order to obtain a ray picture of the TE (ordinary) and TM (extraordinary) waves, respective refractive indices n_o and n_e associated with these rays can be defined in terms of the elements of \hat{n}_1 . The ordinary and extraordinary rays make angles θ_o and θ_e respectively with the x-axis as shown in Fig. D.2. Since the rays must obey Snell's law, then :

$$\beta = n_3 \sin \theta_3 = n_o \sin \theta_o = n_e \sin \theta_e = n_2 \sin \theta_2 \quad (D.7)$$

For the ordinary (TE) ray : $K_o^2 = (k_0 n_o \cos \theta_o)^2$

but from (D.4) :

$$K^2 = k_0^2 (n_{1y}^2 - \beta^2) = k_0^2 (n_{1y}^2 - n_o^2 \sin^2 \theta_o)$$

so that $n_o = n_{1y}$ (D.8)

For the extraordinary (TM) ray :

$$K^2 = (k_0 n_e \cos \theta_e)^2$$

but from (D.5)

$$K^2 = k_0^2 n_{1z}^2 \left(1 - \frac{\bar{\beta}^2}{n_{1x}^2}\right) = k_0^2 n_{1z}^2 \left(1 - \frac{n_e^2 \sin^2 \theta_e}{n_{1x}^2}\right)$$

so that
$$\frac{\cos^2 \theta_e}{n_{1z}^2} + \frac{\sin^2 \theta_e}{n_{1x}^2} = \frac{1}{n_e^2} \quad (D.9)$$

This shows that the effective index n_e for the extraordinary ray is also a function of its angle θ_e .

D.3 Data Fitting Program

The program used to compute the refractive index tensor and thickness of the anisotropic film is described in Fig. D.3 while Fig. D.4 describes the program used to compute and plot the dispersion curves for the anisotropic thin-film waveguide.

Definition of Labels :

- RSTRT - Initial index value.
- DR - Incremental index step.
- FMIN - Maximum allowable value of G.
- RMIN - Accuracy in index value.
- R2, R3 - Indices of substrate and external medium.
- ME - Specifies 'TE' or 'TM' modes.
- R1Z - TE index required for TM index computation.
- LAY - Number of layers in the film.
- MODE - Number of modes to be fitted at one film thickness.
- BEX - Experimental $\bar{\beta}$ values for these modes.

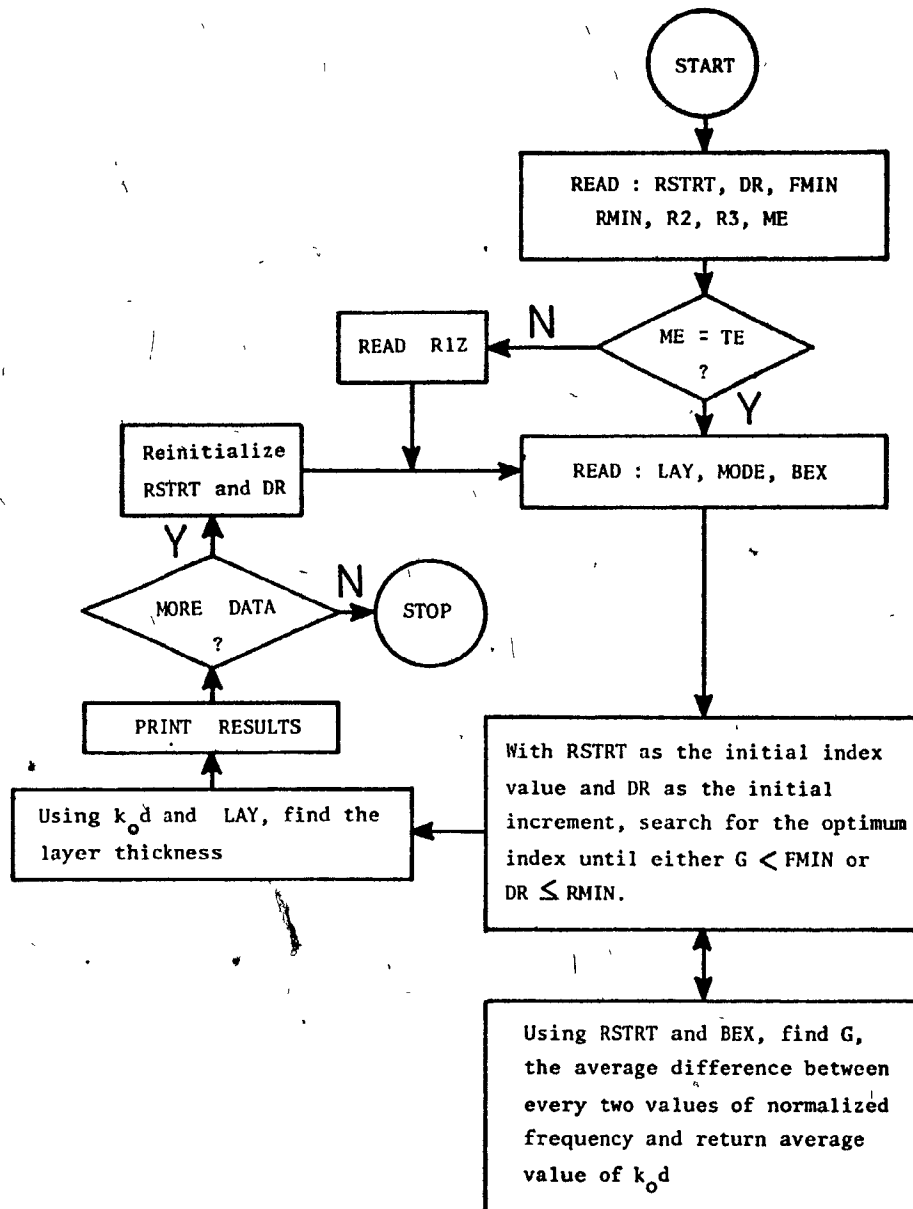


Figure D.3 Generalized flow chart for the data fitting program.

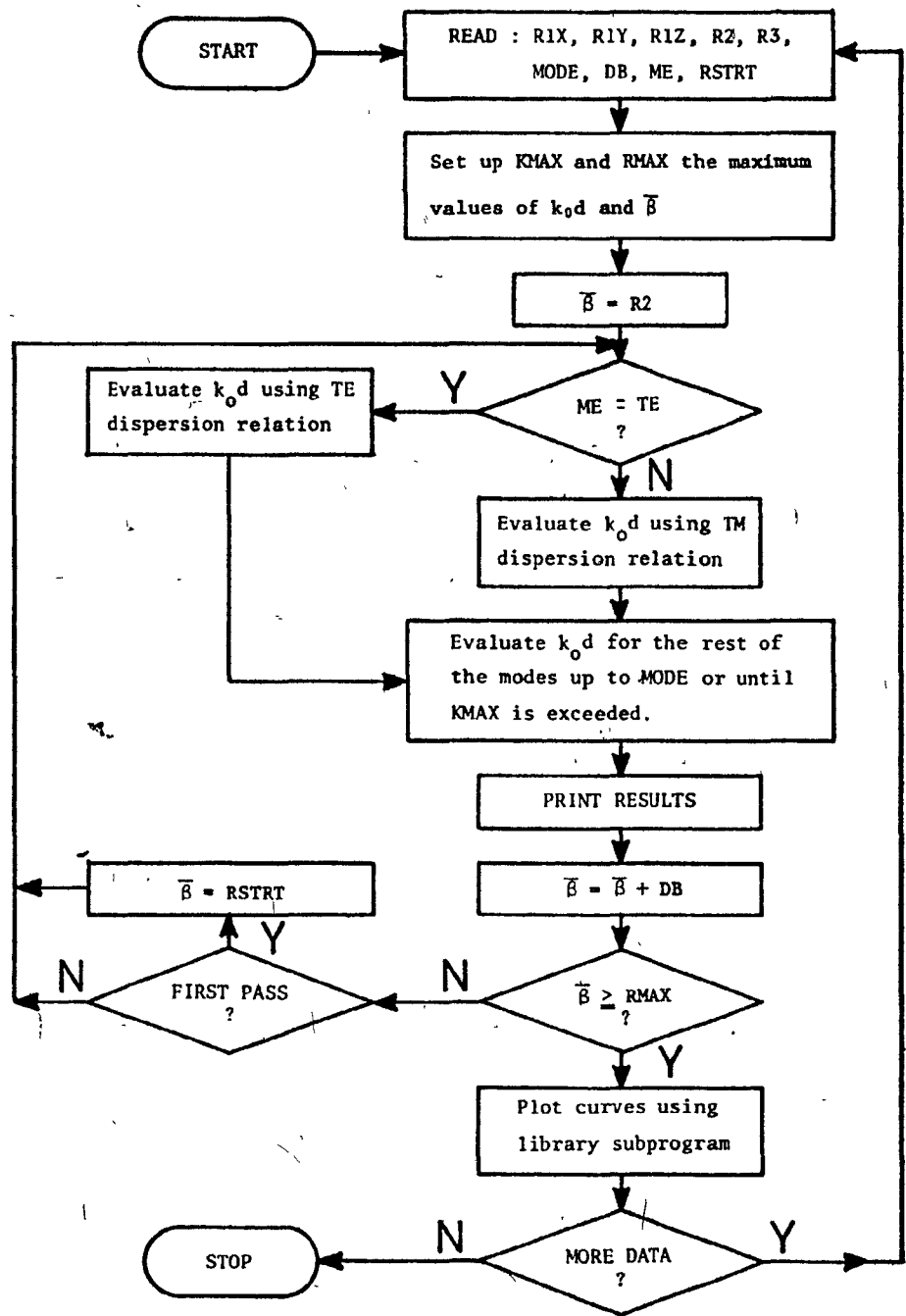


Figure D.4 Flow chart of the program used to compute and plot the dispersion curves for the anisotropic thin-film waveguide.

The minimization of G , the average difference between every two $(kod)_i$, is carried out by employing a modified "interval-halving method" (38) to search for the root, since G is a positive quantity. In other words, consecutive intervals of index are set up and at the end-points G is evaluated and compared. Once the root is confined within an interval, it is continuously subdivided until either $G < FMIN$ or the interval $\leq RMIN$. This procedure is best demonstrated by following a sample search indicated by Fig. D.5.

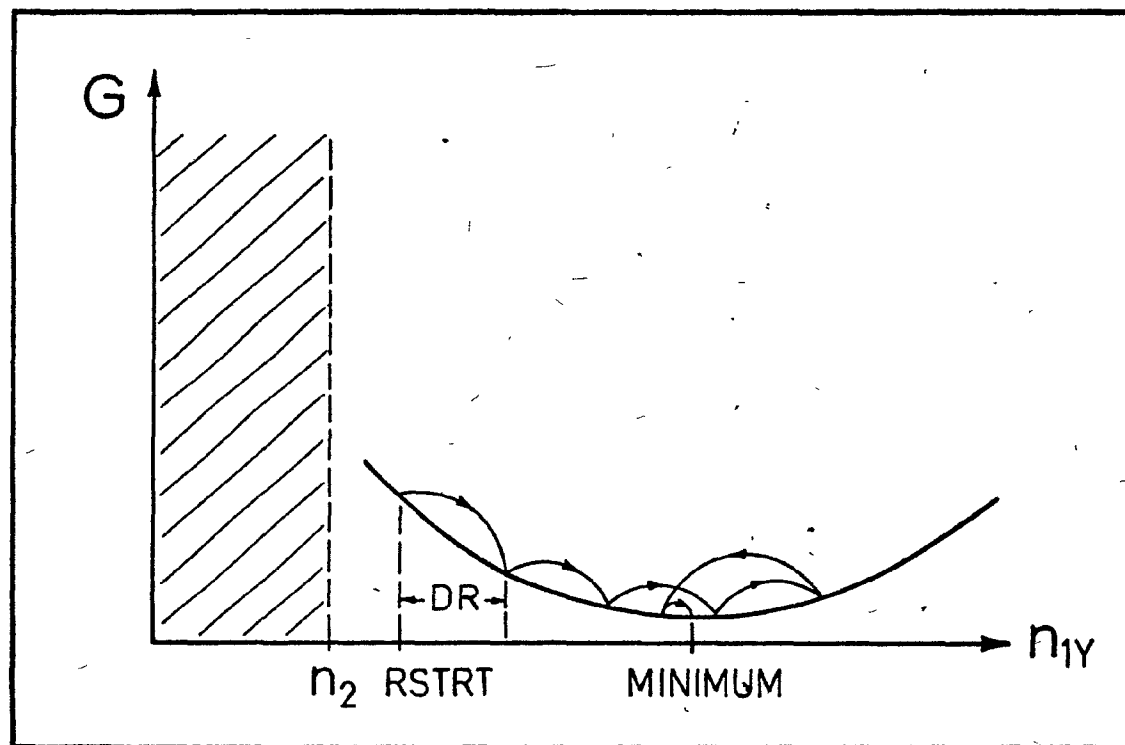


Figure D.5 Sample search for minimum G .

REFERENCES

- (1) C.K. KAO and J.E. GOELL, "Design process for fiber-optic systems follows familiar rules", Electronics, Vol. 49, No. 19, pp. 113-116, Sept., 16, 1976.
- (2) R. GUNDLACH, "Fiber-optic developments spark worldwide interest", Electronics, Vol. 49, No. 16, pp. 81-104, Aug. 5, 1976.
- (3) S.E. MILLER, "Integrated optics : An introduction", Bell Syst. Tech. J. 48, 2059 (1969).
- (4) J.E. GOELL and R.D. STANDLEY, "Integrated optical circuits", Proc. IEEE 58, 1504 (1970).
- (5) P.K. TIEN, "Light waves in thin films and integrated optics", Appl. Opt. 10, 2395 (1971).
- (6) S.E. MILLER, "A survey of integrated optics", IEEE J. Quantum Electron. QE-8, 199 (1972).
- (7) D. MARCUSE, "Integrated optics", IEEE Press, 1972.
- (8) D. MARCUSE, "Theory of dielectric optical waveguides", Academic Press, New York, 1974.
- (9) R.V. POLE, S.E. MILLER, J.H. HARRIS, and P.K. TIEN, "Integrated optics and guided waves - A report of the Topical meeting", Appl. Opt. 11, 1675 (1972).

- (10) Y. SUEMATSU, "The progress of integrated optics in Japan", IEEE Trans. MTT 23, 16 (1975).
- (11) H. KOGELNIK, "An introduction to integrated optics", IEEE Trans. MTT 23, 2 (1975).
- (12) R.V. POLE, E.M. CONWELL, H. KOGELNIK, P.K. TIEN, J.R. WHINNERY, A. YARIV, and A.J. DeMARIA, "Integrated optics : A report on the 2nd OSA Topical Meeting", Appl. Opt. 14, 569 (1975).
- (13) K.-H. STEINER, "A theory of the dielectric multi-layer-core waveguide", Optical and Quantum Electronics 7, 59 (1975).
- (14) S. SUGIMOTO, K. KOBAYASHI, K. NISHIZAWA, and A. UEKI, "Light coupling from a DH laser into a Selfoc[®] fiber using slab Selfoc[®] lenses", Topical Meeting on Optical Fiber Transmission, Williamsburg, Virginia, paper WD1-1-4, Digest 1975.
- (15) W. STREIFER and C.N. KURTZ, "Scalar analysis of radially inhomogeneous guided media", J. Opt. Soc. Am. 57, 779 (1967).
- (16) C.N. KURTZ and W. STREIFER, "Guided waves in inhomogeneous focusing media part I : formulation, solution for quadratic inhomogeneity", IEEE Trans. MTT 17, 11 (1969).
- (17) C.N. KURTZ and W. STREIFER, "Guided waves in inhomogeneous focusing media part II : asymptotic solution for general weak inhomogeneity", IEEE Trans. MTT 17, 250 (1969).

- (18) H. KIRCHHOFF, "The solution of Maxwell's equation for inhomogeneous dielectric slabs", Arch. Elek. Übertragungstech 26, 537 (1972).
- (19) D. MARCUSE, "TE modes of graded-index slab waveguides", IEEE J. Quantum Electron. QE-9, 1000 (1973).
- (20) E.F. KUESTER and D.C. CHANG, "Propagation, attenuation, and dispersion characteristics of inhomogeneous dielectric slab waveguides", IEEE Trans. MTT 23, 98 (1975).
- (21) Y. SUEMATSU and K. FURUYA, "Propagation mode and scattering loss of a two-dimensional dielectric waveguide with gradual distribution of refractive index", IEEE Trans. MTT 20, 524 (1972).
- (22) E.M. CONWELL, "WKB approximation for optical guide modes in a medium with exponentially varying index", J. Appl. Phys. 46, 1407 (1975).
- (23) E.M. CONWELL, " 'Buried Modes' in planar media with non-monotonically varying index of refraction", IEEE J. Quantum Electron. QE-11, 217 (1975).
- (24) P.K. TIEN, R. ULRICH, and R.J. MARTIN, "Modes of propagating light waves in thin deposited semiconductor films", Appl. Phys. Lett. 14, 291 (1969).
- (25) J.E. GOELL and R.D. STANDLEY, "Sputtered glass waveguide for integrated optical circuits", Bell Syst. Tech. J. 48, 3445 (1969).

- (26) E.R. SCHINELLER, R.P. FLAM, and D.W. WILMOT, "Optical waveguides formed by proton irradiation on fused silica", J. Opt. Soc. Am. 58, 1171 (1968).
- (27) P.K. TIEN, R. ULRICH, and R.J. MARTIN, "Optical second harmonic generation in form of coherent Cerenkov radiation from a thin-film waveguide", Appl. Phys. Lett. 17, 447 (1970).
- (28) H.P. WEBER, W.J. TOMLINSON, and E.A. CHANDROSS, "Organic materials for integrated optics", Optical and Quantum Electronics 7, 465 (1975).
- (29) F. MOHRING, D. VOLKMANN, and D. HUHN, "Wave propagation in low-loss acrylic resin films", Optical and Quantum Electronics 7, 443 (1975).
- (30) G.-C. RIGHINI, V. RUSSO, and S. SOTTINI, "KOR negative photoresist in integrated optics", Optical and Quantum Electronics 7, 447 (1975).
- (31) R. ULRICH and H.P. WEBER, "Solution-deposited thin films as passive and active light-guides", Appl. Opt. 11, 428 (1972).
- (32) P.K. TIEN, G. SMOLINSKY, and R.J. MARTIN, "Thin organosilicon films for integrated optics", Appl. Opt. 11, 637 (1972).
- (33) K.B. BLODGETT, "Films built by depositing successive monomolecular layers on a solid surface", J. Amer. Chem. Soc. 57, 1007 (1935).

- (34) K.B. BLODGETT and I. LANGMUIR, "Built-up films of barium stearate and their optical properties", Phys. Rev. 51, 964 (1937).
- (35) I. LANGMUIR, "Pilgrim Trust Lecture molecular layers", Proc. Roy. Soc., Ser A 170, 1 (1939).
- (36) V.K. SRIVASTAVA and A.R. VERMA, "Interferometric and X-ray diffraction study of 'built-up' molecular films of some long chain compounds", Solid State Commun. 4, 367 (1966).
- (37) V.K. SRIVASTAVA, "Built-up molecular films and their applications", in Physics of Thin Films, G. Hass, M.H. Francombe and R.W. Hoffmann, Eds., Academic, New York, 1973, Vol. 7, pp. 311-397.
- (38) C.F. GERALD, "Applied numerical analysis", Addison-Wesley (Series in Mathematics) London, 1973, p. 2.
- (39) P.M. MORSE and H. FESHBACH, "Methods of theoretical physics", Vol. II, McGraw-Hill, New York, 1953.
- (40) G.L. GAINES, Jr., "Insoluble monolayers at liquid-gas interfaces", Wiley (Interscience), New York, 1966.
- (41) J.B. BATEMAN and E.J. COVINGTON, "Molecular tilt in fatty acid multilayers", J. Colloid Sci. 16, 531 (1961).
- (42) B.L. HENKE, "X-ray fluorescence analysis for sodium, fluorine, oxygen, nitrogen, carbon, and boron", in Advan. in X-ray Anal., W.M. Mueller, G.Mallett, and M. Fay, Eds., Plenum Press, New York, 1964, Vol. 7, pp. 460-488.

- (43) G. POSTE and C. MOSS, "The study of surface reactions in biological systems by ellipsometry", *Progress in Surface Science* 2, 139 (1972).
- (44) A. ROTHEN, "Ellipsometric studies of thin films", *Progress in Surface and Membrane Science* 8, 81 (1974).
- (45) S. TOLANSKY, "Multiple beam interferometry of surfaces and films", Oxford Univ. Press (Clarendon), London and New York, 1948.
- (46) J.S. COURTNEY-PRATT, "An optical method of measuring the thickness of adsorbed monolayers", *Proc. Roy. Soc., Ser A* 212, 505 (1952).
- (47) F.L. McCRACKIN, E. PASSAGLIA, R.R. STROMBERG, and H.L. STEINBERG, "Measurement of the thickness and refractive index of very thin films and the optical properties of surfaces by ellipsometry", *J. Res. Natl. Bur. Std.* 67A, 363 (1963).
- (48) E. COLOMBINI, "Ellipsometric measurements for thin-film waveguides : theory and technique", technical report, *Elect. Eng. Dept.*, McGill Univ., Montreal, 1976.
- (49) D. d.ENGELSEN, "Ellipsometry of anisotropic films", *J. Opt. Soc. Am.* 61, 1460 (1971).
- (50) V. DANEU and A. SANCHEZ, "Measuring the refractive index and thickness of thin transparent films : a method", *Appl. Opt.* 13, 122 (1974).

- (51) R. MITTRA and T. ITOH, "A method for measuring the refractive index profile of thin-film waveguides", IEEE Trans. MTT 23, 176 (1975).
- (52) P.K. TIEN and R. ULRICH, "Theory of prism-film coupler and thin-film light guides", J. Opt. Soc. Am. 60, 1325 (1970).
- (53) P.K. TIEN, "Light wave coupling into thin films", Canadian Patent 901352, May 30, 1972.
- (54) R. ULRICH, "Theory of the prism-film coupler by plane-wave analysis", J. Opt. Soc. Am. 60, 1337 (1970).
- (55) K. OGAWA, W.S.C. CHANG, B.L. SOPORI, and F.J. ROSENBAUM, "A theoretical analysis of etched grating couplers for integrated optics", IEEE J. Quantum Electron. QE-9, 29 (1973).
- (56) M.L. DAKSS, L. KUHN, P.F. HEIDRICH, and B.A. SCOTT, "Grating couplers for efficient excitation of optical guided waves in thin films", Appl. Phys. Lett. 16, 523 (1970).
- (57) P.K. TIEN and R.J. MARTIN, "Experiments on light waves in a thin tapered film and a new light-wave coupler", Appl. Phys. Lett. 18, 398 (1971).
- (58) Y. SATOMURA, M. MATSUHARA, and N. KUMAGAI, "Analysis of electromagnetic-wave modes in anisotropic slab waveguide", IEEE Trans. MTT 22, 86 (1974).

- (59) R.C. WEAST, "Handbook of chemistry and physics", C.R.C. Press, Cleveland, Ohio, 57th Ed., 1976, p. E-224.
- (60) I.P. KAMINOW, "An introduction to electrooptic devices", Academic Press, New York, 1974.
- (61) J.T. MILEK and M. NEUBERGER, "Linear electrooptic modulation materials", in Handbook of Electronic Materials, Vol. 8, IFI/Plenum, New York, 1972.